Clemson University

TigerPrints

All Dissertations

Dissertations

December 2018

Situational Intelligence for Improving Power System Operations Under High Penetration of Photovoltaics

Yawei Wei

Clemson University, yaweiw@g.clemson.edu

Follow this and additional works at: https://tigerprints.clemson.edu/all_dissertations

Recommended Citation

Wei, Yawei, "Situational Intelligence for Improving Power System Operations Under High Penetration of Photovoltaics" (2018). *All Dissertations*. 2564.
https://tigerprints.clemson.edu/all_dissertations/2564

This Dissertation is brought to you for free and open access by the Dissertations at TigerPrints. It has been accepted for inclusion in All Dissertations by an authorized administrator of TigerPrints. For more information, please contact kokeefe@clemson.edu.

SITUATIONAL INTELLIGENCE FOR IMPROVING POWER SYSTEM OPERATIONS UNDER HIGH PENETRATION OF PHOTOVOLTAICS

A Dissertation
Presented to
the Graduate School of
Clemson University

In Partial Fulfillment
of the Requirements for the Degree
Doctor of Philosophy
Electrical Engineering

---

by
Yawei Wei
December 2018

Accepted by:
Dr. Ganesh Kumar Venayagamoorthy, Committee Chair
Dr. Johan Enslin
Dr. Shuangshuang Jin
Dr.Rajendra Singh

ABSTRACT

Nowadays, power grid operators are experiencing challenges and pressures to balance the interconnected grid frequency with rapidly increasing photovoltaic (PV) power penetration levels. PV sources are variable and intermittent. To mitigate the effect of this intermittency, power system frequency is regulated towards its security limits. Under aforementioned stressed regimes, frequency oscillations are inevitable, especially during disturbances and may lead to costly consequences as brownout or blackout. Hence, the power system operations need to be improved to make appropriate decision in time. Specifically, concurrent or beforehand power system precise frequencies, simplified straightforward-to-comprehend power system visualizations and cooperated well-performed automatic generation controls (AGC) for multiple areas are needed for operation centers to enhance.

The first study in this dissertation focuses on developing frequency prediction general structures for PV and phasor measurement units integrated electric grids to improve the situational awareness (SA) of the power system operation center in making normal and emergency decisions ahead of time. Thus, in this dissertation, a frequency situational intelligence (FSI) methodology capable of multi-bus type and multi-timescale prediction is presented based on the cellular computational network (CCN) structure with a multi-layer proception (MLP) and a generalized neuron (GN) algorithms. The results present that both CCMLPN and CCGNN can provide precise multi-timescale frequency predictions. Moreover, the CCGNN has a superior performance than the CCMLPN.

The second study of this dissertation is to improve the SA of the operation centers by developing the online visualization tool based on the synchronous generator vulnerability index (GVI) and the corresponding power system vulnerability index (SVI) considering dynamic PV penetration. The GVI and SVI are developed by the coherency grouping results of synchronous generator using K-Harmonic Means Clustering (KHMC) algorithm. Furthermore, the CCGNN based FSI method has been implemented for the online coherency grouping procedure to achieve a faster-than-real-time grouping performance.

Last but not the least, the multi-area AGCs under different PV integrated power system operation conditions are investigated on the multi-area multi-source interconnected testbed, especially with severe load disturbances. Furthermore, an onward asynchronous tuning method and a two-step (synchronous) tuning method utilizing particle swarm optimization algorithm are developed to refine the multi-area AGCs, which provide more opportunities for power system balancing authorities to interconnect freely and to utilize more PV power.

In summary, a number of methods for improving the interconnected power system situational intelligence for a high level of PV power penetration have been presented in this dissertation.

DEDICATION

I dedicate my dissertation work to my parents, Bianhua Pang and Jianguo Wei, for their continuous support during my Ph.D. study, especially for the time that I suffered for the research bottleneck. A special gratitude to my wife, Dr. Shuning Chen, the encouragement conversations help me reach to the end.

I also dedicate this work to my colleagues, Ke Tang, Iroshani Jayawardene, Paranietharan Arunagirinathan, Xingsi Zhong, Pramod Herath, Chirath Pathiravasam, and Md Ashfaqur Rahman, for your supporting and cooperating works throughout the entire Ph.D. process.

ACKNOWLEDGMENTS

Firstly, I would like to have special thanks to Dr. Ganesh Kumar Venayagamoorthy for his countless hours of discussing, encouraging, commenting, reviewing, and especially the patience during the whole doctorate process.

Secondly, I would like to thank Dr. Johan Enslin, Dr. Shuangshuang Jin, and Dr. Rajendra Singh for approving and serving on my committee.

Last but not least, I wish to acknowledge the United States National Science Foundation and the Duke Energy for the support of my Ph.D. research. This work is supported in part by the National Science Foundation (NSF) of the United States, under grant IIP #1312260 and ECCS #1408141, and the Duke Energy Distinguished Professorship Endowment Fund. Any opinions, findings and conclusions or recommendations expressed in this material are those of the author(s) and do not necessarily reflect the views of the financial support.

TABLE OF CONTENTS

Page

CHAPTER

Page

LIST OF TABLES

List of Tables (Continued)

Table Page

LIST OF FIGURES

List of Figures (Continued)

Figure Page

List of Figures (Continued)

Figure Page

List of Figures (Continued)

CHAPTER 1

INTRODUCTION

1.1 Overview

The modern power grid is being transformed towards renewable energy era as the trend of worldwide government policies on lower carbon emission [1-3] and renewable device market dynamics [4-5], notably for the dramatically reduced cost of solar PV plant in both distributed scale and utility scale [2-4]. As a consequence of the aforementioned mandates, the penetration level of PV in the grid will be continuously increased in long-term perspective [5]. The future smart grid vision presents a grid with a variety of renewable power integrated and new technology-based infrastructures, as shown in Figure 1.1.

As more PV plants connected to the main grid, they bring in the extra power as well as the nature uncertainty, known as the power intermittency. Firstly, the extra power must be mitigated by replacing the other deployed plants, like gas, hydro or coal plants. Second, the intermittency issue results in the system-wide frequency excursion. Maintaining the system-wide frequency stable and security also require a significant displacement of the onsite conventional generators [6-7]. This situation has led the current power grids to operate towards their frequency security limits, which requires the Situational Awareness (SA) to be faster, more comprehensive and well-refined [8]. To meet the requirements of the future power system, the situational awareness of the current control center needs to be enhanced.

1.2 Challenges for Power System Operation with PMUs and PV Powers

Electric grids have carefully designed, scheduled and protected at operation centers to maintain reliable power supply in traditional generation and demand situations. Through one-direction grid hierarchy, near a fixed supply-demand curve and corresponding supervisory control and data acquisition (SCADA) system at a typical rate of 2 to 10 seconds, operation center can coordinate grid-monitoring, control and power dispatch functions with pre-determined values, regarded as “the brain” of power systems.

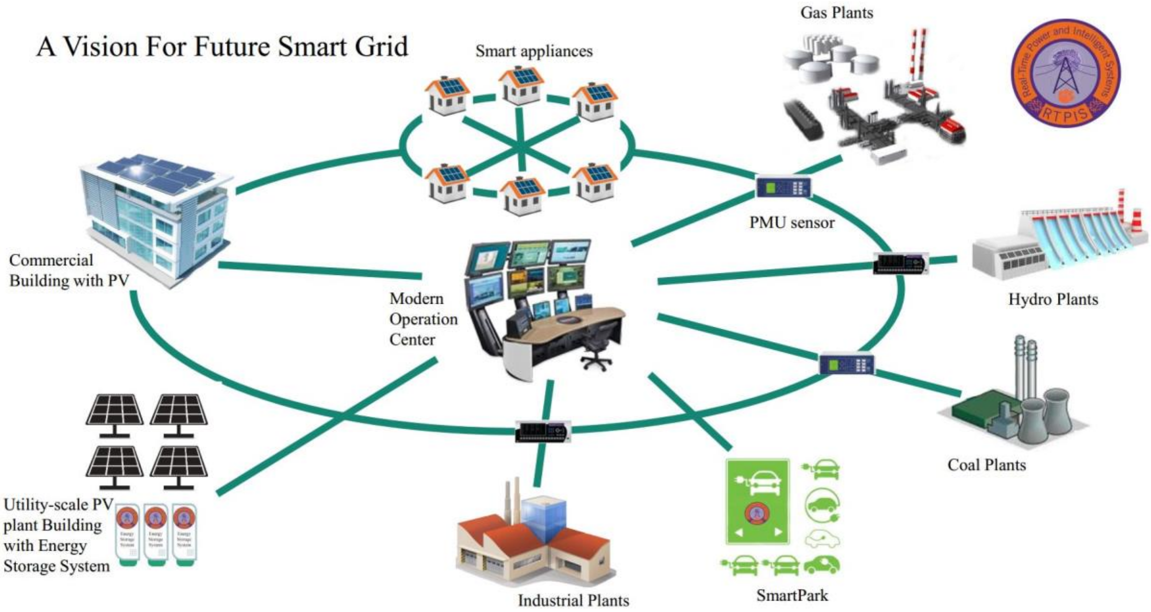

Figure 1.1 An overview of Smart Grid and its components.

Within a system operation center, frequency information is of critical importance in the monitoring, control, and protection of power systems [9]. The frequency of a power system at any given point in time reflects the effective balancing of both generation and load. Unfortunately, the increased integration of renewable energy sources, electric vehicles, storage batteries, and demand-response management now means that the periodic energy dispatch decisions can no longer be determined independently by the control centers [10].

This transition imposes challenges in maintaining an optimal system frequency. During extreme weather conditions, these imbalances can lead to severe frequency disturbances, system-wide frequency instabilities and even system blackout [11-13]. Specifically, the occurrence of a local disturbance triggers a protection device that in turn trips a section of the power network, depending on the severity of the disturbance, which in turn increases the frequency stress of that portion of the power. Such stress thus may result in a larger area underfrequency load shedding (UFLS) which in turn stabilizes the grid frequency [14]. However, these UFLS schemes are not without tremendous economic cost, as illustrated in the 2003 North America-Canada blackout [13].

To prevent such events from occurring, these broadly installed SCADA systems provide limited measurements and intelligence that intelligent control systems and system operators can use to rapidly analyze and predict dynamic frequency trajectories [8-9]. Phasor measurement units (PMUs), in contrast, can capture and transmit current and voltage phasor data at higher sampling rates, 30 Hz/60 Hz, than the SCADA, which is shown in Figure 1.2. Nowadays, the North America power grids continuously deploy PMUs into their electric networks [17]. Transmitting through the wide area measurement system (WAMS), PMU measurements provide time and location synchronized grid operation information that reveals detailed system dynamic behaviors.

Thus, advanced computational methods are needed to leverage new grid sensors and eventually provide intelligent information and knowledge for enhanced power system operation and control [14].

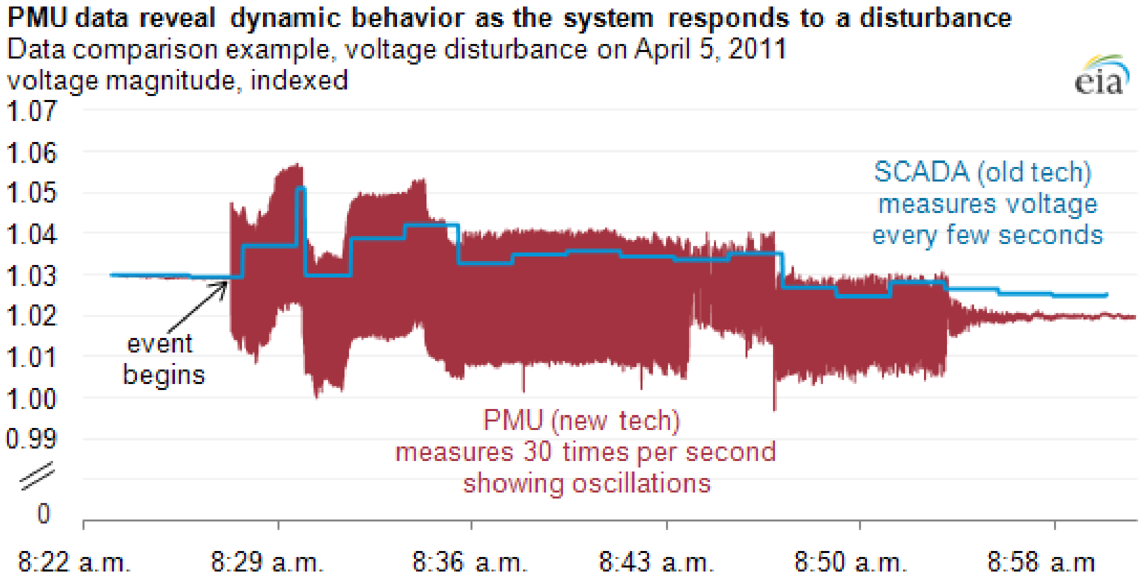

Figure 1.2 A general sampling rate comparison between PMU and SCADA [16].

The vulnerability of power system with PV power integrated has been the object of many researches works in distributed network level [18-19]. These studies investigate the consequences of the PV penetrated power system, and furthermore, design energy management system for mitigation. Physical solar plant involved test bed has also been developed for the purpose of investigation [20-23] on the distribution level. The transmission area effects with high penetration PV is a rather ongoing topic [6]. It has been introduced in [6] that the high level of PV connected to the grid, the system voltage, and rotor angular stability will be significantly affected. The results examine the effects for stability issue using a various amount of rooftop solar plants and several fixed utility-scale PV plants in a specialized 2419-bus western electricity coordinating council (WECC) system. The solar plants are aggregated models. Therefore the dynamic voltage and speed profiles of the system have to zoom into a certain part for analyzing.

Furthermore, due to computation and communication latencies, it is prohibitive to carry out detailed as well as holistic grid impact reviews in the aftermath of disturbances. Thus, the power system dynamic frequency responses to different PV penetration situations have to be addressed and discovered through system coherence analysis for model reduction and simplification [23].

1.3 Frequency Based Researches for Modern Power System

The research focuses for power system frequency can be categorized into four aspects as the protection; the operation, also known as the Automatic Generation Control (AGC); power system simplification, and the prediction. A brief overview of the researches is shown in Figure 1.3 with the highlight topics covered in this study. To avoid extreme under or over frequency situations, the Under Frequency Load Shedding (UFLS) and Out-Of-Step (OOS) protection are discussed in the protection area. To balancing the load and generation, which is maintaining the frequency at 60 Hz, the power system operations are analyzed different operating conditions to design the suitable AGCs. As a unified parameter for system-wide measurements, frequency has been utilized to simplify the power system generator behaviors via the conventional model reduction or using the new soft computing algorithm based methods. After the simplification, the generators are condensed to several groups straightforward for the operator to comprehend.

Frequency dynamic changes reflect the situations of the power system load and generation balancing. Hence, any major disturbances will lead to an excursion of frequency in the plot. Known the abnormal beforehand (frequency prediction) based on the historical and current information will help the power system operators to make adequate just-in-time decisions. The field of the frequency prediction involves the long-going estimation and the new PMU or SCADA data-driven methods.

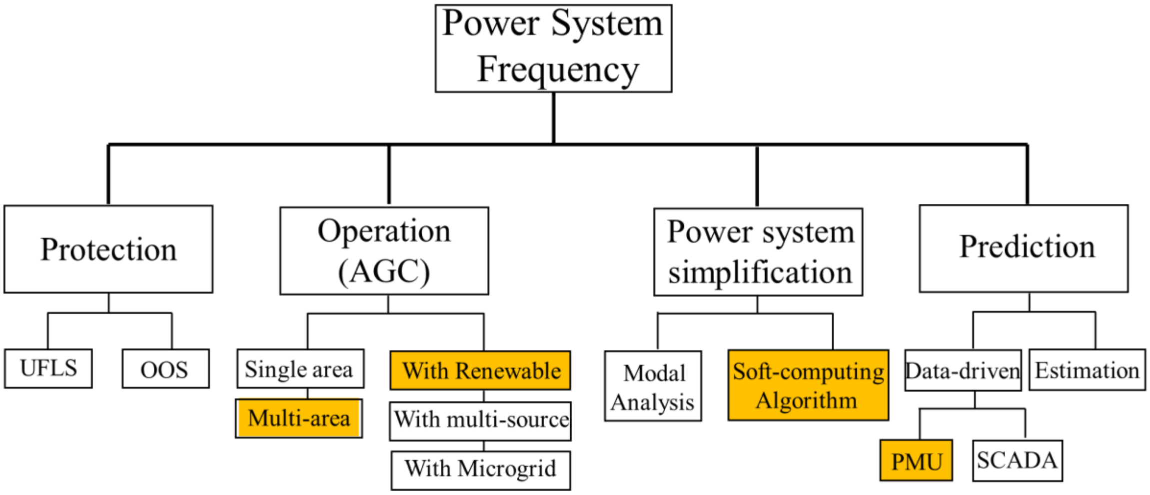

Figure 1.3 Power system frequency research focuses overview from the literature review.

1.4 Power System Benchmark Models

This research studies two IEEE benchmark models, namely the IEEE 2-area 4-machine power system and the IEEE New-England New-York power system. The structure introductions include their general information for further testing.

1.4.1 IEEE 2-area 4-machine Power System

Figure 1.4 presents an IEEE 2-area 4-machine power system model [24-25] with PMU equipped. Four identical generators divide into two areas, and they interconnect by one 230kV transmission corridor. The load is located in both areas with controllable values, which is normally set the area 2 larger for stability analysis convenience.

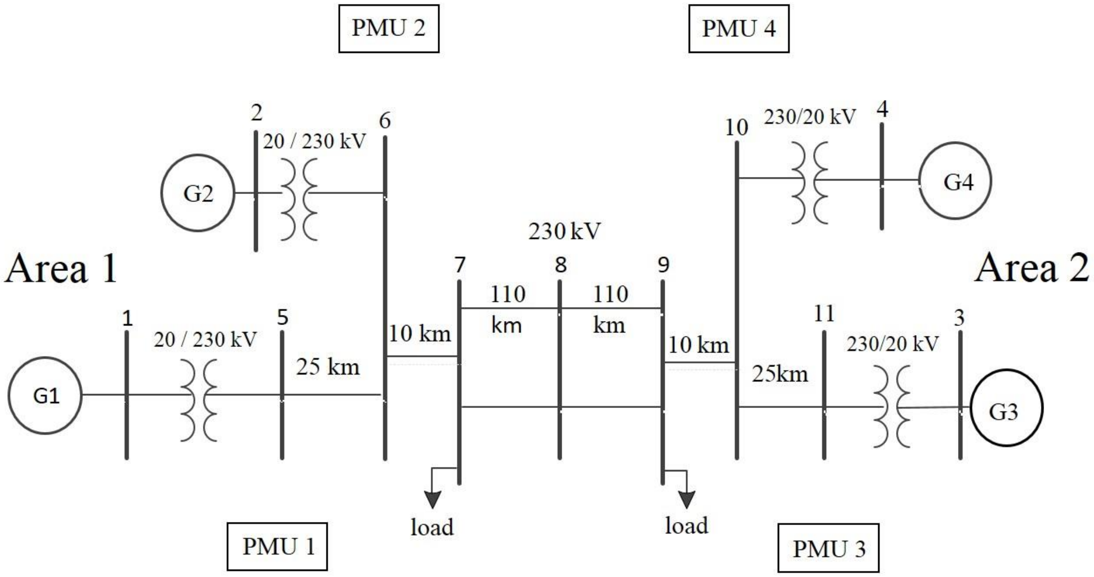

Figure 1.4 IEEE 2-area 4-machine power system [25-26].

1.4.2 IEEE New-England and New-York Power System

The IEEE New-England (NE) and New-York (NY) power system [24], as shown in Figure 1.5, is a widely adopted power system benchmark model for frequency estimation, prediction and stability analysis. It is based on the 1970s actual New England (NE) and New York (NY) power systems with five balancing authorities. The New England power system and New York power system are simulated in detail for 13 generators while the other three exterior systems are modeled by three simplified equivalent generators. Thus, the IEEE NE-NY power system consists of 16 generators, 68 buses, and five controlling areas.

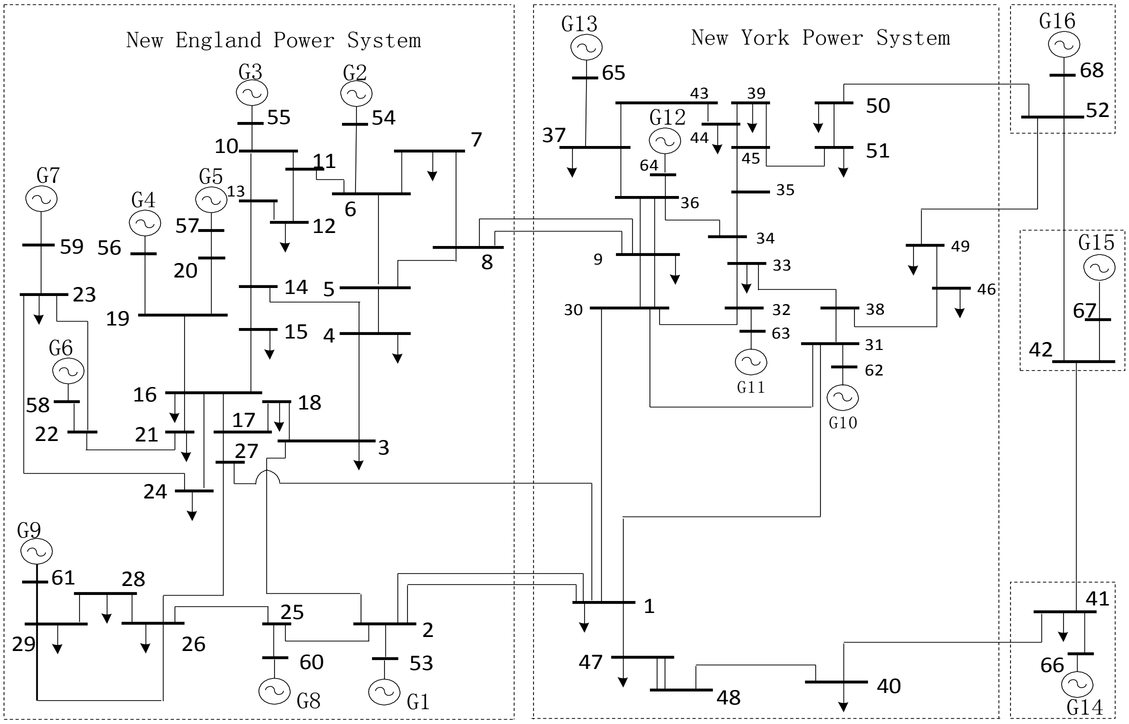

Figure 1.5 IEEE New-England and New-York power system.

1.5 The objective of This Dissertation

The objectives of this dissertation are as follows:

- Develop and implement the new frequency situational intelligence (FSI) methods based on the distributed cellular computational network (CCN) structure, which involves:
    - simulate the IEEE 2-area 4-machine and IEEE New-England New-York benchmark models with PMUs and PVs.
    - Develop new frequency prediction methods based on the CCN.

  - Implement the FSI with different power system models to predict the frequency.
- Develop the frequency coherency group based power system vulnerability index visualization:
  - Develop a multi-area AGC installed 70-bus testbed with utility-scale PV plants and PMUs.
  - Investigate the effects of different PV penetration levels based on the generator online coherency grouping results.
  - Implemented the developed FSI method for multi-area power system real-time coherency analysis
- Develop multi-area AGC parameter practical tuning frameworks suitable for different balancing authorities utilization:
  - Developed a new two-step tuning method for all AGCs in the interconnected power systems.
  - Developed a new asynchronous distributed tuning method for bilateral or multi-lateral AGCs cooperation in the same systems.

1.6 Contributions Outline

The main contributions up to date are shown as follows,

i. Developed and implemented a cellular computational network structure based frequency prediction algorithm for multi-machine power system [27].

ii. Developed and implemented cellular neuron network with different prediction algorithms for multi-machine power systems frequency prediction incorporating with PMUs [28-30].

iii. Developed and implemented a frequency situational intelligence-based method for multi-machine synchronous generator coherency analysis [31].

iv. Developed a new coherent group based generator and power system vulnerability visualization method to analyze the effects of high penetration of utility-scale PV plant in an interconnected multi-area power system [32].

v. Developed and implemented two-step and asynchronous new tuning methods for multi-area AGCs performance improving [33-35].

1.7 Summary

With a rapid renewable energy deployment and penetrated the main grid, the continuous frequency situational awareness of the modern power system control center becomes a must-to-do challenge. Frequency situational intelligence is then developed and implemented with the wide installed PMUs to provide insight and predicted views for operators mitigating the impacts of high penetration of solar energy.

CHAPTER 2

POWER SYSTEM BENCHMARK / TESTBED MODELS

2.1 Overview

In this chapter, benchmark models are first introduced and then modified with PMUs for further frequency prediction methodology adoption. These models include IEEE 2-area 4-machine system and IEEE New-England New-York system. Moreover, the IEEE 2-area 4-machine is modified considering PV plants with actual weather information from Real-time Power and Intelligent Systems (RTPIS) Laboratory weather station at Clemson University. In the end, a novel real-time test bed is developed with utility-scale PV plants and multi-type synchronous generators. All the benchmark models and the test bed model are simulated via the RSCAD software on the RTDS device.

2.2 IEEE 2-area 4-machine Benchmark Models

As aforementioned, the IEEE 2-area 4-machine benchmark model contains four identical synchronous generators separately in two areas. The synchronous generator has a rated value of 20 kV/ 900 MVA [26]. All of the generator machines are considered with primary controllers, notably, turbine governors, automatic voltage regulators (AVRs) and power system stabilizers (PSS). Under steady state conditions, tie-line power flow from area 1 to area 2 is 400 MW [26]. To investigate the system frequency fluctuations within a small and random disturbance, generator voltage regulator combines the pseudo-random binary signal (PRBS) in its reference voltage input channel.

For the 2-area 4-machine model, PMUs are installed at all ‘generator buses’ to measure the dynamic frequency of the synchronous machine, namely Bus 5, Bus 6, Bus 10 and Bus 11. All PMUs are configured with the unified parameters fulfilling the IEEE standard, 30 Hz or 60 Hz sampling rate for frequency measuring.

This 2-area 4-machine is further implemented with utility-scale PV plants, as shown in Figure 2.1. In this model, a 210 MW PV plant [36-37] is integrated in area 2. For each area, automatic generation control is implemented to maintain the steady system frequency in 60 Hz. The PV plant adopts actual weather information from the RTPIS laboratory weather station at Clemson University. The achieved daily weather data is also available at RTPIS website for further investigation.

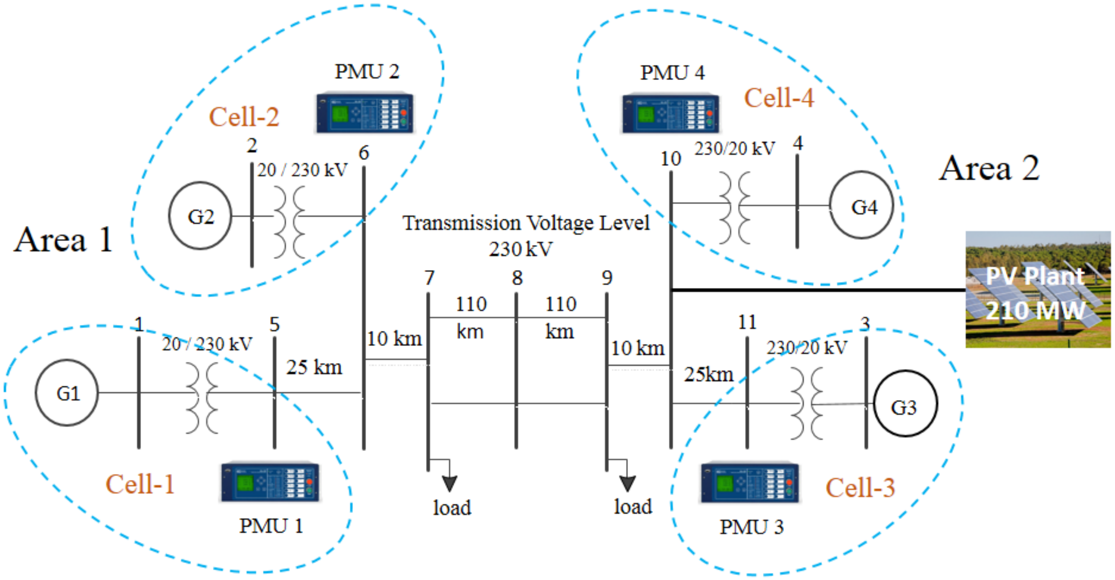

Figure 2.1 IEEE 2-area 4-machine with a 210 MW PV plant.

2.3 IEEE New-England and New-York Benchmark Model

The IEEE New-England New-York benchmark model is shown in Figure 1.5. This is a reduced order equivalent of the interconnected New-England (NE) system and New-York (NY) system. There are five geographical regions out of which NE and NY are represented by a group of generators whereas, import from each of the three other neighboring areas 3, 4, and 5 are approximated by equivalent generator models.

Generators G1 to G9 are the equivalent representation of the NE generation while machines G10 to G13 represent the generation of the New-York system. Generators G14 to G16 are the equivalent generators of the neighboring areas adjacent to NY side. Bus 1 and 2, Bus 1 and 27, as well as Bus 8 and 9 are three major transmission corridors connecting New-England system and New-York system. In the steady-state condition, the tie-line power transfer from New-England to New-York is 560 MW in total.

Further investigating the transient cases, the three-phase line to ground faults are also implemented in this system locating at either Bus 1 or Bus 8. The fault duration time is set to 6 cycles. The IEEE NE-NY benchmark model with faults is shown in Figure 2.2.

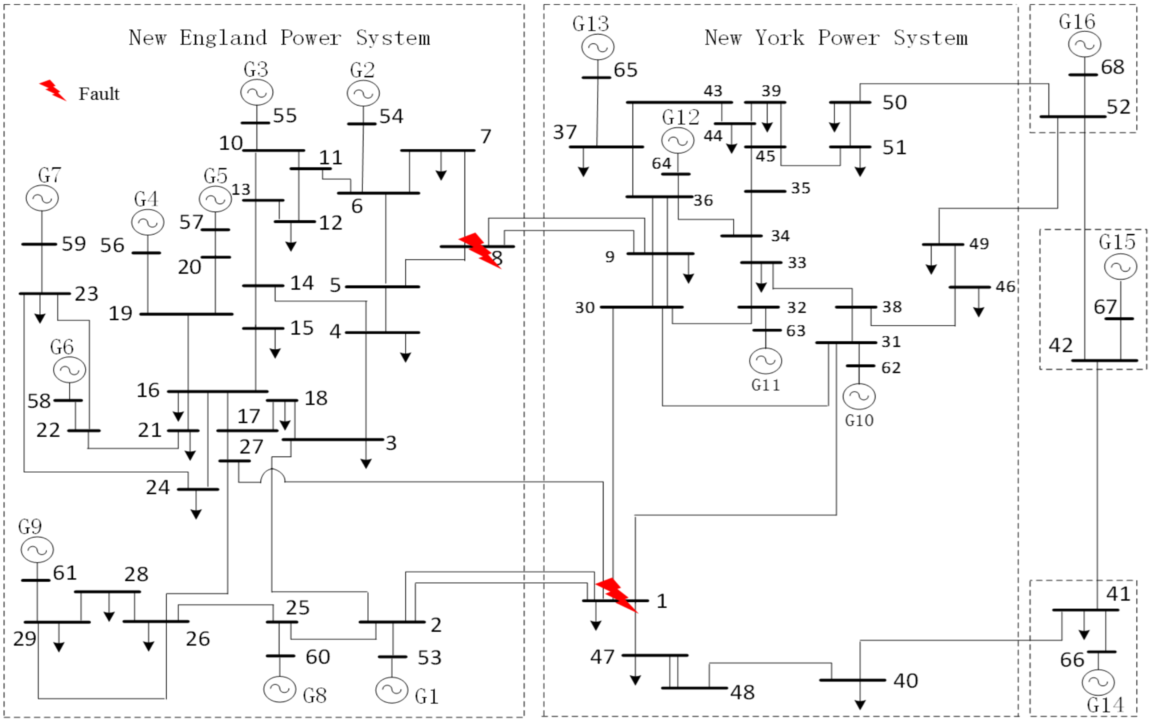

Figure 2.2 IEEE New-England and New-York power system model with tie-line faults.

2.4 Real-time Testbed with Utility-scale PV Plants

2.4.1 Motivations for Testbed with High Penetration of PV Power

As more PV plants connected into the main grid, the mitigation of their intermittent power output has to be adjusted by the other plants, like gas, hydro or coal plant. Besides, maintaining the system-wide frequency stable and security also require a large displacement of the conventional generators due to the consequence of high level PV penetration [18]. This situation has led the conventional power grids to operate towards their frequency security limits, which are more vulnerable to any possible disturbance [19]. The vulnerability of power system with PV power integrated has been the object of many research works in distributed network level [20-21]. These studies investigate the consequences of the PV penetrated power system, and furthermore, the design energy management control block for mitigation. Physical solar plant involved test bed has also been developed for the purpose of investigation [18-20] on the distribution level. The transmission area effects with high penetration PV is a rather ongoing topic [6-7]. It has been introduced in [6] that the high level of PV connected to the grid, the system voltage, and rotor angular stability will be significantly affected. The results have been examined using a various amount of rooftop solar plants and several fixed utility-scale PV plants in a specialized 2419-bus western electricity coordinating council (WECC) system. The solar plants are aggregated and the dynamic voltage and speed profiles of the system has to zoom into a certain part for analyzing.

Furthermore, due to computation and communication latencies, it is prohibitive to carry out detailed as well as holistic grid impact reviews in the aftermath of disturbances. Thus, the power system dynamic frequency responses to different PV penetration situations have to be addressed and discovered through system coherence analysis for model reduction and simplification [22].

2.4.2 Real-time Test Bed with Utility-scale PV Plants

To investigate the effects of PV penetration on multi-machine system dynamic grouping, a test bed with various conventional generation types and utility-scale Photovoltaic (PV) station, is developed as shown in Figure 2.3. The test bed is developed and simulated in RTDS for three racks. It is derived from the classical IEEE New England (NE) – New York (NY) multi-machine power system model [25, 38]. The NE-NY model consists of 68 buses, which is a simplified network of the 1970s New England

and New York five-area interconnected system. Area 1, also known as the New England system, consists of generators from G1 to G9. Area 2, known as the New York system, consists of generators from G10 to G13. Areas from 3 to 5 are aggregated subsystems simulated by generator G14 to G16. Two additional identical utility-scale Solar PV plants are connected to the corresponding New-England and New-York sides by two additional transmission lines and buses, which are named as bus 69 and 70. PMUs are equipped in each terminal of the conventional generator. A brief description of the modified system components is summarized below.

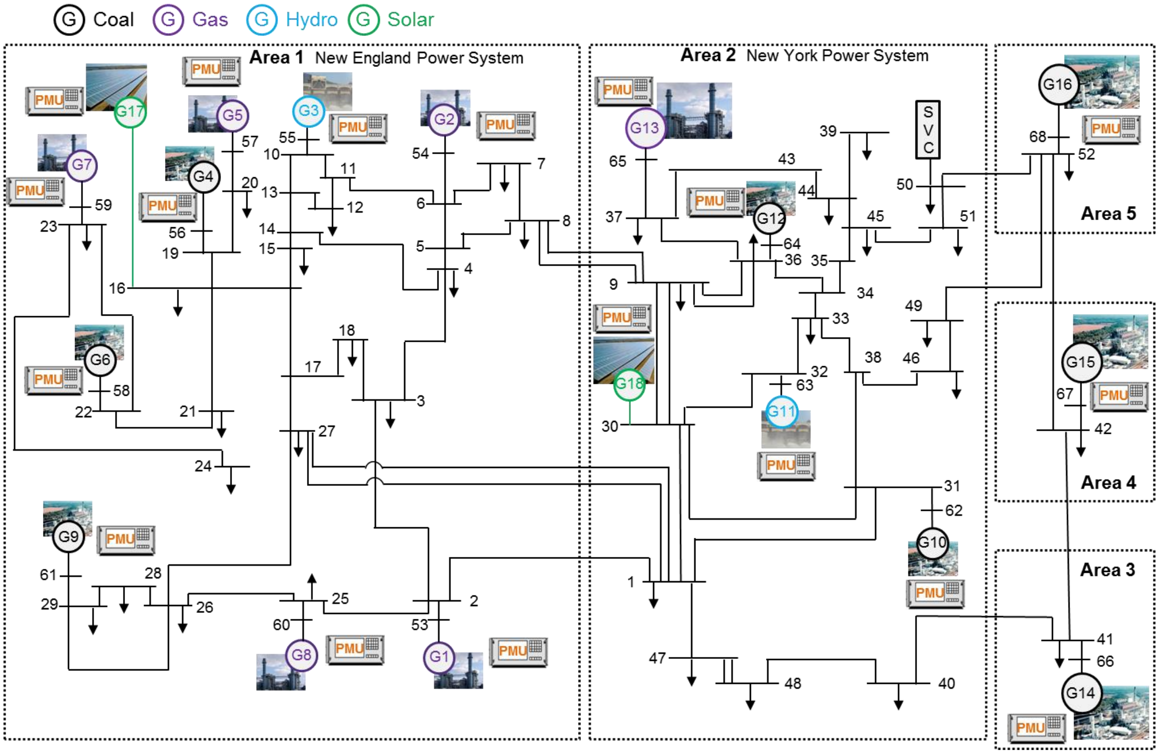

Figure 2.3 The developed test bed with multi-type generators and utility-scale PV plants.

2.4.3 Multiple Generator Types

The standard generators in the IEEE NE-NY power system are modified into three types, namely, coal, gas and hydro plants [38]. The coal plant consists of eight plants as

G4, G6, G9, G10, G12, G14, G15, and G16; the gas plant contains six plants as G1, G2, G5, G7, G8 and G13; and the hydro plants for two as G3 and G11. In this test bed, system frequency is maintained by area generator controls and 8th order synchronous machine models are utilized and applied for all generators mentioned above. The detailed parameters of each synchronous machine are initially derived from [24] and modified for representing the corresponding machine types. Appendix A presents the modified parameters for this testbed.

Synchronous machine's AVR and speed governors are included for all generation units. The block diagrams of the AVR and speed governors are shown in Figure 2.4. The AVR exciters' communication time latency in this test-bed is assumed negligible. The damping torque is enhanced by considering a transient gain reduction feedback block. Ramp rates are set to be different as 1% per minute for coal plants, 5% per minute for gas plants and 5% per second for hydro plants. The detailed AVR and speed governor parameters for all three types of plants are adopted from [25], which are presented in Appendix A.

The test bed system is also equipped with power system stabilizers (PSS) for every conventional generator for improving the damping of the system local and inter-area oscillation modes [39]. The PSSs' parameters are listed in Appendix A and a general block diagram for designing is shown in Figure 2.4.

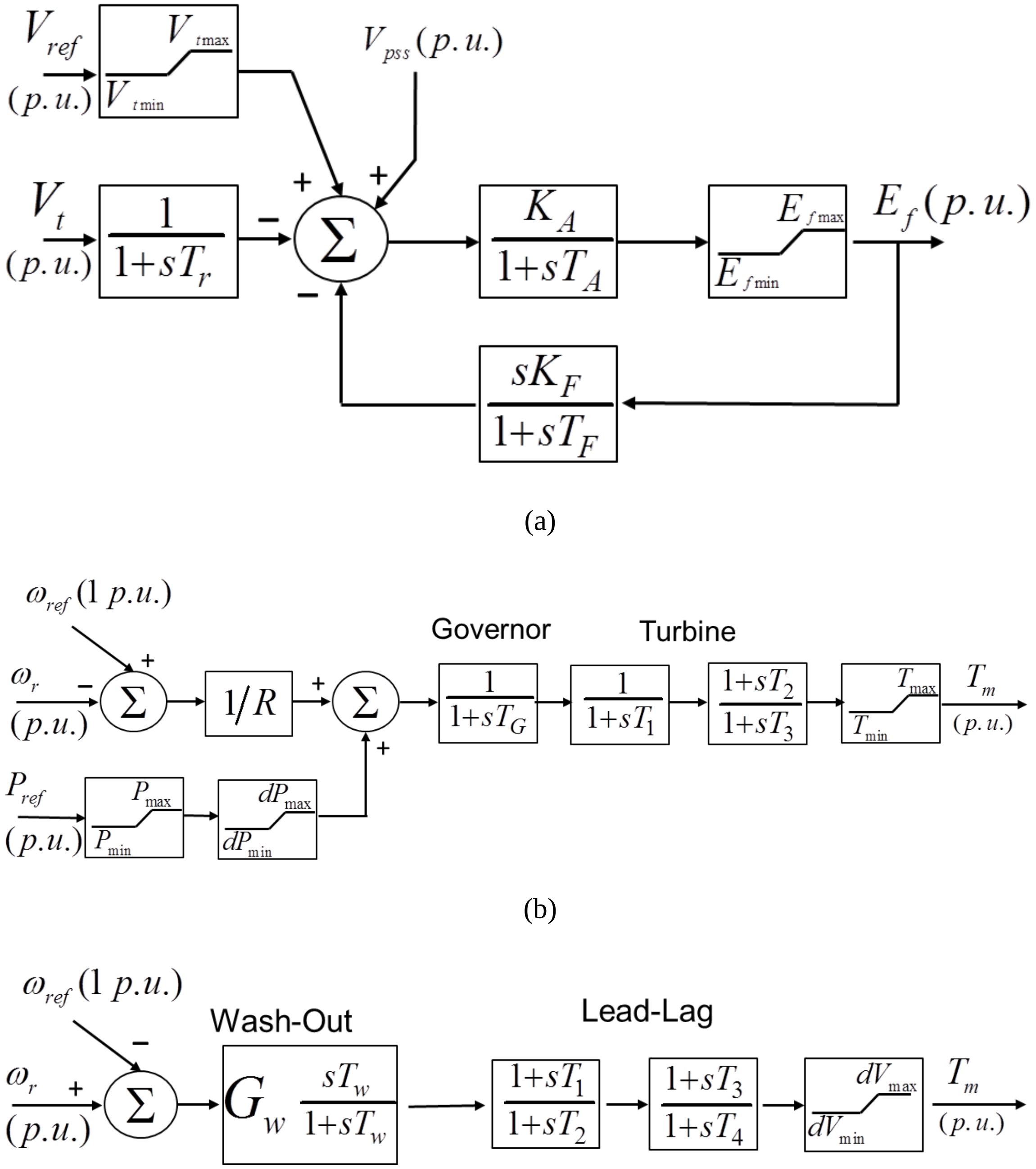

Figure 2.4 The AVR (a), governor control (b) and PSS (c) for the developed testbed.

The test bed load modeling is simplified as impedance models for lowering the RTDS computing burden. The transmission line models are adopted the single-section lumped π model, which neglects the electromagnetic traveling wave effects.

2.4.4 Utility-scale PV Plants

The test bed system is expended with integrating two utility-scale solar PV plants. Solar PV plant G17 has a peak-generation capacity of 1148 MWp and is integrated in New-England area at Bus 16. Solar PV plant G18, which is connected to New-York area at Bus 39, has a peak-generation capacity of 840 MWp. Both PV plants are modeled in Polycrystalline type. The Clemson University weather station real-time data for PV system modeling is shown in Figure 2.5. The PV DC-DC electronic converter is modeled as a controllable voltage source [36] for three-phase connection. External control signals as solar irradiance and temperature are also implemented.

The MPPT algorithm implemented in order to harness the maximum amount of power at each solar irradiance and ambient temperature operating point condition is the Perturb and Observe (P&O) method. While P&O is considered as a slow tracking method and might fail under fast variations in irradiance, its implementation is quite simple in comparison to other conventional as well as novel MPPT algorithms. A passive low-pass filter (LPF) is further installed at the output terminals of the inverter in order to eliminate the high frequency switching harmonics in output current waveform [36-37].

To compensate for the additional solar PV plant integration, the loads in both New England and New-York areas are increased as the Bus 16 and the Bus 24 for 175 MW each; Bus 33 and 45 for 240 MW each. Detailed PV power control algorithms are elaborated in Appendix B.

Within this study, the various PV penetration is carried out using the following equation [6]:

$$\text{Penetration Percentage (\%)} = \frac{\text{Total PV Power (MW)}}{\text{Area Onsite Convention Power (MW)}} \tag{2.1}$$

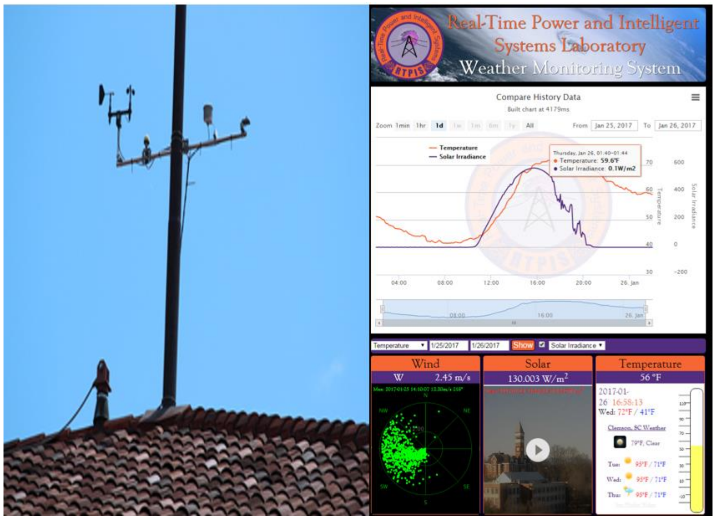

Figure 2.5 Clemson weather station real-time data for PV system modeling.

To compensate for the additional solar PV plant integration, the loads in both New England and New-York areas are increased as Bus 16 and Bus 24 for 175 MW each; Bus 33 and 45 for 240 MW each [38]. The PV integration and corresponding controls are summarized separately in Appendix B.

2.4.5 Test Bed with High Penetration of Solar PV Power

The maximum PV power connected to the NE and NY areas, which is shown in Figure 2.6 (a), is 1250 MW and 1050 MW, respectively. The speed fluctuations for all 16 generators are shown in Figure 2.6 (b). In this case, the maximum PV power penetration is about 22% of the test bed generation capacity. The operating conditions of all 16 generators are summarized in Table 2.1.

Table 2.1 Testbed with high penetration of solar PV power for steady-state situation.

Generator	**Active Power Generation (MW)**	**Generator**	**Active Power Generation (MW)**
G1	194	G9	627.8
G2	427	G10	506
G3	509.3	G11	1195
G4	515.8	G12	1362
G5	396	G13	2698
G6	547.5	G14	5715
G7	438.6	G15	6030
G8	524.2	G16	5471
G17 (PV)	1230	G18 (PV)	1050

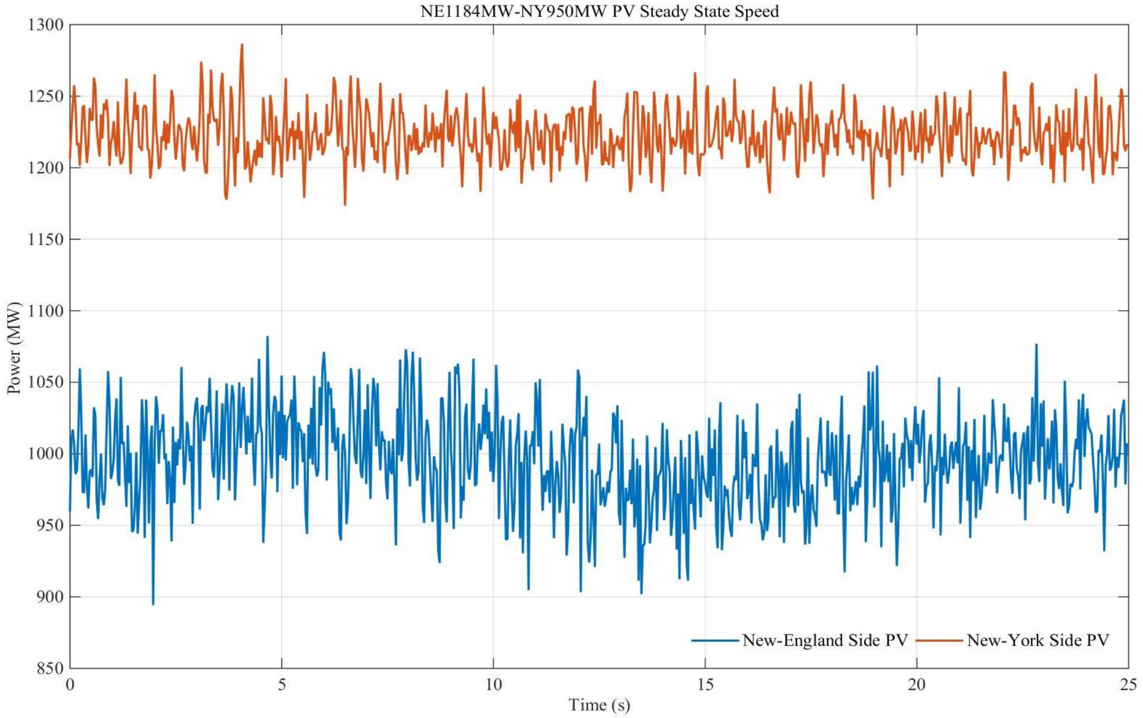

(a)

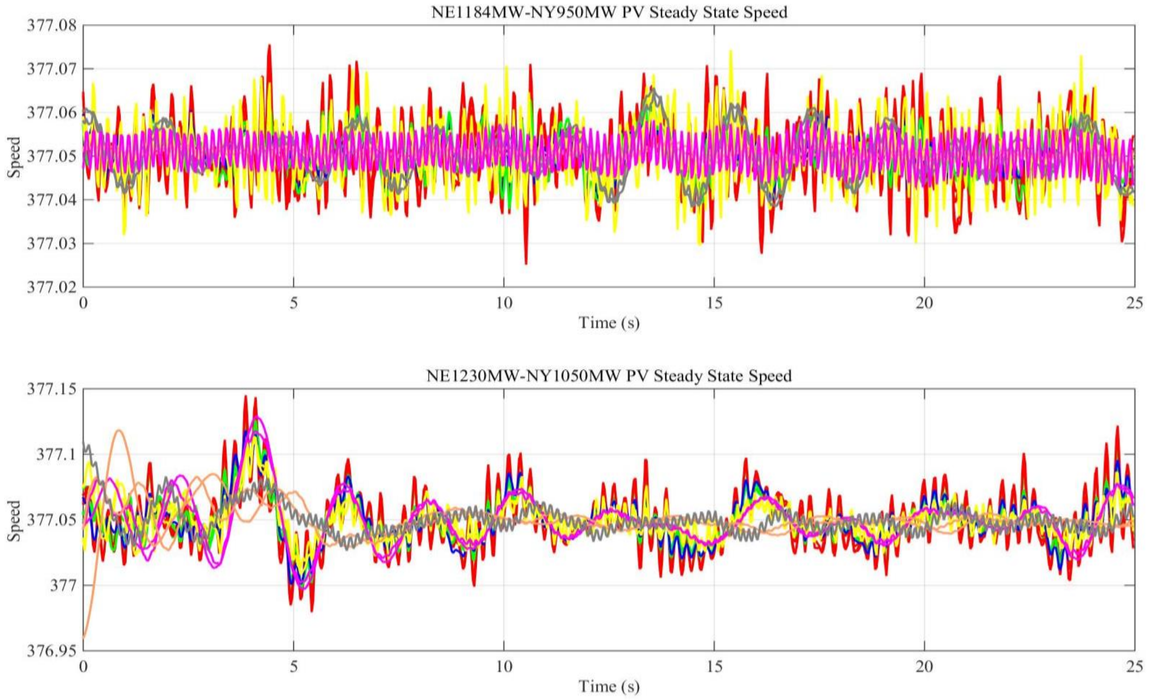

(b)

Figure 2.6 The maximum PV penetration level for the test bed steady state condition (a) and corresponding frequency oscillations for all generators (b).

2.5 Summary

This chapter focused on developing the IEEE benchmark models for following chapter frequency situational intelligence analysis. Furthermore, a test bed is developed with multi-type generators and utility-scale PV power plants. All these models /testbed are adopted for the following chapters' studies.

CHAPTER 3

MULTI-AREA AUTOMATIC GENERATION CONTROLS FOR INTERCONNECTED POWER SYSTEMS

3.1 Overview

In this chapter, the multi-area Automatic Generation Controls (AGC) are developed and implemented in the modified IEEE NE-NY testbed, which includes utility-scale PVs. Frequency fluctuations in the interconnected power system are indications of the load imbalance between the power supply and demand. Whenever a noticeable disturbance occurs, the system frequency deviates from the steady value [40]. The absence of regulation will result in load shedding and continuous generator trips that are detrimental to grid stability and reliability [41]. The primary governor controls are used to manage large disturbances whereas supplement controls as the AGCs are used to manage system frequency disturbances within the standards [42-45].

3.2 Multi-area Automatic Generation Control Models

AGC maintains the steady frequency of the entire system during load or generator disturbance, the U.S standard of which is which is 60 Hz. Multi-area AGCs locate on the generation terminal to regulate the frequency of the corresponding area. The multi-area multi-source test system has a sub-power-system that is a combination of various generations under the same control scheme. Figure 3.1 shows the block diagram of a generalized AGC for area *i* that includes n generators. It is possible to modify this AGC model to manage multiple areas. The tie line power from area *i* to area *j* is expressed as,

$$\Delta P_{tie-i} = \sum_{\substack{j=1 \\ j\neq i}}^{N} \Delta P_{tie-ij} = \frac{2\pi}{s}\left[\sum_{\substack{j=1 \\ j\neq i}}^{N} (T_{ij}\Delta f_i - T_{ij}\Delta f_j)\right] \tag{3.1}$$

$$N = 1, 2, \ldots, m$$

$$T_{ij} = \frac{|V_i||V_j|}{X_{ij}} \cos(\delta_i - \delta_j) \tag{3.2}$$

where ΔP_{tie-i} is the tie-line power deviation; T_{ij} the tie-line synchronizing coefficient between area i and j, N the area numbers, i and j the corresponding area; $|V_i|$ and $|V_j|$ the voltages at equivalent generator terminals of area i and area j; X_{ij} the tie-line reactance between areas i and j; *and* δ_i and δ_j the power angles between areas i and j. Thus, the frequency responses of the power system in Figure 3.1 is expressed as,

$$\Delta f_i = \frac{1}{2H_i + D_i}\left(\sum_{k=1}^{N} M_{ki}\left[\Delta P_{ki} - \frac{1}{R_{ki}}\Delta f_i\right] - \Delta P_{tie-i} - \Delta P_{Li}\right) \tag{3.3}$$

where Δf_i is the frequency deviation; H_i and D_i the generator inertia and damping ratio; M_{ki} the generator governor-turbine control block, ΔP_{Li} the load change in the corresponding area i, and ΔP_{ki} and R_{ki} the k generator power change and speed-droop characteristic in area i.

In a multi-area power system, AGC uses tie-line bias control in which both area frequency and the net interchange power with neighboring areas are regulated. Therefore, Area Control Error (ACE) is utilized for the entire ACG loop. ACE is a linear combination of tie-line power and frequency changes for area i, which is expressed as,

$$ACE_i = \Delta P_{tie-i} + \beta_i \Delta f_i \tag{3.4}$$

where β_i represents a bias factor as can be calculated as follows.

$$\beta_i = D_i + \frac{1}{R_i} \tag{3.5}$$

Where the R_i is set with the 5% response rule for all generators in area *i* and D_i is set with the 1% system response for all generators in the corresponding area *i*.

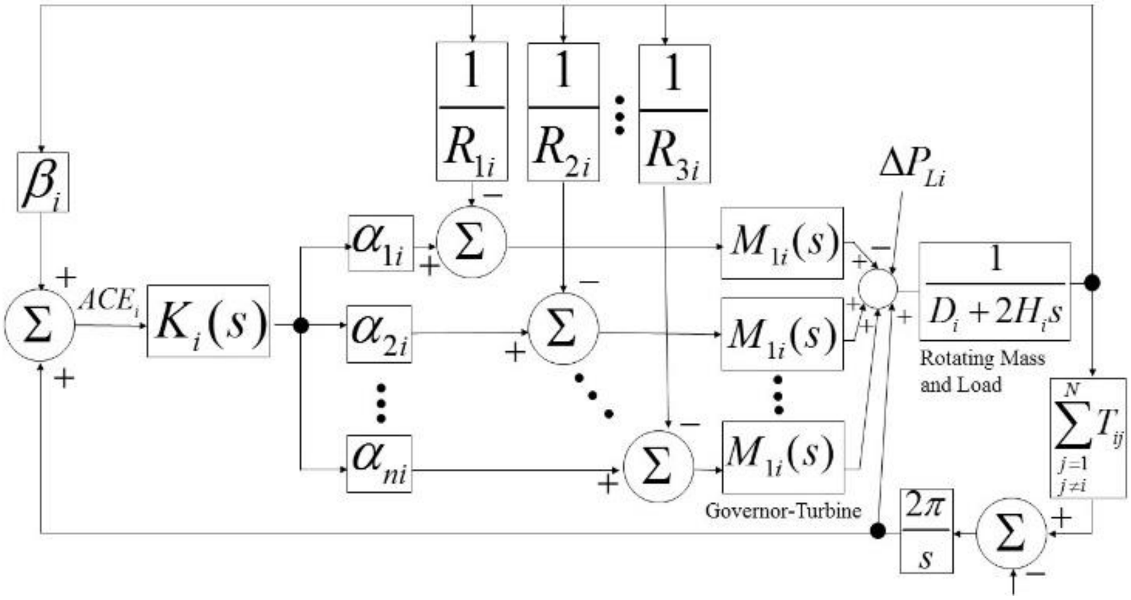

Figure 3. 1 AGC model of area *i* with *n* regulated generators.

3.3 Multi-area AGC Models with PV Power Integration

The integration of utility-scale PVs into a multi-area power system also results in additional system variations that introduce uncertainty. Compared to the load or normal generator disturbances, utility-scale PV power variation is instantaneous with any amount from zero to the rated PV plant power output along with weather changes. Thus, PV power changing effects must be balanced for ACEs. This new ACE that considers PV power for a multi-area power system is expressed as [46].

$$ACE_i = \Delta P_{tie-i} + \beta_i \Delta f_i + (P_{PVactual} - P_{PV\,schedule}) \tag{3.6}$$

where the $P_{pv\ \mathrm{actual}}$ and $P_{pv\ schedule}$ is the PV actual power output and scheduled power output during identical weather conditions.

Mitigating the corresponding impact of the PV integrated power means that the other generators in the testbed must displace certain portions of the power. The functionality of each AGC in its corresponding balancing authority serves as this displacement, based on the generators' participation factors [45-46]. The corresponding block diagrams of the interconnected five-area AGCs are shown in Figure 3.2. Five AGCs, as shown in the AGC diagram in Figure 3.2, in five regions regulate the tie-line power flow and system frequency of 60 Hz together in Figure 3.3.

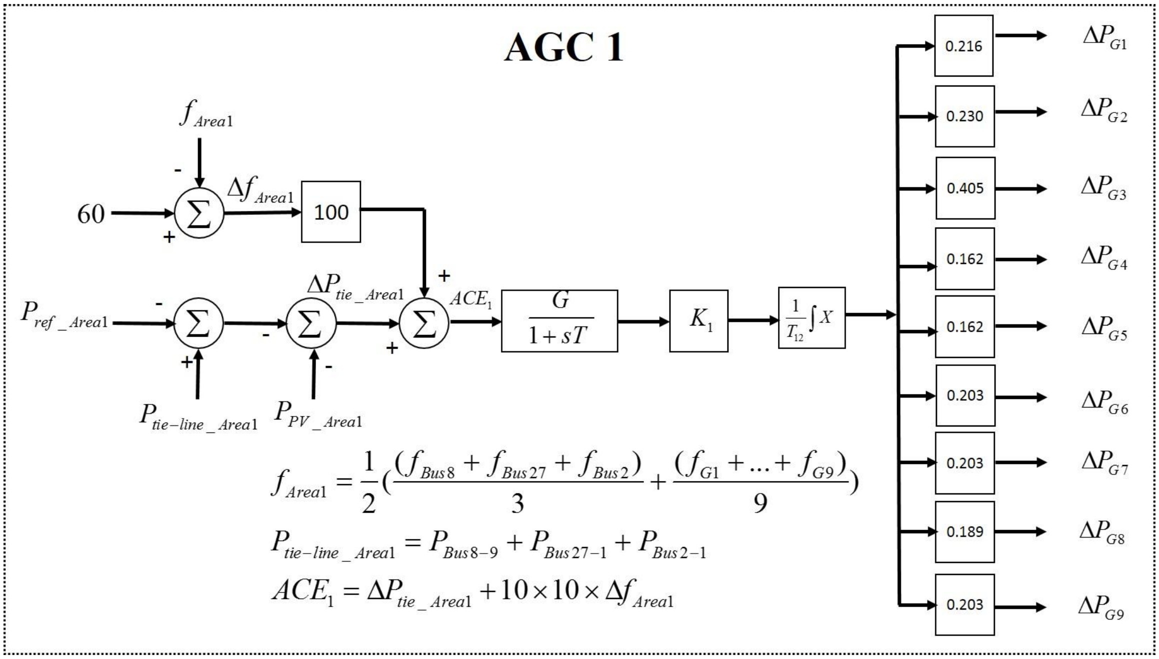

(a)

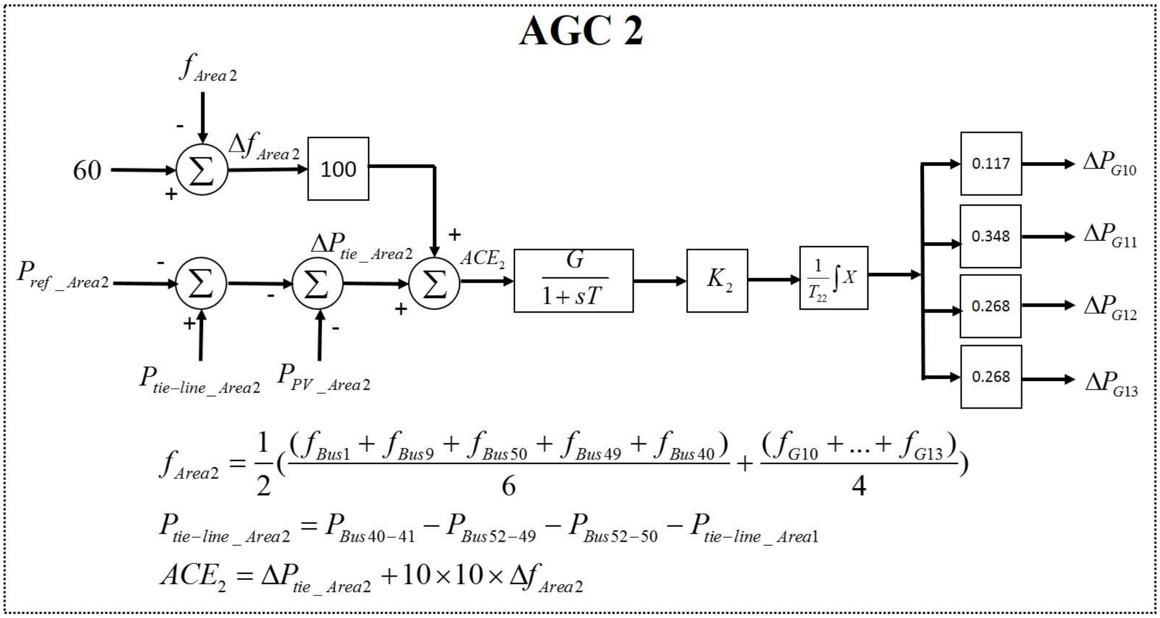

$$f_{Area2} = \frac{1}{2}\left(\frac{(f_{Bus1} + f_{Bus9} + f_{Bus50} + f_{Bus49} + f_{Bus40})}{6} + \frac{(f_{G10} + \ldots + f_{G13})}{4}\right)$$

$$P_{tie-line\_Area2} = P_{Bus40-41} - P_{Bus52-49} - P_{Bus52-50} - P_{tie-line\_Area1}$$

$$ACE_2 = \Delta P_{tie\_Area2} + 10 \times 10 \times \Delta f_{Area2}$$

(b)

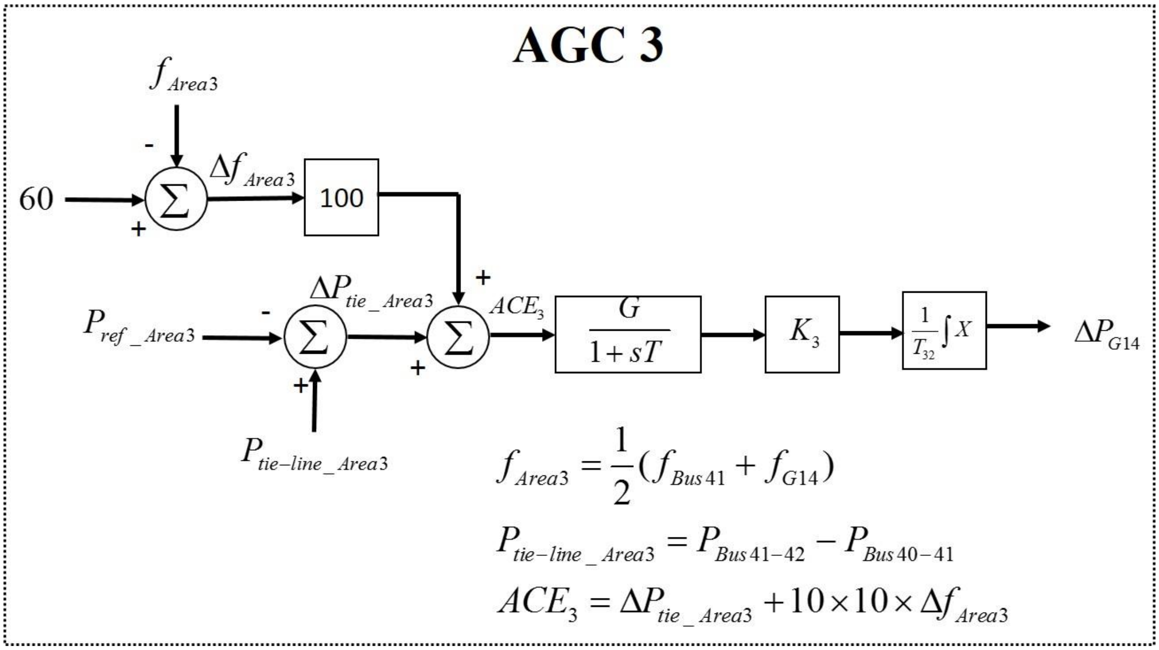

$$f_{Area3} = \frac{1}{2}(f_{Bus41} + f_{G14})$$

$$P_{tie-line\_Area3} = P_{Bus41-42} - P_{Bus40-41}$$

$$ACE_3 = \Delta P_{tie\_Area3} + 10 \times 10 \times \Delta f_{Area3}$$

(c)

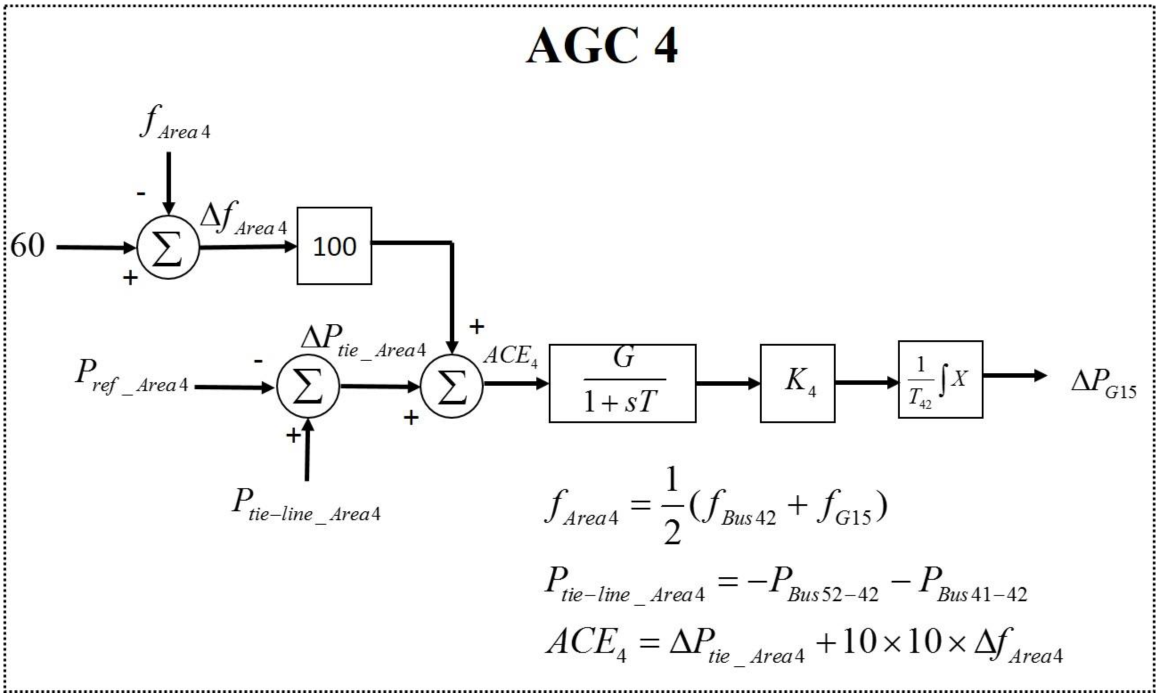

(d)

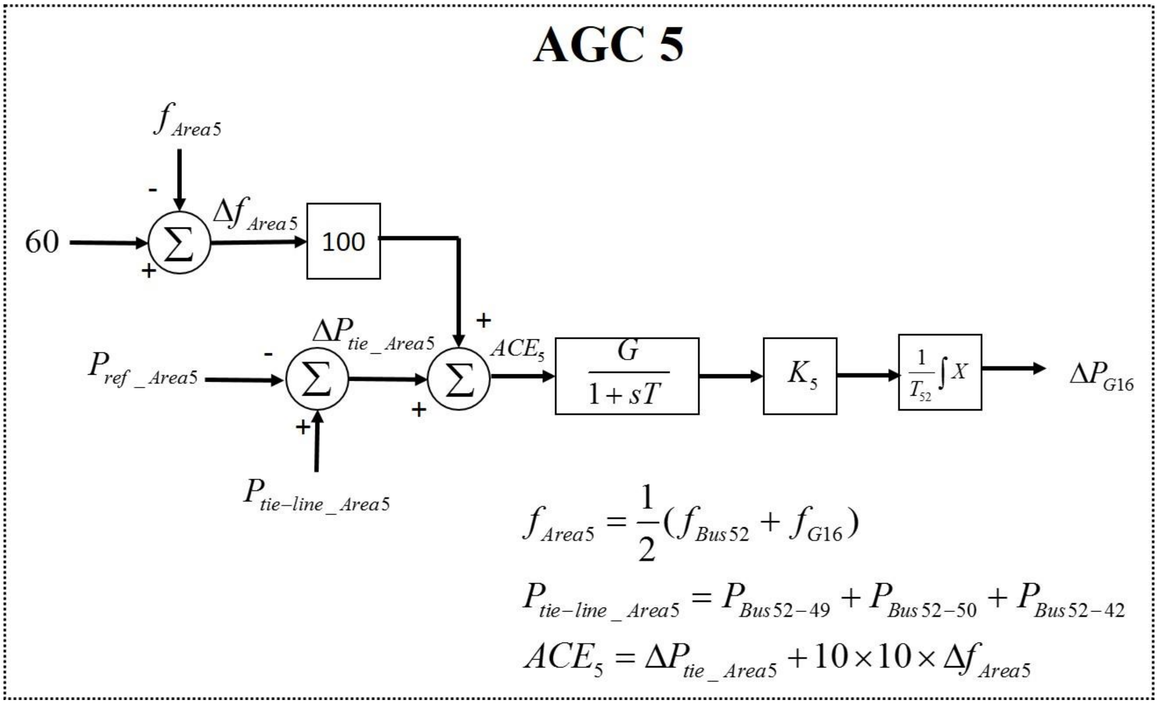

(e)

Figure 3. 2 The AGCs from (a) to (e) corresponding to Area 1 to 5 on the testbed.

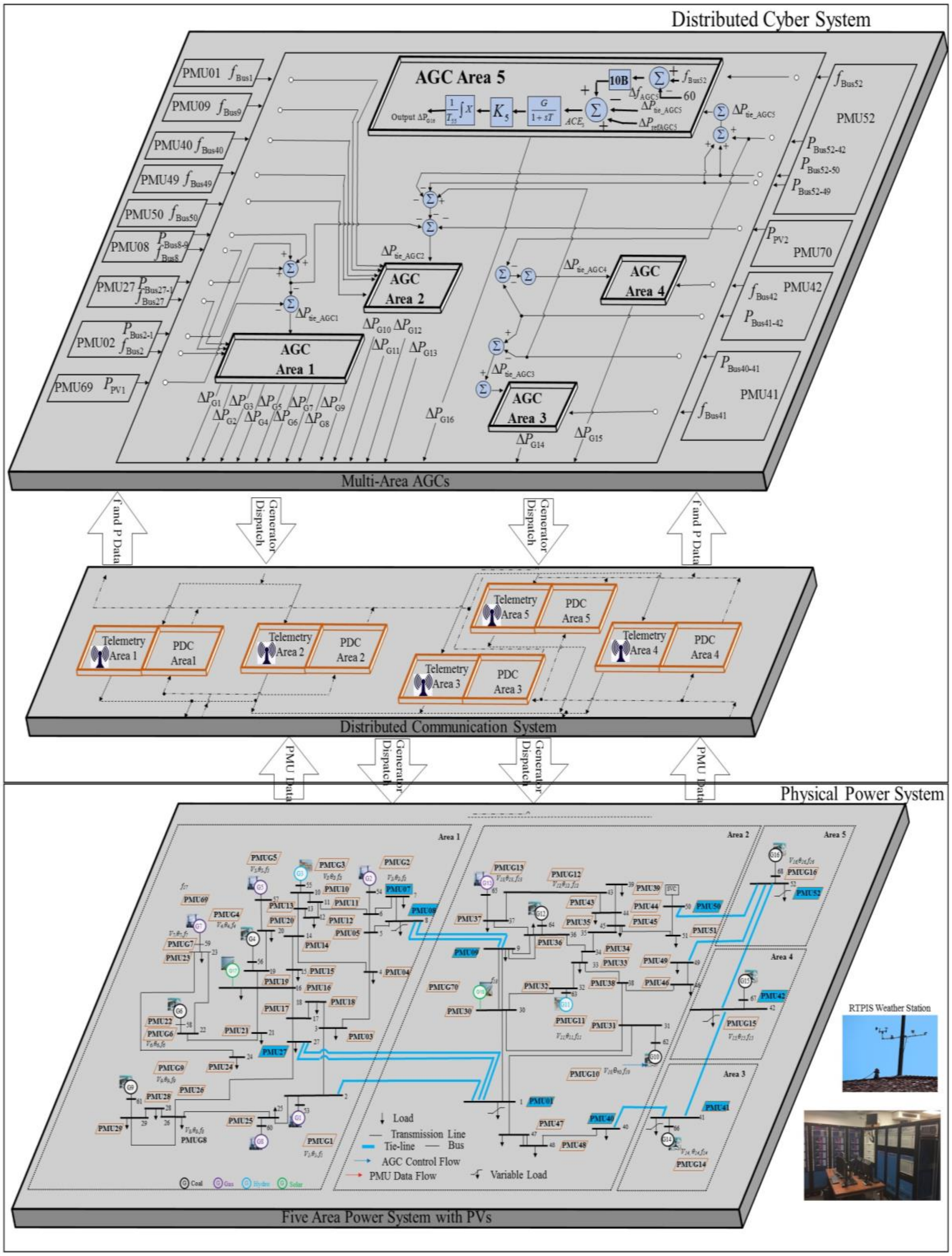

Figure 3.3 Distributed Cyber Control System with Multi-area AGC diagram.

3.4 Summary

This chapter elaborates on developing the multi-area AGC models for interconnected power systems, which are utilized in the following chapters. Furthermore, modified AGCs with PV powers integration considered are also developed for interconnected power system adoption. Eventually, a new distributed cyber control system with multi-area AGCs is presented for the following chapters demonstration.

CHAPTER 4

FREQUENCY SITUATIONAL INTELLIGENCE BASED ON CELLULAR COMPUTATIONAL NETWORK

4.1 Overview

Frequency situational intelligence aims to provide frequency predictions in multi-timescale ahead for grid monitoring, control or protection applications. These frequency predictions can present system behavior, especially during disturbances, in advance and eventually incorporate with other operation analysis functions to deliver fast decisions. In this chapter, the frequency situational intelligence methodology is proposed for multi-timescale frequency predictions based on the cellular computational network approach.

4.2 Power System Frequency Prediction Methods Review

The development of various electrical grid measuring and computing schemes, however, has yielded three types of algorithms: frequency (or model based) estimations, data-based predictions, and soft computing integrated load frequency controls [47]. Regarding model based estimations, the Kalman Filter [48], the Least Square Estimation (LSE) [49], Newton-type algorithms [50], the Fourier method [51] and a hybrid algorithm combined Taylor series expansion and Fourier algorithm have all been used to analytically and independently estimate/predict frequency fluctuations [52]. However, establishing suitable models to provide rigorous estimations via linear methods in a complex power system with a variety of uncertainties remains an unsolved challenge.

Computational intelligence algorithms, however, have been used in an integrated data-oriented approach for the estimation, evaluation and limited prediction of frequencies in post-disturbance scenarios. Specifically, the Neural network (NN) has been used to determine the frequency and corresponding harmonic assessments in real-time [53]. Specifically, a machine learning approach to estimate distributed island grid frequencies has been developed via the integration of NN with decision tree (DT) and entropy networks (EN) [54]. Regression tree [55], and NN with SVR [56] methods have also been developed for predicting frequencies after generator outages or system disturbances. Although these early combinations of data and intelligent algorithms were initially successful, the hardware limitations prevented their use beyond the estimation level, specifically in predicting the frequency behaviors in advance or fixed time intervals.

The creation of the phasor measurement unit (PMU) and frequency disturbance recorder (FDR), used to scan grid frequencies in milliseconds, together with the Wide area Measurement system (WAMS) and Frequency Monitoring Network (FNET), used to coordinated those measurements now characterizes the modern power grid. Contemporary frequency prediction concepts based upon the uncertain basis functions method [57] and Bayesian network structures [58] have been developed based on FDRs in FNET, which is widely used in North America. Internationally, however, the current standard involves the use of a WAMS structure with PMUs.

Renewable energy sources, electric vehicles (EV), and energy storage have also been used to create a coordinated control or soft computing techniques that integrate power system load frequency controls to circumvent the complicated control calculation process. Frequency regulation research includes i) a virtual energy storage system (VESS) integrated control [59], ii) an optimization fuzzy controller using EV for grid wise frequency balancing [60], iii) coordinated control considering large-scale EV charging point and battery devices to restrain frequency oscillations [61]. Soft computing related technique research has been undertaken to use iv) neural network control in nonlinear power systems control [62], v) a least square genetic algorithm and fuzzy inference system to acquire real-time system parameters for control design [63], vi) an online reinforcement method known as goal representation adaptive dynamic programming (GrADP) for the adaptive control of units in an island smart grid [64], vii) type-2 fuzzy logic load frequency controls [65-66], and viii) a hybrid neuro-fuzzy control approach for interconnected system frequency control [67-68]. All of these techniques are suitable alternative methods for controlling future power grids for photovoltaic, wind, electric vehicles and energy storage systems.

4.3 Cellular Computational Network

A cellular computational network (CCN) is a distributed and scalable framework which uses the concept of cells, and adjacent neighbors to simulate a complex system such as a multi-machine power system [69]. For predicting bus frequencies in a multi-machine power system, a CCN must have a similar cell interconnection topology as the power system. Herein, cells communicate first with their directly connected neighbors, referred to as the first-order connectivity. Then, we have second order, third order, and up to n^{th} order connectivity, referring to two cells connected via another cell, two cells connected via two cells, and two cells connected via *n*-1 cells. The cellular interactions in a CCN make it a suitable framework for frequency situational intelligence in a multi-machine power system. The power system topology determines the interconnection of cells in a CCN framework. Any perturbation sensed by a computational cell propagates over time from the disturbance cell to all other cells via intercellular communications. That is to say, the generator frequency predictions are influenced by any disturbance that occurs anywhere within the power system, even if distant.

Cells in a generalized CCN utilize data from the physical system that is either current, past or both as inputs, *I(t)*. Furthermore, predicted data from neighboring cells are as used as additional inputs. The output of a CCN cell can be an estimated or predicted variable of the physical system, $\hat{O}_i(t)$. Thus, for a CCN with m cells and each cell contains j neighbors based on the physical system topology ($j \in [1, m-1]$), the predicted output, $\hat{O}_i(t+k)$, for a random cell *i* at the time (*t*+*k*) is given in (4.1). Herein, *f* is a non-linear function such as a neural network, *k* is the prediction time step, *n* is the number of time steps, a_j is a coefficient based on the strength of the correlation between connected cells.

$$\hat{O}_i(t+k) = f(a_iO_i(t),\ a_iO_i(t-k),\dots,a_iO_i(t-nk),\ a_iI_i(t), a_j\hat{O}_j(t)),\ i=1\ldots m,\ j=1\ldots m-1 \quad (4.1)$$

A CCN cell has three units: computing, learning, and communication. Within the CCN framework, the cells are to exploit local and neighborhood information to minimize the error between the actual cell output and the predicted one, as can be seen in Figure 4.1.

A generalized CCN framework for synchronous generator frequency predictions in a two-area four-machine power system is used for testing. In this study, the generalized neurons and the multi-layer perceptron are used as computing units. These are described below.

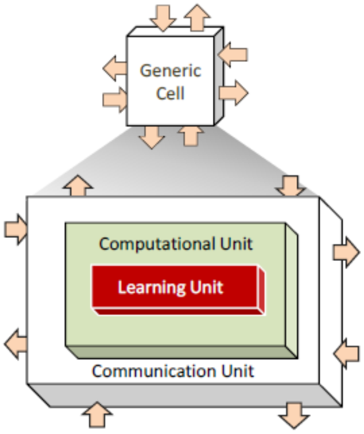

Figure 4. 1 A general description of a cell in the CCN structure [69].

4.4 CCN Computing and Learning Algorithms

4.4.1 Multi-layer Perceptron for CCN Computing Unit

Multi-layer perceptron (MLP), a feedforward neural network, that maps input data sets onto a set of appropriate outputs, is used the primary CCN computation unit. An MLP architecture for frequency prediction, one timescale ahead, is shown in Figure 4.2.

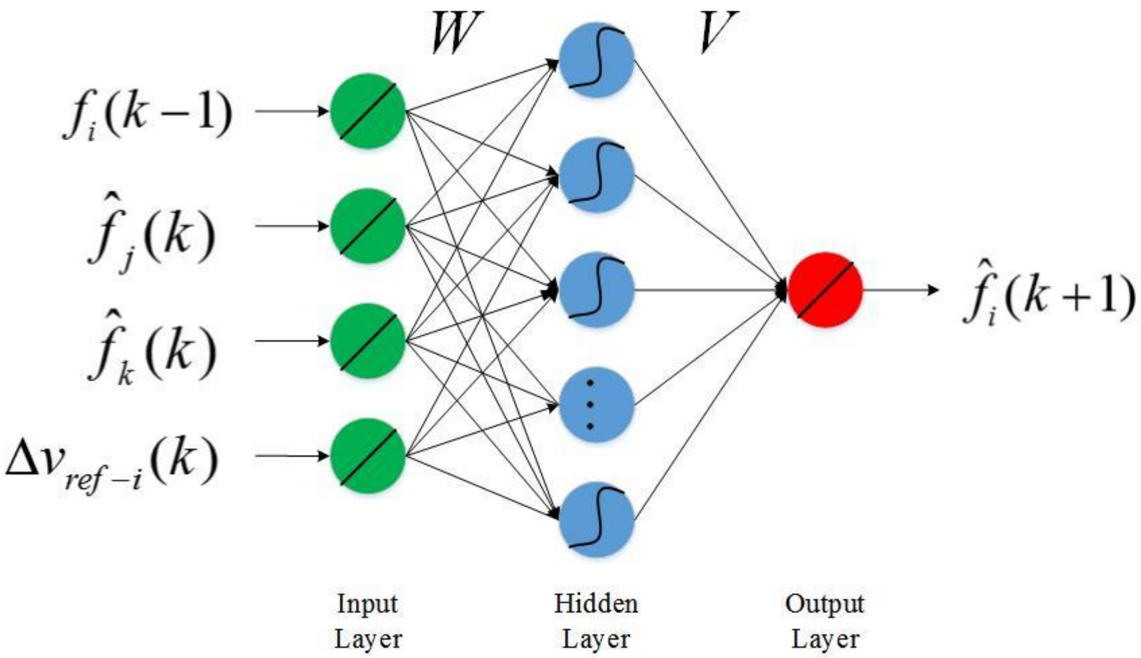

Figure 4. 2 A general structure of the Multi-layer perception.

For predictions in k time step ahead of t, the input *I(t)* is fed via the corresponding weights W in the input layer to each neuron in the hidden layer. The activation computing the nonlinear inputs is expressed as (4.2).

$$a_i(t) = W \times I(t) \tag{4.2}$$

where $I(t) = \{ f_i(t),\ f_i(t-1\times k),\ f_i(t-2\times k), \Delta Vref_i(t),\ \hat{f}_j(t+k),\ \hat{f}_k(t+k)\}$.

The activation procedure in the hidden layer computes the inputs through a sigmoidal function for the hidden layer output $D_i(t)$, is expressed as

$$D_i(t) = \frac{1}{1+e^{-a_i(t)}},\ i \in \{1,2,...,m\} \tag{4.3}$$

where m is the number of neurons in a hidden layer. The predicted frequency is then computed with the corresponding weights in the output weight V. The frequency prediction of an MLP is then processed as:

$$\hat{f}_i(t+k) = (V \times D_i(t))^T \tag{4.4}$$

The output error e_0 is computed as

$$e_0(t) = f_{ref-i}(t) - \hat{f}_i(t) \tag{4.5}$$

where $f_{ref\text{-}i}$ is the actual measurement at time instant t. Note that the error calculation is based on the current data which will be delayed comparing to the predictions for k steps.

4.4.2 Generalized Neuron for CCN Computing Unit

The generalized neuron (GN) is a compact and powerful neuron capable of learning nonlinear functions. The output of the GN is computed from a linear summation of the outputs of two nonlinear activation functions whose inputs are fed from a summation and product, respectively [70]. The activation functions, a sigmoid and a Gaussian, are as shown in Figure. 4.3.

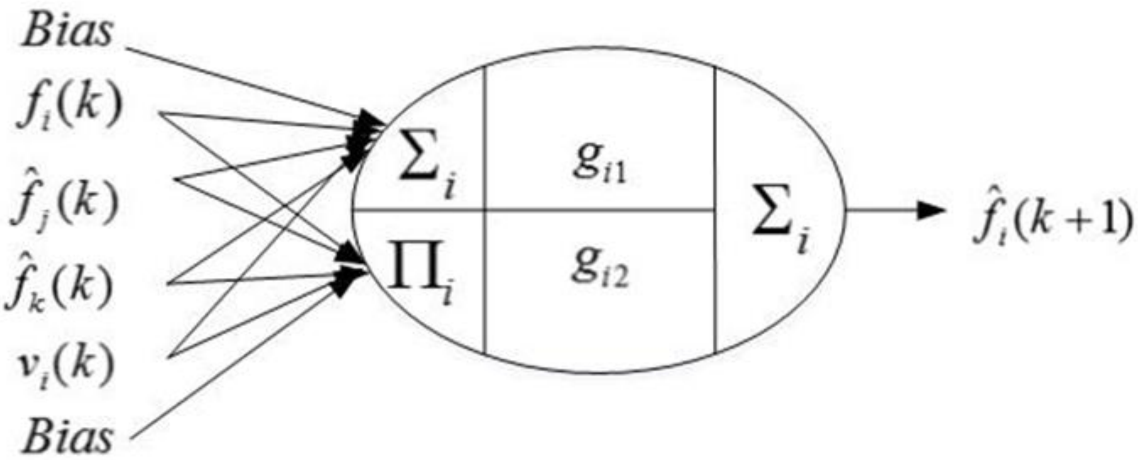

Figure 4. 3 A general structure of the generalized neuron.

As can be seen in Figure 4.3, $\sum_i$ and $\prod_i$ are adopted for the GN for frequency prediction, one timescale ahead. The GN model can be represented by (4.6), (4.7) and (4.8). In (4.6), g_{i1} is a sigmoid function, whereas in (4.7), g_{i2} is a Gaussian function.

$$O_{\Sigma i}(t+k) = \frac{1}{1+e^{-\lambda_s g_{i1}}} \tag{4.6}$$

where $g_{i1} = \sum_{i=1}^{n} W_{\Sigma i} \times X_i(t+k) + X_{o\Sigma}$.

$$O_{\Pi i}(t+k) = e^{-\lambda_p g_{i2}{}^2} \tag{4.7}$$

where $g_{i2} = \prod_{i=1}^{n} W_{\Pi i} \times X_i(t+k) \times X_{o\Pi}$.

In (4.6) and (4.7), X_i (t+k) and $X_{o\sum}$ (t+k) represent the input and bias, respectively, for the summation part of the GN; $W_{\sum i}$ is the weight which is related to the input of $\sum_i$ part. X_i (t+k), $X_{o\prod}$ and $W_{\prod i}$ represent the input, bias, and weight, respectively, for the product part of the GN.

The final output $\hat{f}_i(t+k)$ is a summation of the two calculated terms multiplied by weights W and (1-W) in (3.8).

$$\hat{f}_i(t+k) = O_{\Sigma i} \times W + O_{\Pi i} \times (1-W) \tag{4.8}$$

The output error, e_{GN}, is computed as follows:

$$e_{GN}(t) = f_{ref-i}(t) - \hat{f}_i(t) \tag{4.9}$$

where $f_{\text{ref-i}}$ is the actual measurement at time instant t. Note the error calculation is based on the current data. The error is calculated using particle swarm optimization, described below, to learn the weights mentioned above.

4.4.3 Particle Swarm Optimization for CCN Learning Algorithm

The particle swarm optimization (PSO) is adopted for training the parameters (weights) of the learning units in the cellular computational generalized neuron network (CCGNN) and cellular computational multi-layer perceptron network (CCMLPN). PSO is a popular evolutionary-like, swarm intelligence algorithm used for searching near-optimal global solutions [70-71]. Similar to a parallel optimal result searching approach, PSO models the dynamic social behavior of a flock of birds, which is defined as a particle in a swarm society. A PSO system, therefore, contains an entire society of solutions to a specific problem as involving particles together. Each particle explores an n-dimensional hyperspace in search of the global solution by adjusting its position and velocity according to its historical behaviors and that of its neighbors. A predefined fitness function (or cost function) is utilized to compare the performance of particles in society. For every iteration, the particles' velocity and position are updated to strive to achieve the minimum fitness (in this study, the mean square error).

The learning process of a two-dimensional PSO algorithm is presented in Figure 4.4 in which X_{id} and V_{id} represent the position and the velocity of i_{th} particle in a d dimensional space. The variable P_{bestid} is the local best value of each particle in its history and the G_{bestid} is the global best weight for all particles. To initialize the PSO algorithm, the position and velocity of each particle are randomly assigned within fixed boundaries. In every iteration, particles move to their local best (P_{bestid}) position and then update to the global best (G_{bestid}) location.

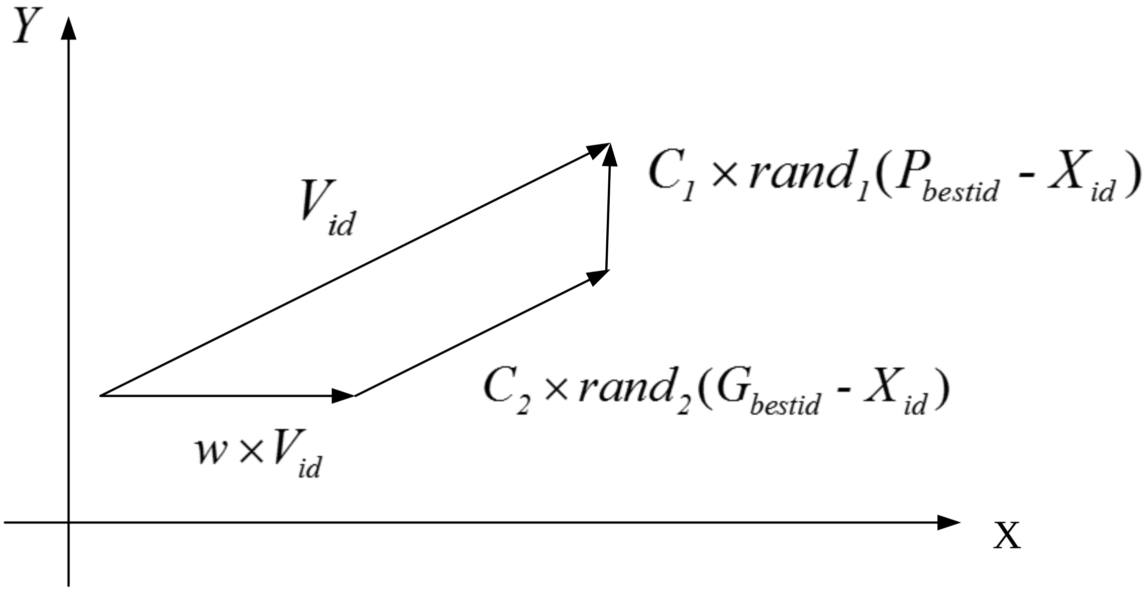

Figure 4. 4 A general description of the PSO algorithm.

The influence of a particle's historical behavior and that of the global best in the swarm upon the velocity of a particle is expressed by (4.10).

$$V_{id}(r+1) = wV_{id}(r) + C_1\, rand_1(P_{bestid}(r) - X_{id}(r)) + C_2\, rand_2(G_{bestid}(r) - X_{id}(r)) \tag{4.10}$$

where r is the iteration index and w is the inertia weight, C_1 is a cognition acceleration constant, C_2 is a social acceleration constant, and $rand_1$ and $rand_2$ generate two random values from a uniform distribution within the range [0, 1]. After the velocity calculation is completed, the particle position is updated via (4.11).

$$X_{id}(r+1) = X_{id}(r) + V_{id}(r+1) \tag{4.11}$$

Trial and error methods have been utilized to determine other GN and PSO parameters. For the PSO algorithm, the values of the maximum velocity and searching boundaries depend on the problem limitations, which also result in a variance of particle numbers. Although a higher number of particles to enhance the search performance, it also increases the computational time, thus requiring a consideration of the trade-off between the two.

4.5 Power System Frequency Prediction Using CCN

The CCN for one timescale ahead frequency prediction of synchronous generators in a multi-machine system can be presented as follows [27],

$$\hat{f}_i(t+k) = f\{f_i(t), \Delta V_{ref-i}(t),\ f_i(t-k),\ f_i(t-2k),\ \hat{f}_j(t)\},\ i=1\ to\ n,\ j=1\ldots m-1 \qquad (4.12)$$

where $\hat{f}_i(t+k)$ is the k time step ahead frequency prediction for the generator *i*. $\Delta V_{ref\text{-}i}$ represents the reference voltage of Cell *i* in the system; $f_i(t\text{-}k)$, $f_i(t\text{-}2k)$ refers to the frequency at previous (k) time step before, and $\hat{f}_k(t)$ represent the corresponding predicted the frequency of the neighboring cells for time (t).

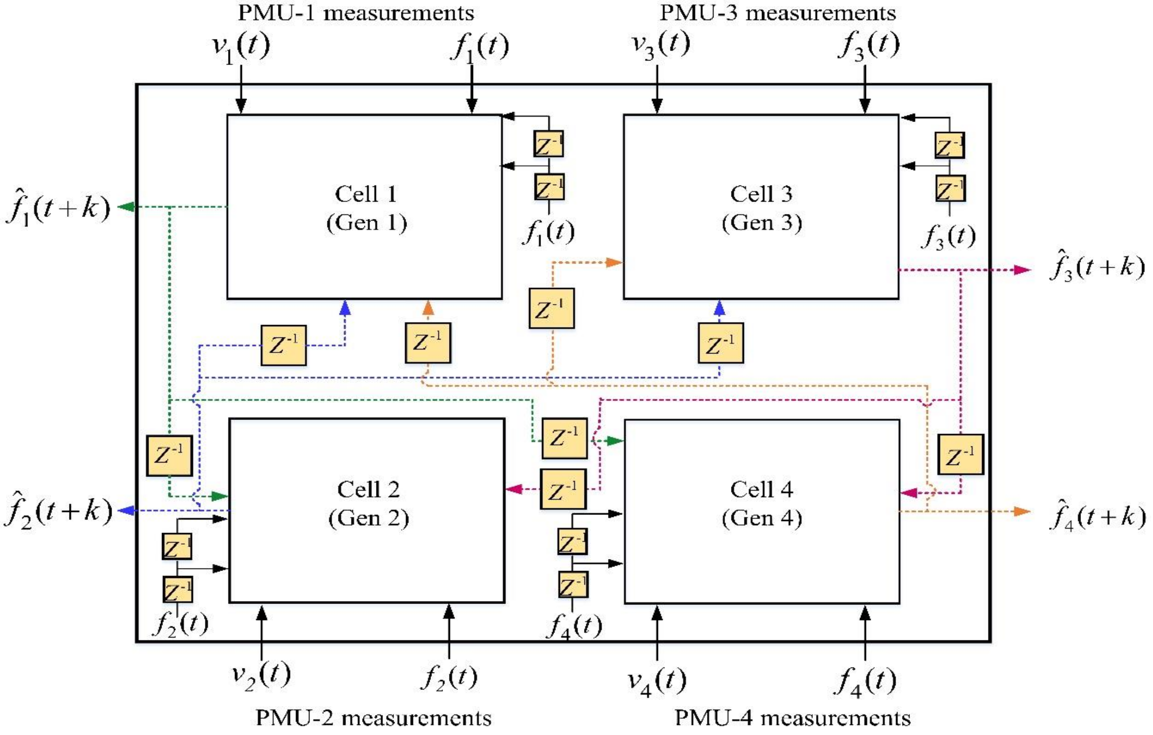

Figure 4. 5 A general CCN structure for the IEEE 2-area 4-machine system.

4.6 Prediction Performance Metrics

The absolute percentage error (APE) and mean absolute percentage error (MAPE), as defined in (4.13) and (4.14), respectively, are used as a measure of fitness to compare the performance of the CCGNN and CCMLPN The performance metric (P_m) and normalized P_m as defined in (4.15) and (4.16), are used for evaluating the effectiveness of CCN based frequency situational intelligence. Herein, P refers to the entire CCN's trainable parameters; T is the entire training time and N is the sample number Moreover, the normalized P_m is adopted for CCGNN to distinguish its performance comparing to CCMLPN. A higher P_m value stands for a better performance of the corresponding CCN architecture.

$$APE = \left| \frac{(f_i(t) - \hat{f}_i(t))}{f_i(t)/60} \right| \times 100\% \tag{4.13}$$

$$MAPE = \frac{1}{N} \sum_{i=1}^{N} \left| \frac{(f_i(t) - \hat{f}_i(t))}{f_i(t)} \right| \tag{4.14}$$

$$P_m = \frac{1}{P \times MAPE \times T} \tag{4.15}$$

$$Normalized\ P_m = \frac{P_{m\_CGNN}}{P_{m\_CMLPN}} \tag{4.16}$$

4.7 Summary

This chapter focused on developing a general frequency situational intelligence methodology. With the help of CCN structures, the FSI is distributed and scalable for multi-machine power systems. In the following chapter, the FSI is applied for different benchmark models and multi-timescale frequency prediction performances are summarized for demonstration.

CHAPTER 5

FSI FOR POWER SYSTEMS

5.1 Overview

As aforementioned, in this chapter, the proposed frequency situational intelligence methodology is applied to multi-machine power systems. First, the proposed FSI is applied to the IEEE 2-area 4-machine power system, the IEEE New-England New-York power system and modified 2-area 4-machine with Solar PV plants to test the performance in multi-machine systems. Different Events, including small disturbances and three-phase bus faults, are created to generate the different scale of system frequency stable oscillations for prediction accuracy validation. Moreover, actual solar irradiance changings collected by Clemson University Real-Time and Power Intelligence System (RTPIS) laboratory weather station are applied for a practical frequency prediction examination.

5.2 FSI for the IEEE 2-area 4-machine System

The FSI method is first applied for IEEE 2-area 4-machine system (Figure 1.4), which is introduced in Chapter 2.2. The CCGNN and CCMLPN used in this study are shown in Figures 5.1 (a) and 5.1 (b), respectively.

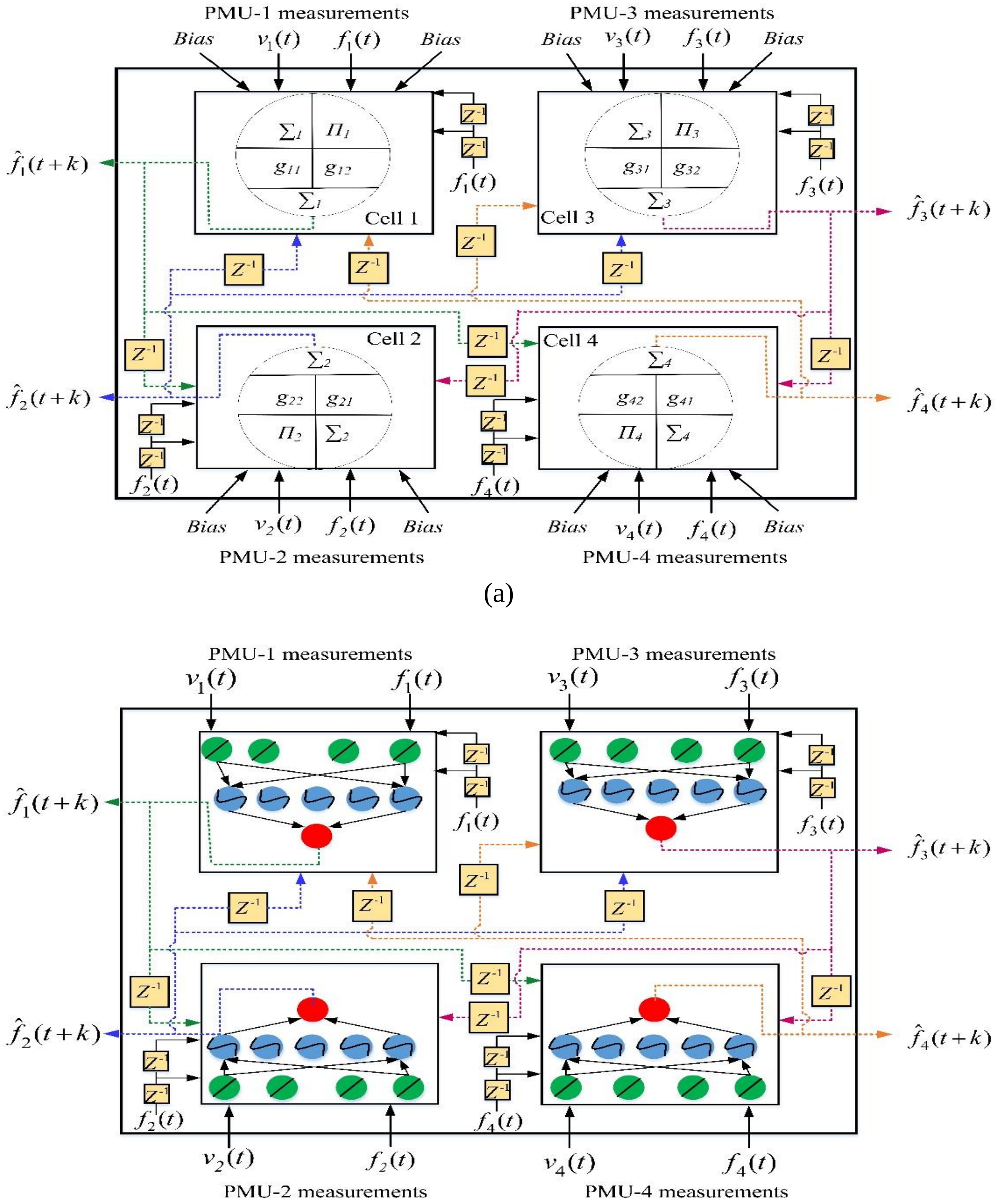

(a)

(b)

Figure 5.1 The two CNN frameworks for the two-area four-machine power system with PV shown in Figure 1.5: (a) The CCGNN framework for the two-area four-machine power system frequency prediction; (b) The CCMLPN framework for the two-area four-machine power system frequency prediction.

In this two-area four-machine test power system, CCN based FSI were initially adopted and verified along with a comparison of the corresponding performance metrics of CCGNN and CCMLPN. The frequency oscillations generated in this system were generated through a pseudo-random binary signal (PRBS) added to the reference voltage for each generator, shown as a random perturbation in Figure 5.2. PMUs were used to capture all four generator frequencies and voltages. During the training process, 220 frequency and reference voltage samples, a 7.2 seconds data, have been utilized for both CCGNN and CCMLPN network learning. The training process was terminated when the iterations requirements were fulfilled. The PRBS generated reference voltage perturbations, and the captured frequency oscillations are shown in Figure 5.2 over a 30-second interval.

The CCGNN and CCMLPN based 100 *ms* ahead frequency predictions for three operating conditions (967 MW-1767 MW, 900 MW-1500 MW, and 920 MW-1380 MW, respectively) are shown in Figure 5.3 for the 10-second interval CCGNN and CCMLPN 33.3 *ms* and 100 *ms* ahead frequency predictions. P_m and normalized P_m are summarized in Table 5.1. As can be seen, the CCMLPN consumes 1184 seconds over 200 epochs training while the CCGNN is 334 seconds for 33.3 *ms* ahead prediction. The overall MSE, time and normalized P_m comparisons as summarized in Table 5.1 demonstrate the CCGNN yields a superior option of FSI than CCMLPN in small-scale power system test.

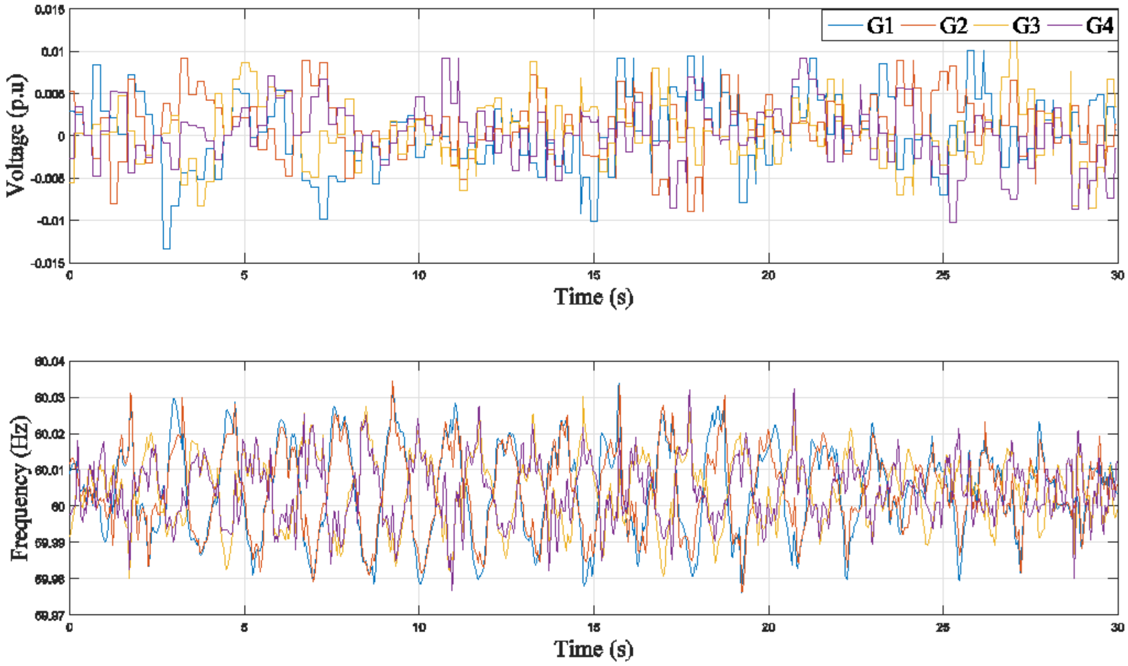

Figure 5.2 The frequency and the reference voltage 30 seconds variation curve for CCGNN and CCMLPN frequency prediction.

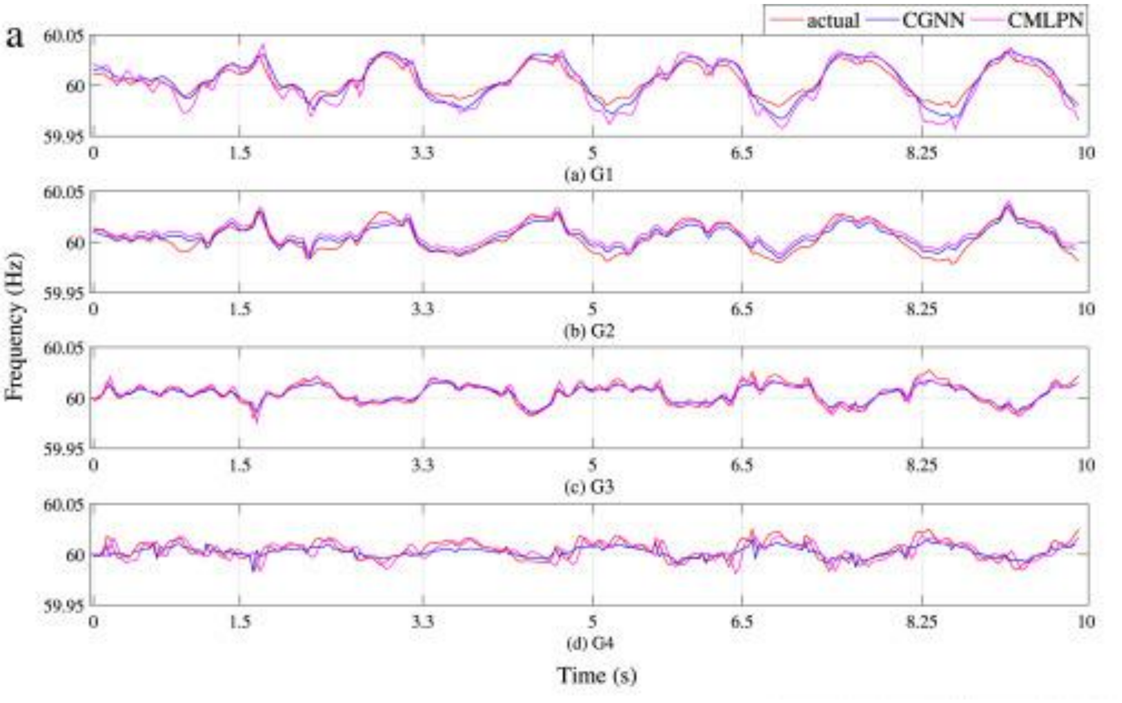

(a)

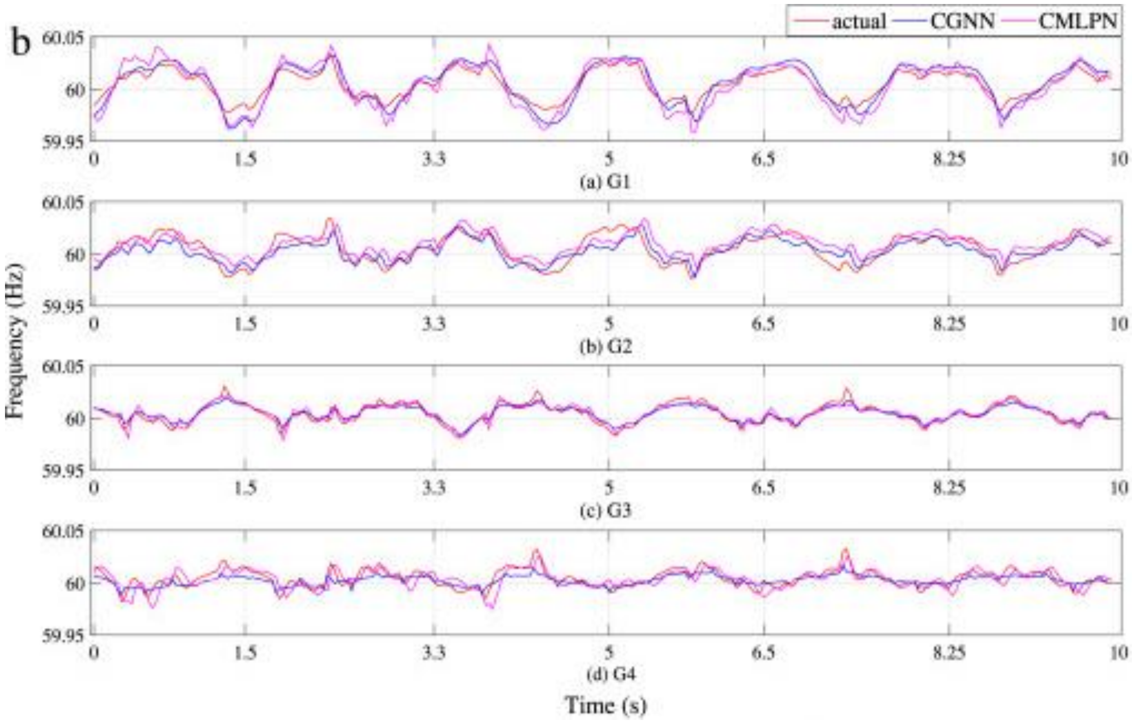

(b)

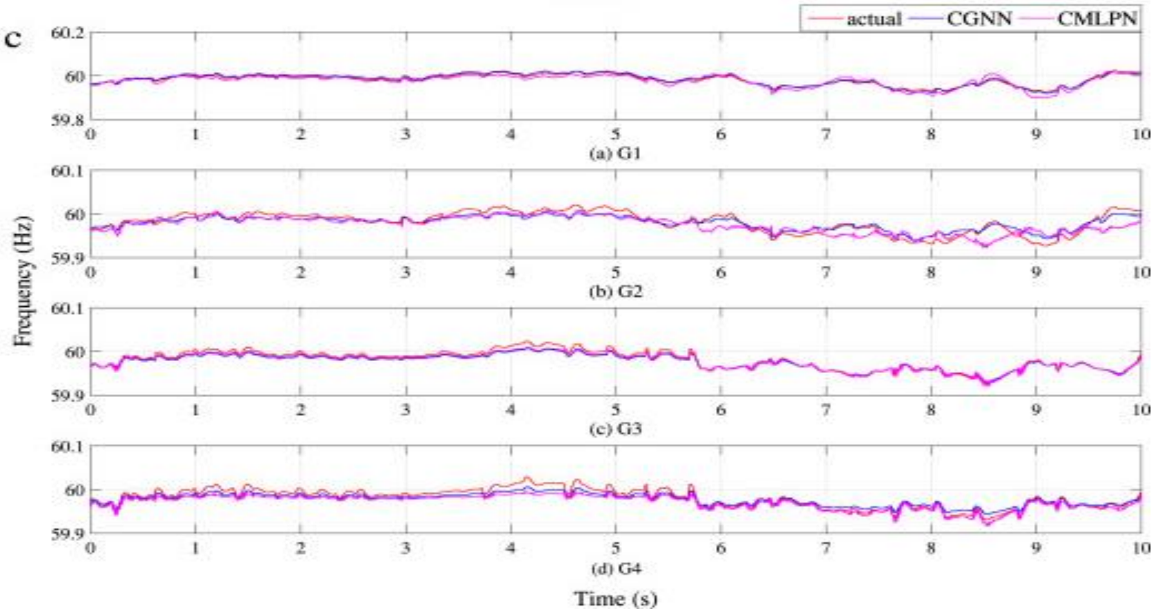

(c)

Figure 5.3 The CCGNN and CCMLPN combined 100 ms ahead frequency prediction with six inputs for four generators in (a) a 967 MW-1767MW operating condition; (b) a 900 MW-1500 MW operating condition; and (c) a 920 MW-1380 MW operating condition.

5.3 FSI for IEEE NE-NY Benchmark Model

The second test power system in this study is the IEEE New England-New York (NE-NY) power system shown in Figure 2.2. Here, each bus is assumed a cell with each cell connected with at least two nearest neighbors. For instance, the CCN based 200 *ms* ahead frequency prediction description for generator G1 with three neighbors and Bus 17 with four neighbors are expressed by (5.1) and (5.2).

$$\hat{f}_1\,(t{+}200) = f\{\, f_1(t), \Delta V_{ref-1}(t),\ f_1(t-200),\ f_1(t-400),\ \hat{f}_2(t),\ \hat{f}_8(t),\ \hat{f}_{10}(t)\} \qquad (5.1)$$

$$\hat{f}_{17}\,(t{+}200) = f\{ f_{17}(t), \Delta V_{ref-17}(t),\ f_{17}(t-200),\ f_{17}(t-400),\ \hat{f}_{15}(t),\ \hat{f}_{16}(t),\ \hat{f}_{18}(t),\ \hat{f}_{27}(t)\} \qquad (5.2)$$

Here, $\hat{f}_1(t{+}200)$ represents the (t+200) *ms* frequency prediction; $\Delta V_{ref\text{-}1}(t)$ the G1 reference voltage, $f_1(t\text{-}400)$ the past inputs of G1; $\hat{f}_2(t{+}200)$, $\hat{f}_{10}(t{+}200)$ and $\hat{f}_8(t{+}200)$ the G1 three closest neighbors predicted frequencies, and $\hat{f}_{15}(t)$, $\hat{f}_{16}(t)$, $\hat{f}_{18}(t{+}200)$, and $\hat{f}_{27}(t)$ representing all four neighbors of Cell 17.

Results in the previous section for a for widely adopted small-scale power system indicate the superiority of the FSI performance for CCGNN compared to CCMLPN. Here the subject of the study was the IEEE NE-NY system in which the frequency oscillation was generated by integrating PRBS signals in each generator’s voltage reference. Based on CCN’s framework description, cells can be a generator or bus in a system. In this test system, it was assumed that every bus was assigned as a cell to provide frequency predictions for all buses. The system corresponding CCN topology is presented in Figure 5.4.

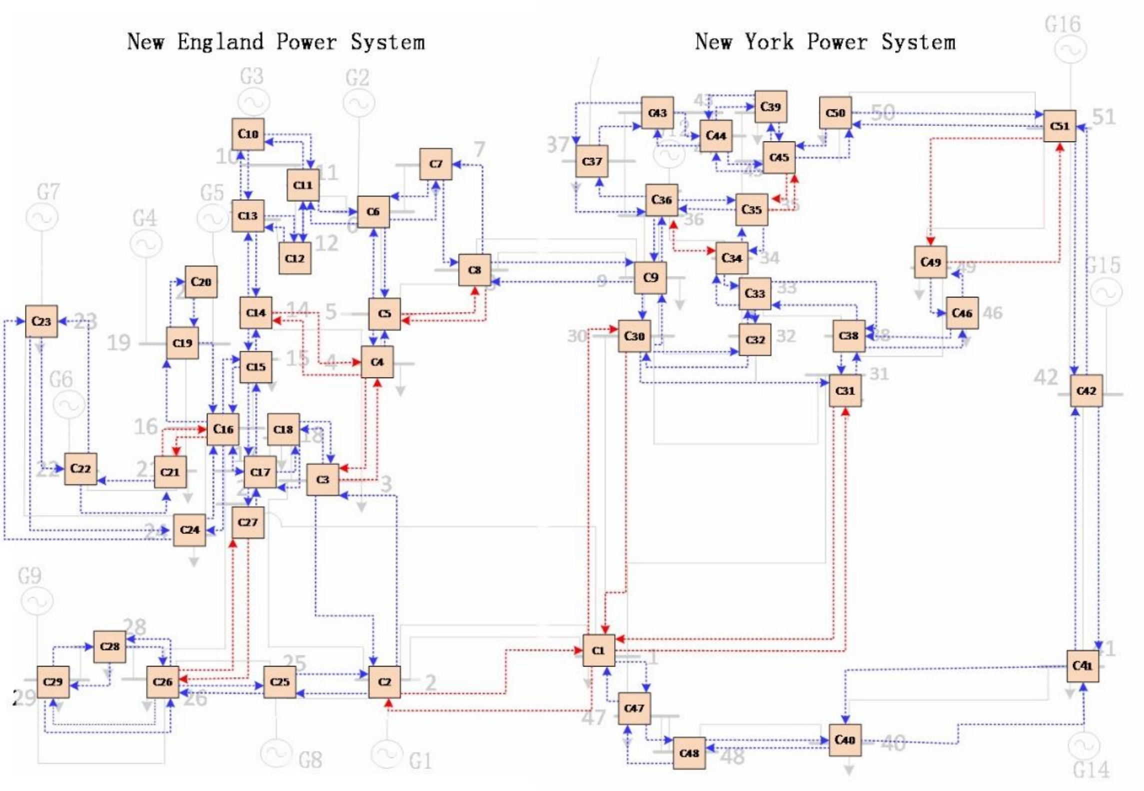

Figure 5.4 A CCN based frequency prediction diagram with multiple neighbors for the complete observation of the IEEE NE-NY power system.

The system buses can be categorized as the generator bus, load bus, and zero-injection bus. For simplicity, all three type buses are randomly selected for visualization: as Cells 2 and 22 for the generator bus, as Cells 17 and 27 for the zero injection bus and Cells 46 and 51 for the load bus. Accurately predicting the power usage for this medium scale NE-NY system, under severe conditions was a challenging enterprise. Therefore, two scenarios from the IEEE NE-NY power system were used in the CCN based FSI prediction test: a normal case (300 MW with PRBS) and a fault case (600 MW with a 5-cycle three-phase line to ground fault at Bus 27).

5.3.1 Case 1- Initial Testing for All Buses for Single-cycle Ahead Prediction

The first case study entailed a simulation under 300MW power exchange from NE to NY in which the learning measurements for the cells were in 3.34-second measurements captured by the PMUs. All 15.0-second PMU measurements were used for all bus predictions. The single-cycle ahead (i.e. 16.67 *ms*) frequency predictions for three bus types are shown in Figure 4.5 with the maximum frequency fluctuation of approximately 0.06 Hz.

An analysis of the frequency prediction of all cells determined that Cell 46 exhibit the largest MAPE value: at 8×10^{-3} %. Thus, Cell 46 (load bus) was selected for load bus fault validation with Cells 22 and 17 selected as the generator and zero-injection buses respectively, with both 4.7×10^{-3} % MAPEs due to the lowest prediction accuracy. A comparison of Cell 17 to Cell 22 reflected a more specific frequency behavior of generator G6.

5.3.2 Case 2- Multi-bus Types with Multi-timescale Predictions

As can be summarized from case 1, the Cells 46, 22 and 17 exhibited the worst prediction accuracy with PRBS perturbations. Thus, these three cells are selected for comparison in a fault condition with three timescales at time t: *t*+16.67 *ms*, *t*+100 *ms*, and *t*+200 *ms*. An 83.5 *ms* three-phase line to ground fault at Bus 27 under 600MW tie-line power transfer condition was used here, as shown in Figure 5.6. During the fault condition, the PRBS signals are set as zero injection for fault test. The fault is applied at 3.006 seconds and cleared at 3.0895 seconds. The CCN multi-timescale prediction is applied right after the fault being cleared.

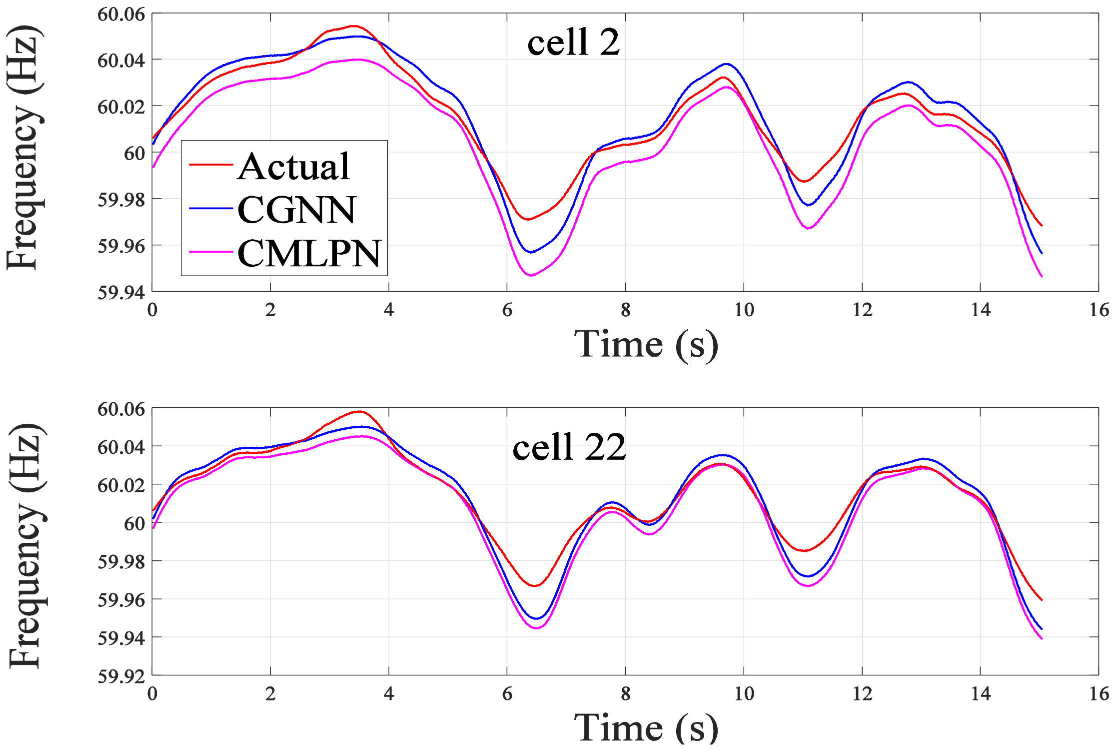
cell 2
Actual
CGNN
CMLPN
Frequency (Hz)
60.06
60.04
60.02
60
59.98
59.96
59.94
Time (s)
0
2
4
6
8
10
12
14
16
cell 22
Frequency (Hz)
60.06
60.04
60.02
60
59.98
59.96
59.94
59.92
Time (s)
0
2
4
6
8
10
12
14
16

(a)

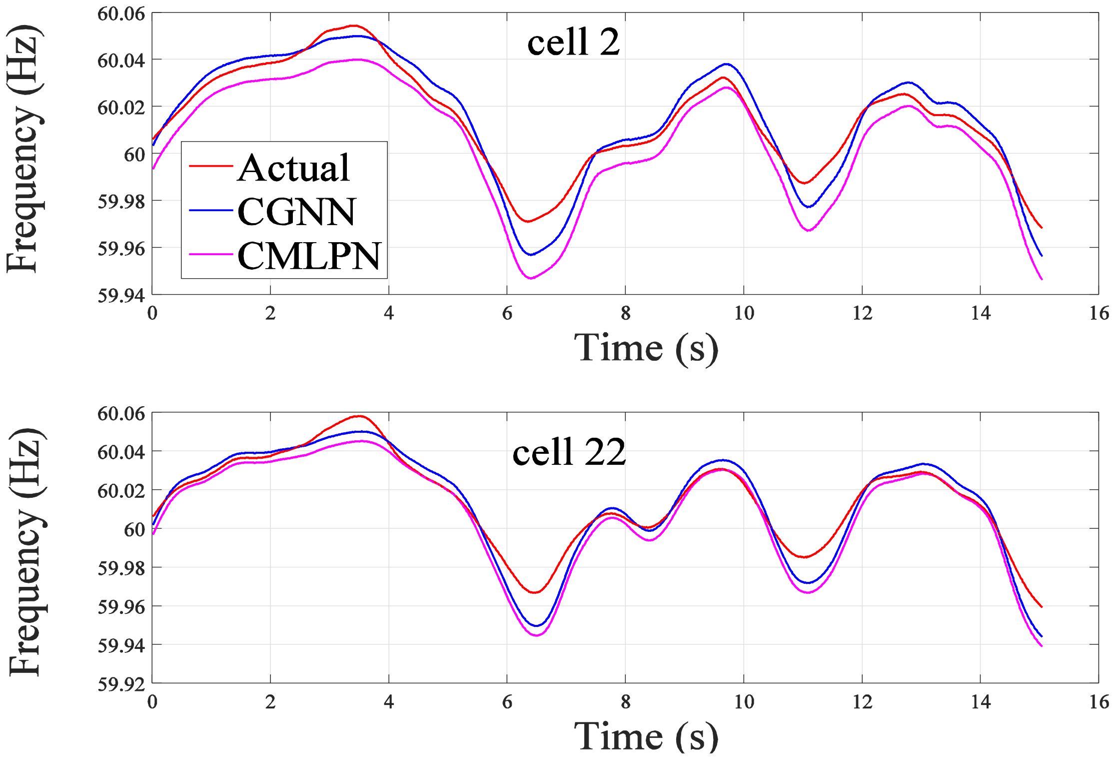
cell 2
Actual
CGNN
CMLPN
Frequency (Hz)
60.06
60.04
60.02
60
59.98
59.96
59.94
Time (s)
0
2
4
6
8
10
12
14
16
cell 22
Frequency (Hz)
60.06
60.04
60.02
60
59.98
59.96
59.94
59.92
Time (s)
0
2
4
6
8
10
12
14
16

(b)

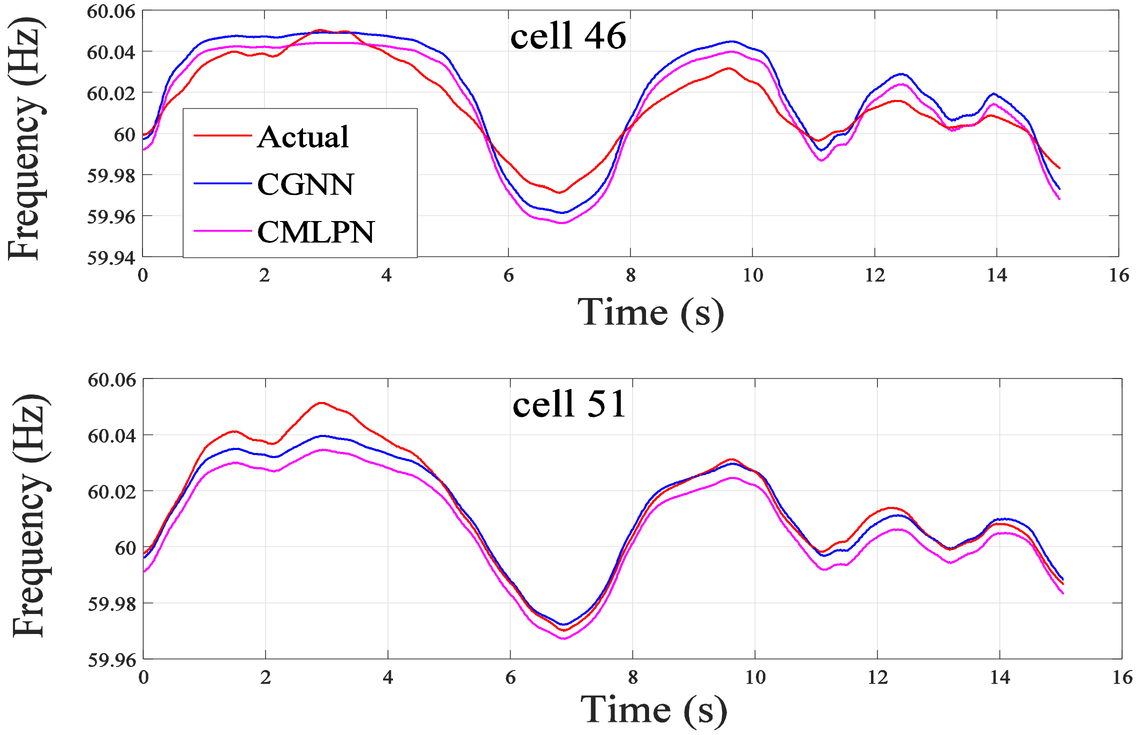

(c)

Figure 5.5 Three bus types frequency initial prediction in 16.67 ms ahead for an IEEE NE-NY system: (a) Generator bus type for the initial 300 MW power transfer; (b) Zero injection bus type for the initial 300 MW power; (c) Load bus type for the initial 300 MW power transfer.

The Bus 46 frequency predictions of this case are visualized and verified as shown in Figure 5.7 with the most inferior MAPE predictions as the 200 *ms* ahead being 0.147% (CCMLPN) and 0.134% (CCGNN). The frequency prediction profiles of generator Bus 22 are given in Figure 5.8. The 200 *ms* ahead of the MAPEs were 0.0834% (CCMLPN) and 0.0722% (CCGNN). The MAPEs for the zero-injection Bus 17 frequency predictions in multiple intervals are summarized in Table 5.2. Corresponding 16.67 *ms*, 100 *ms* and 200 *ms* frequency predictions for zero-injection Bus are shown in Figure. 5.9, along with the results of the 200 *ms* list of predictions with MAPEs of 0.156% (CCMLPN) and 0.144% (CCGNN). All three bus types' MAPE results are summarized in Table 5.2. The

Pm and CCGNN's normalized Pm value of three bus types are computed for comparison in Table 5.3. As can be indicated from the normalized Pm, the CCGNN had a superior performance within a range of 31 and 34 times for Bus 46 and 22 respectively in comparison to CCMLPN, whereas a 33 greater times superior for Bus 17 frequency predictions than CCMLPN.

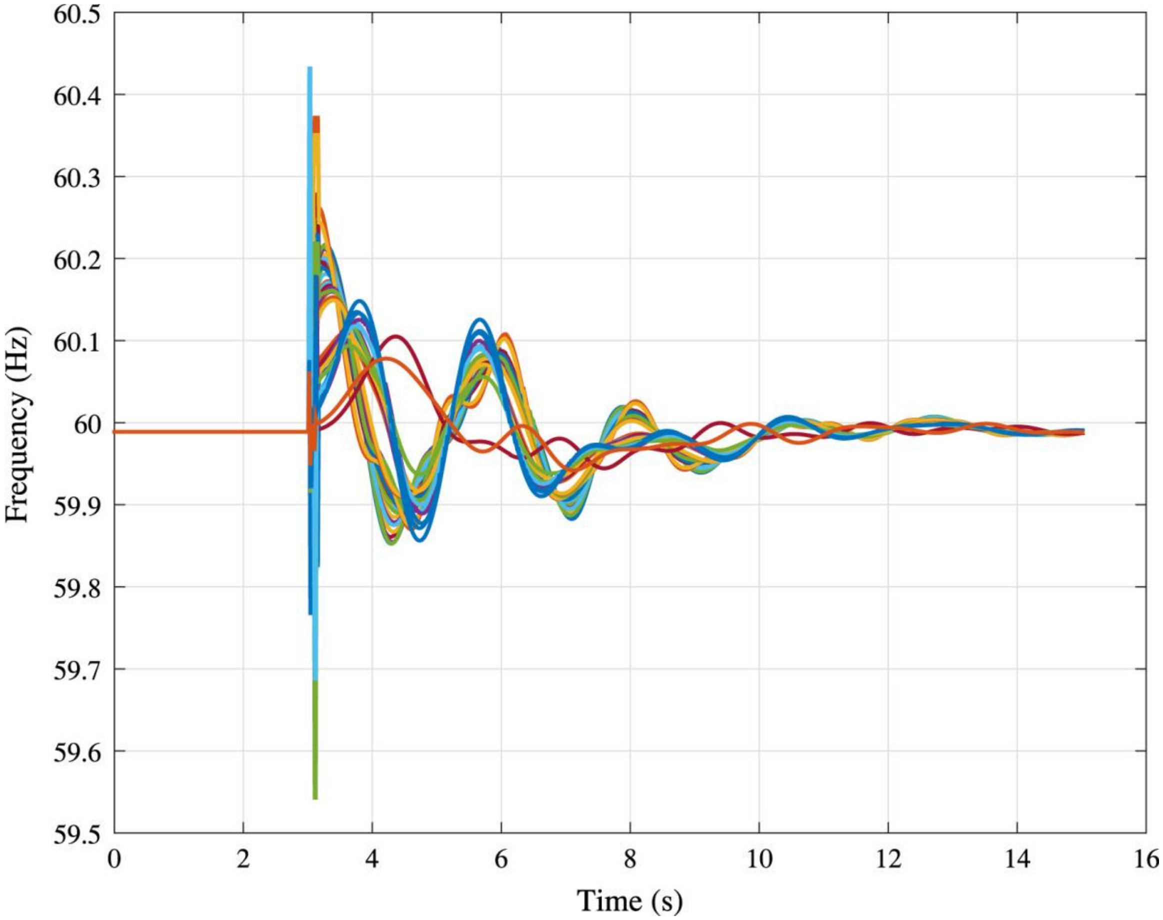

Figure 5.6 All frequency curves for a three-phase line to ground fault condition at Bus-27.

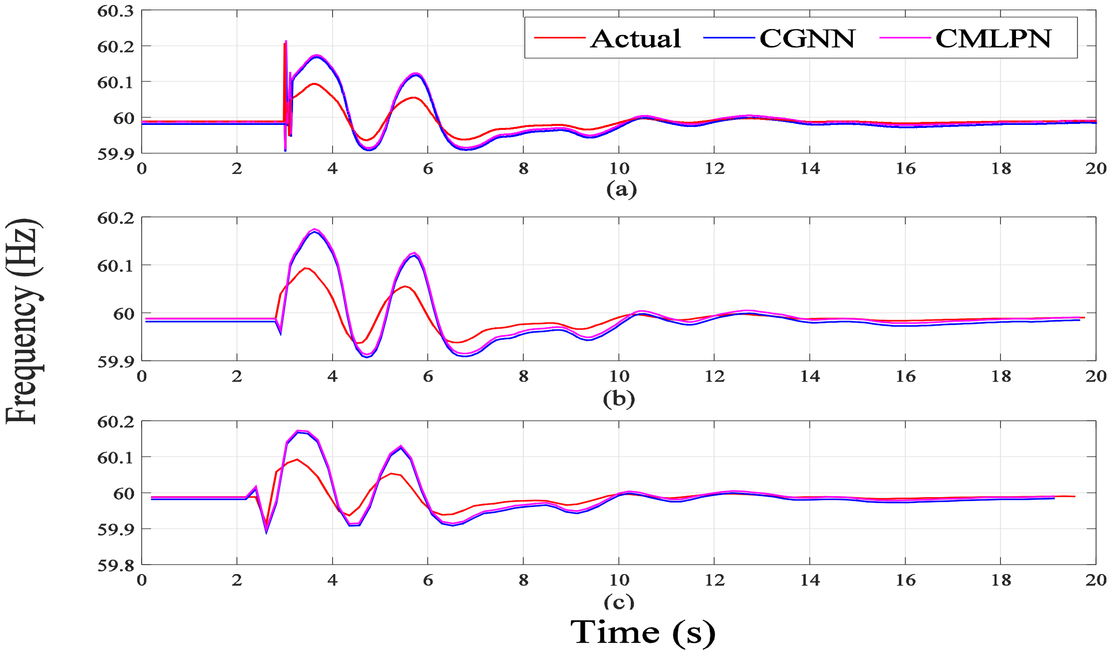

Figure 5.7 Bus 46 three timescale frequency predictions for fault condition: (a) refers Cell 46 16.67 *ms* ahead predictions; (b) refers to Cell 46 100 *ms* ahead predictions and (c) refers to Cell 46 200 *ms* ahead predictions.

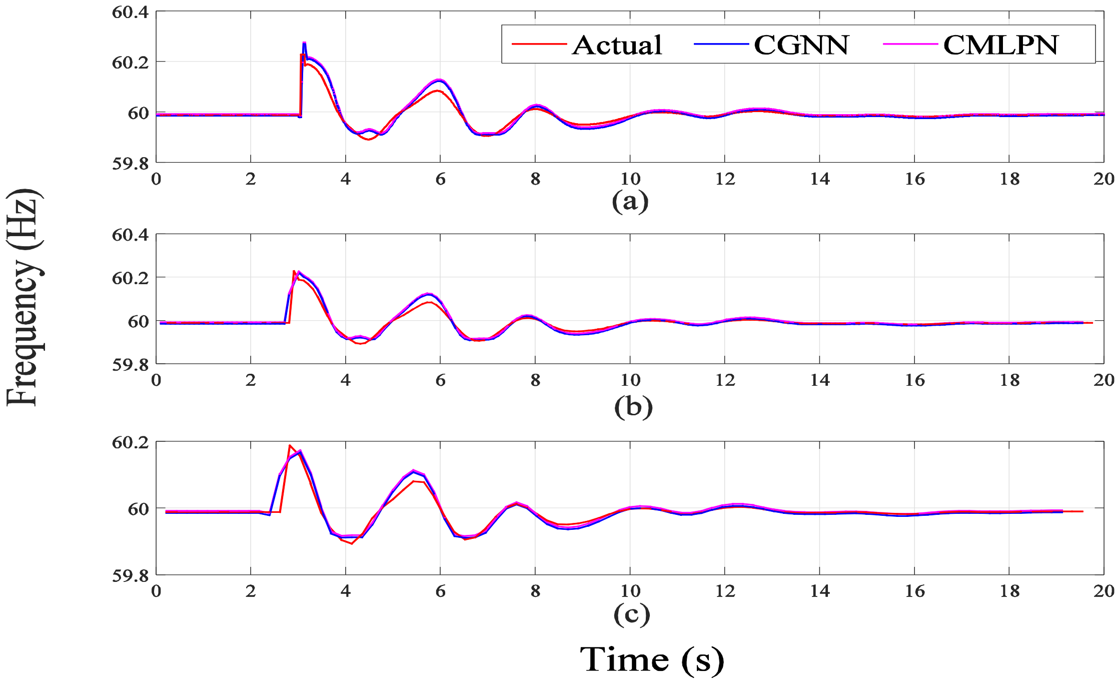

Figure 5.8 Bus 22 three timescale frequency predictions for fault condition: (a) refers to Cell 22 16.67 *ms* ahead prediction; (b) refers Cell 22 100 *ms* ahead prediction and (c) refers Cell 22 200 *ms* ahead prediction.

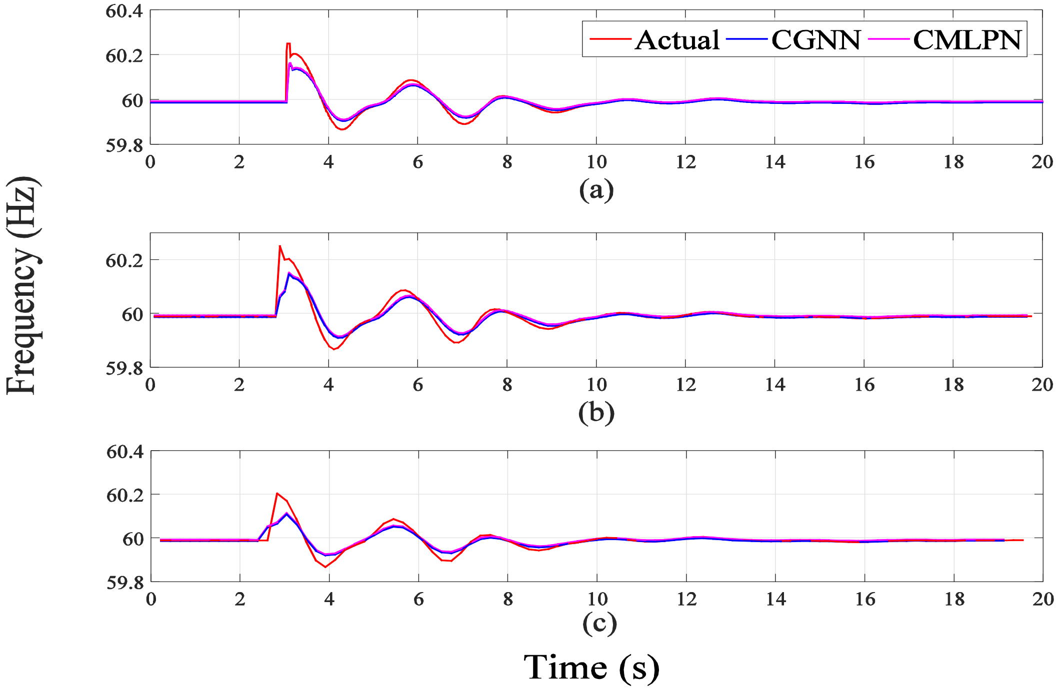

Figure 5.9 Bus 17 three timescale frequency predictions for fault conditions: (a) refers to Cell 17 16.67 *ms* ahead predictions; (b) refers to Cell 17 100 *ms* ahead predictions and (c) refers to Cell 17 200 *ms* ahead predictions.

5.4 Frequency Predictions with Actual Solar Parameters Integration

While multi-machine power systems with random perturbation were used in the CCN FSI prediction tests, in this FSI application study, as shown in Figure 2.1, here a renewable energy PV source was used for natural perturbation. Here, three PV power output average conditions were used in this analysis: high level (above 160MW on a sunny day), moderate level (between 0MW and 200MW on a moderate day), and low level (below 70 MW on a cloudy day). Sunny, moderate, and cloudy solar irradiance conditions at Clemson SC were used in the simulation, from 00:00:00 to 23:59:59 with 1 sec/sample rate. The combined sunny (August 19th, 2015), moderate (May 1st, 2015) and cloudy (November 18st, 2015) plots are shown in Figure 5.10. The sunny day data was used for reference and the moderate day data were used in the frequency prediction analysis. Cells represent all generators in this study.

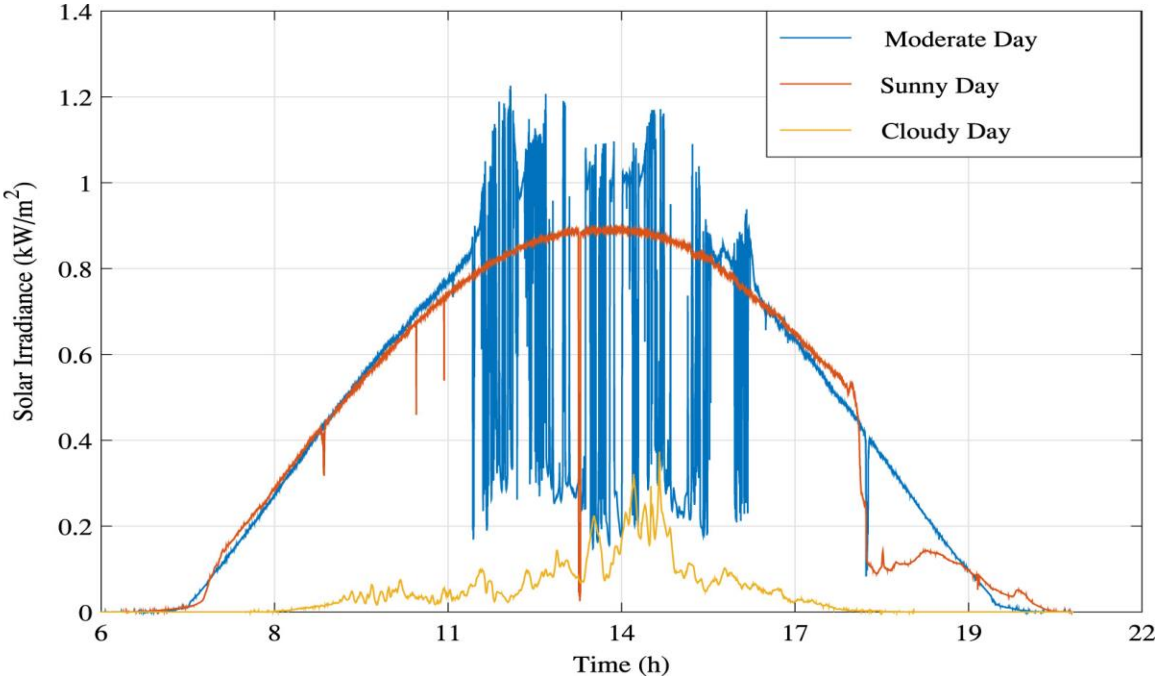

Figure 5.10 Solar irradiance variations during sunny, moderate and cloudy weather.

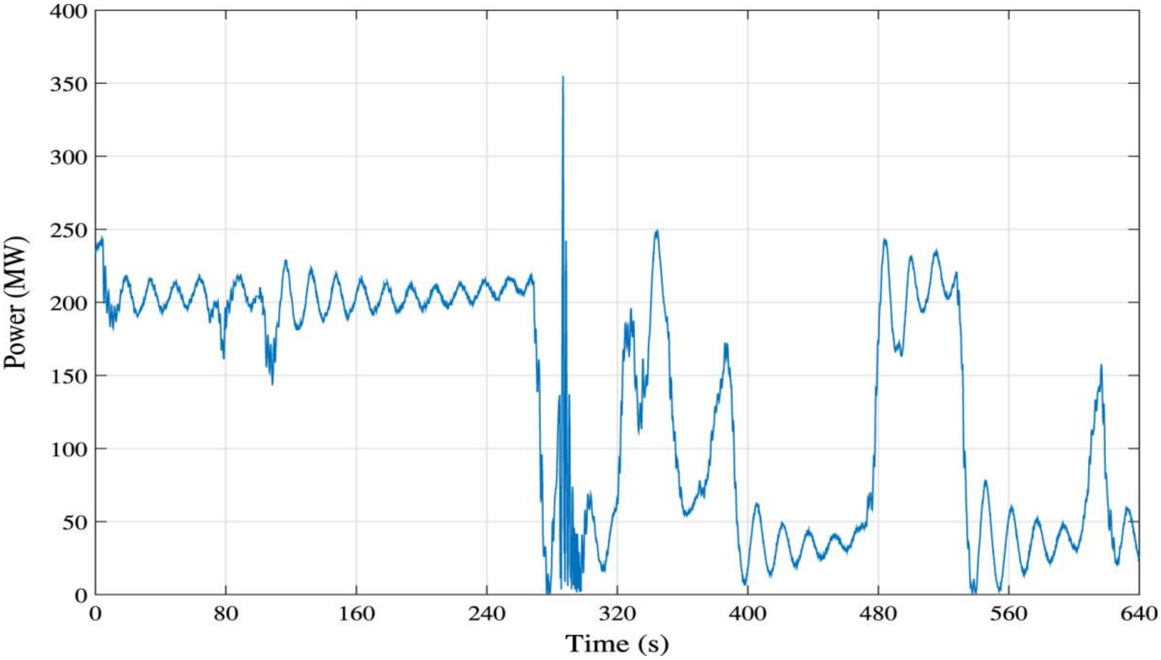

Figure 5.11 PV station power output for moderate day from 12:00:00 to 12:10:40 pm.

G2 was selected for following multi-timescale frequency prediction under a moderate weather condition. Since the solar irradiance challenges mildly, the prediction intervals were extended for a longer period. Three timescale predictions were performed at time t, namely *t*+16 *ms*, *t*+1000 *ms*, and *t*+2000 *ms*.

To better test, the FSI methodology, a randomly selected time-window from the moderate day was applied for testing, the period of which was 640 seconds for visual convenience, and flexible for prediction. The moderate PV system 640 seconds (from 12:00:00 pm to 12:10:40 pm) generation profile, shown in Figure 5.11, clearly indicates a corresponding power output ranges of 0-200 MW, respectively. The relevant multi-timescale frequency predictions of G2 are shown in Figure 5.12.

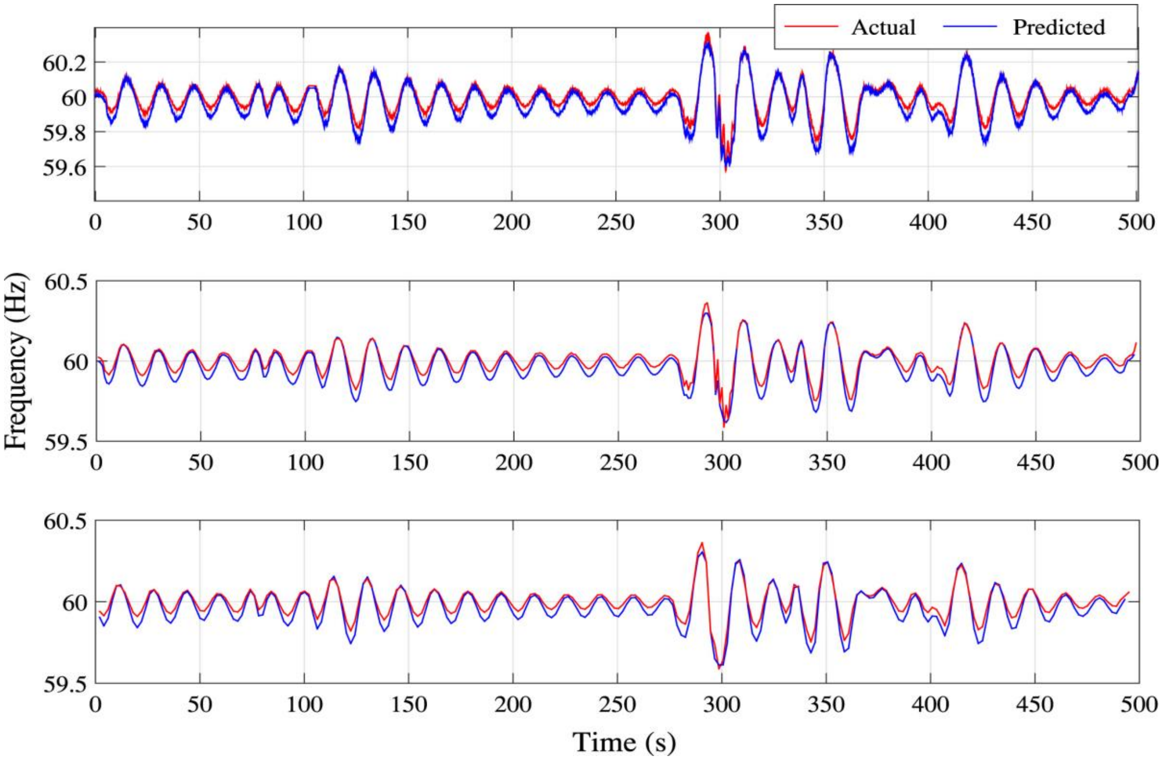

Figure 5.12 Multiple timescale frequency predictions for G2 under PV output condition during a moderate day: (a) refers G2 16.67 *ms* ahead predictions; (b) refers G2 1000 *ms* ahead predictions and (c) refers G2 2000 *ms* ahead predictions.

The overall comparison in Table 4.4 reveals that the CCN based algorithm can provide accurate frequency predictions up to 2000 *ms*. However, the accuracy value (both maximum APEs and MAPEs) declined with an increase in prediction intervals. The prediction accuracy was also dependent upon the fluctuation uncertainty level of the PV power output.

Table 5.1 Performance between CCGNN and CCMLPN for two-area system

Prediction Time Ahead	Model	P	Epochs	MAPE (%)	T (s)	P_m	Normalized P_m
33.3 ms	CCGNN	17×4	200	0.0044	334		15.23
33.3 ms	CCMLPN	56×4	200	0.0058	1184	6.5×10^{-4}	
100 ms	CCGNN	17×4	200	0.0083	336		18.05
100 ms	CCMLPN	56×4	200	0.0126	1213	2.9×10^{-4}	

Table 5.2 Multi-timescale frequency predictions MAPEs for IEEE NE-NY system three bus types (under 967MW-1767MW condition)

Time Ahead	MAPE for CCMLPN (%)				MAPE for CCGNN (%)			
	Bus 46	Bus 22	Bus 17	Average	Bus 46	Bus 22	Bus 17	Average
16.67 ms	0.12	0.0813	0.150	0.1171	0.13	0.0714	0.140	0.1138
100 ms	0.145	0.0815	0.152	0.1262	0.132	0.0716	0.143	0.1155
200 ms	0.147	0.0834	0.156	0.1288	0.134	0.0722	0.144	0.1167

Table 5.3 Multi-timescale frequency predictions performance metrics (P_m) for IEEE NE-NY system-three bus types

Time Ahead	Pm for CCMLPN								
	Parameters			T (s)			P_m		
	Bus 46	Bus 22	Bus 17	Bus 46	Bus 22	Bus 17	Bus 46	Bus 22	Bus 17
16.67 ms	56	56	72	9268			1.61×10^{-5}	2.37×10^{-5}	9.99×10^{-6}
100 ms							1.33×10^{-5}	2.36×10^{-5}	9.85×10^{-6}
200 ms							1.31×10^{-5}	2.36×10^{-5}	9.61×10^{-6}
Time Ahead	Pm for CCGNN								
	Parameters			T (s)			Normalized P_m		
	Bus 46	Bus 22	Bus 17	Bus 46	Bus 22	Bus 17	Bus 46	Bus 22	Bus 17
16.67 ms	17	17	21	1022			27.45	34.01	33.23
100 ms							32.78	34.07	33.09
200 ms							32.78	33.81	33.61

Table 5.4 Maximum frequency prediction performance metrics (Pm) for a two-area four-machine system with a PV source

t+ΔT ms ahead	Maximum APE	MAPE values		P_m for CCGNN		
	Moderate	Moderate	Average MAPE	Parameters	T (s)	P_m
16.67 ms	0.2298	0.0572	0.0302	17*4	337	$1.45*10^{-2}$
1000 ms	0.2615	0.0580	0.0306			$1.43*10^{-2}$
2000 ms	0.2909	0.0636	0.0334			$1.31*10^{-3}$

5.5 Summary

In this chapter, two soft-computing algorithms (CCGNN and CCMLPN), as being developed in chapter 3, had been implemented for the purposes of providing multi-timescale frequency predictions in power systems. The CCGNN framework based frequency situational intelligence approach has been compared with CCMLPN for three power system cases. The proposed FSI approach was used to successfully predict timescale frequencies within a range of 16.67 *ms* to 2 *s* under the following conditions: pseudo-random binary signal (PRBS), disturbance and PV random natural perturbation integrated. The results illustrate the effectiveness of the proposed frequency method in both CCMLPN and CCGNN for small (two-area four-machine), medium scale (IEEE NE-NY) power systems, and for a PV integrated power system. The results demonstrate that CCGNN has a superior performance for FSI, which is of importance for practical applications. In the following chapter, power system synchronous generators coherency analysis is introduced and incorporated with FSI methodology to analyze the high PV power penetrated test bed.

CHAPTER 6

SYNCHRONOUS GENERATORS ONLINE COHERENCY ANALYSIS WITH HIGH PV POWER INTEGRATION LEVELS

6.1 Overview

This chapter analyzes the online dynamic effects of utility-scale Photovoltaic (PV) plant integrated with a various power level for synchronous generator coherency grouping, in particular, the interconnected transmission grid. Furthermore, a generator vulnerability index (GVI) and corresponding power system vulnerability index (SVI) are proposed based on the dynamic coherency groups that are identified. These indices are to provide alerts to system operators of the variations of PV power and/or severe system disturbances on the coherency behavior. Typical results are provided for four disturbances including sudden PV power increase and decrease, unexpected bus faults on major tie-line (inter-area) transmission corridors. The results are elaborated based on the developed test bed with two utility-scale PV plants.

6.2 Synchronous Generator Coherency Analysis Methods Review

The purpose of power system coherency analysis involves identifying disturbances based on the similar behavior measured at the generator terminal. Previously, coherency analysis is required for power system islanding schedule or islanding control, system monitoring, and power system model reduction in offline mode as measurements are initially captured by supervisory control and data acquisition (SCADA) system in a minute-based sampling rate [72]. The subsequent and rapid deployment of PMUs means that millisecond-based high sampling rate PMU measurements provide the potential capability for enhancing control center situational awareness in real-time incorporating with utility-scale PVs in the multi-area power system. Therefore, online coherency analysis is necessary for system dynamic identification, wide-area based monitoring and control application.

Power system coherency analysis has been a subject of extensive and longstanding research. Model-based approaches were first developed to characterize synchronous generator inter-area oscillations for slow coherency analysis [72-73], which directly leads to the system islanding design and corresponding decomposition scheme schedule. However, the changes in generator model and power system topology during transients render these approaches negligible for use in a variation of power system operating conditions. Therefore, several coherency grouping methods have been proposed to provide an accurate and model-free result. Based on actual power system measurements, methods such as the Fast Fourier Transform [74], the Hilbert transform in empirical model decomposition [75], nonlinear Koopman modes [76], spectral clustering [77], and principal component analysis (PCA) [78] have been successfully used in coherency analysis. However, these offline methods provide holistic coherency groups for the entire period of disturbance, which deliver delayed and insufficient information for online operator decision-making.

The further evolution high sampling rate Phasor Measurement Units (PMUs) and the Wide-area Measurement System (WAMS) is accelerating the trend towards online and real-time data-driven coherent grouping [79-84]. Both on-line coherent clustering methods, i.e., the generator rotor angle and speed correlation coefficient index [79], and the projection pursuit (PP) [80] were developed based upon the WAMS network and PMU data. Meanwhile, real-time coherent analysis algorithms, such as the Independent Component Analysis (ICA) [81] graphic modeling [82], flock modeling [83] K-harmonic means clustering (KHMC) [31], dynamic coherency determination [84], were developed to provide fast response coherent techniques. However, all of these online and real-time coherency grouping methods concentrate on methodology demonstration for further control, which means they cannot narrow the operator's surfeit of information. This information oversupplied from a large amount of data captured by PMUs and widely interconnected power system is expected to be a significant problem. The objective of the online coherency methodology suitable for smart grid environment mitigates this problem by delivering only that information needed to assist the operator focus on the vulnerability parts of a system, thus decreasing extra interference and support the main-grid survive the transition to a higher PV penetration level at the utility-scale. Nevertheless, reducing the information flow requires further investigation.

6.3 Synchronous Generator Coherency Grouping

In this section, a *K*-harmonic means clustering (KHMC) approach is applied for online coherency analysis of synchronous generator. KHMC is a global optimizing algorithm that bases the adaptation of the group centers based on the entire groups/clusters that exist prior. Unlike ordinary *k*-means clustering, KHMC is insensitive to initialization of group centers and thus provides more accurate results. Besides, the updated group center of a current time step can also serve as the initialization for the next one; in this way, clustering results can be obtained at each consecutive time step, making KHMC very suitable for online clustering. In order to decide the number of clusters in KHMC, an Average Within-Group Distance (AWGD) threshold is adopted; groups may be merged or split to satisfy this threshold, the group number is thus decided indirectly.

6.3.1 Coherency Grouping Using KHMC

Denote x_i as a series of data for variable i and is composed of elements x_i (j) at each time interval j. Denote m_k as the group center k that has the same dimension as x_i. Then the harmonic distance between variable i and all the group centers can be presented as,

$$D_i = \sqrt{1 / \sum_{k=1}^{K} (1 / d_{ik}^{2})} \tag{6.1}$$

where d_{ik} is the distance between generator i and group center m_k, which can be defined by the L_2 norm of their difference, as in (6.2). Thus, a small value of harmonic mean signifies that the variable is well clustered to one specific group.

$$d_{ik} = \|x_i - m_k\|_2 \overset{\Delta}{=} \sqrt{\sum_j (x_i(j) - m_k(j))^2} \tag{6.2}$$

According to the aforementioned harmonic distance concept for clustering, this multi-generator coherent grouping can be transferred into an optimization problem, with the objective of minimizing the sum of harmonic mean through all the generators. This minimization ensures that all of the generators are clustered to the correct groups respectively. Thus, the objective function is defined as (6.3), where the *H* represents the generator *i* inertia.

$$\min J = \sum_i H_i D_i^2 \tag{6.3}$$

Thus, each group center m_k can be obtained by analytically solving (6.3) ~ (6.5) and $\partial J/\partial m_k = 0$, a solution that is expressed as follows:

$$m_k^{new} = \sum_{i=1}^{N} \frac{H_i D_i^4 x_i}{d_{ik}^3} / \sum_{i=1}^{N} \frac{H_i D_i^4}{d_{ik}^3} \tag{6.4}$$

$$\| m_k^{t+1} - m_k^t \|_2 < C_{threshold} \tag{6.5}$$

It can be seen from (6.4) that the value of d_{ik} is needed for the update of group center m_k. Conversely, it can be seen from (6.2) that the value of m_k is needed for the update of d_{ik}. Thus, (6.2) and (6.4) are used iteratively and repetitively until convergence is achieved at (6.5). The $C_{threshold}$ is set to 0.01 in this study. In the practical generator speed cluster, their values are normally close to 377 rad/s, in which, on the other hand, only needs less than ten iterations for convergence satisfaction. The application of the KHMC method thus clusters the generators into the closest group center, based on the measured generator speed data by PMUs.

6.3.2 Coherency Visualization on Multiple Data Windows

After obtaining the coherent groups, especially the significant group pattern changes, this valuable information is transferred into a direct situational configuration and provided to grid operators who must make quick decisions or may need it to verify the system status. Thus, the coherent group visualization is represented by substantially different regions of color, updated in accordance with the output of the KHMC algorithm. These differences in the amount of the generators in the system, in turn, result in a variance in the number of regions according to the coherent groups.

Initially, the sliding data window is set as 2 seconds length with 100 ms updating rate, which provides the instant monitoring of the system abnormal behavior in a perspective of coherency groups. Later, the sliding data window is expended into multiple time intervals (2s, 5s, 10s, 30s, and 60s) thereby providing short term to long term information of the power system after disturbances. The multiple data windows accommodate the operators' demand for both detailed and holistic view of the generator behavior with disturbances. Note the multiple data window results will present step by step only after the data processing and coherency analyzing are finished, thereby, the operator will be consecutively informed for system changes from quasi-real-time up to 1-minute post-disturbance results.

6.3.3 Coherency Analysis for Jaccard Similarity Index

Although this continuous update of the color regions mainly reflects the changes of generator groups to itself, a comparison between the new settled generator groups and the baseline is also crucial for anticipating any systematic alteration in the generators. Similar measures were then used to determine the coefficient of the similarity of the PV integrated groups and the reference case sets. It is well recognized that there are quite a few methods to calculate the similarity in this circumstance. Yet, the design of direct comparison of coherent groups between the reference and the changed groups has rarely been explored up to now, which provides the operator the immediately actionable information without digesting. Therefore, the Jaccard index [85] or the Jaccard similarity (JS) coefficient is then used to implement this similarity metric. The Jaccard similarity is a statistic index calculated for purposes of comparing the similarity of different sample sets. It is mathematically defined as the amount of the intersection set over the amount of the union of sample sets. This fundamental equation is expressed as follows:

$$\mathrm{JS}(\mathbf{A},\mathbf{B}) = \frac{|\mathbf{A} \cap \mathbf{B}|}{|\mathbf{A} \cup \mathbf{B}|} \tag{6.6}$$

where ***A*** and ***B*** are the group sets, with |***A***| and |***B***| denoting the cardinality of groupsets, which represent the elements in the corresponding sets. The intersection between two group sets is denoted as |***A***∩***B***| with the union between these two sets denoted as |***A***∪***B***|. The JS value lies between 0 and 1. For same sets ***A*** and ***B***, however, the JS value is equal to 1, and the value drops to 0. In the coherent group situation, the set ***B*** consists of *n* subsets, which contains the clustered generator index in PV entailed case while the set ***A*** refers to the *n* subsets of the corresponding base case. Thus, the JS value of 1 stands for the *n* identical sets between ***A*** and ***B*,** while 0 denotes that no generators are clustered in s similar fashion. A higher JS value represents a higher similarity consequence.

6.3.4 Generator and Power System Vulnerability Identification

The coherency analysis and similarity index can directly lead to a valuable application -- determining the critical or vulnerable generator in the system directly to provide early warning or emergency calls. To reach this goal, a generator vulnerability index (GVI) is proposed as follows:

$$GVI(Gi) = \frac{n(Gi)}{N}$$

$$N = \frac{T_{window}}{f_{coherent}} \tag{6.7}$$

where N refers to the observation time window in seconds and $f_{coherent}$ is the coherent grouping updating rate; $n(G_i)$ stands for those instances wherein the generator G_i changes its coherent groups in the observation time window N. As can be derivate from (6.7), the *GVI* is within a range of [0,1]. For a steady-state situation, the n is far less than the N as the *GVI* denotes to 0. On the contrary, for a PV perturbated disturbance, the n is close to the N as *GVI* tends to 1. Thereby, the *GVI* uses 1 representing the critical vulnerability and 0 representing the non-vulnerability.

Further, the power system vulnerability index (SVI) considering both vulnerability generator index (GVI) and corresponding generator inertia (H_{Gi}) is then proposed as in (6.8).

$$SVI(Gi) = \frac{H_{Gi} \times GVI(Gi)}{\sum \{H_{Gi} \times GVI(Gi)\}} \tag{6.8}$$

Similarly to (6.7) of *GVI*, the *SVI* is also within a range of [0,1] with 1 representing the critical vulnerability and 0 representing the non-vulnerability.

For instance, assume that a six-generator system base case set ***A*** contains the following three coherent groups of three subsets: {G1, G2, G3}, {G4, G5}, and {G6}. A disturbance is then applied to this six-generator system. Further, assume that set ***B*** represents a post-disturbance result of the coherent grouping, which contains four groups of four subsets: {G1, G2}, {G3, G5}, {G4}, and {G6}. Based on the aforementioned

Jaccard similarity method, the intersection of set ***A*** and ***B*** represents but a single group, {G6}, which is 1. The union of both two sets is 6 with both sets containing three different subsets. In the end, the JS (A, B) = 1/6= 0.167. Specifically, the assumption is during a certain period of time (60 s with a 100 ms updating rate, inertia H=20) that the G4 changes its coherent groups 200 times. Thus, the *GVI*(G4) =200/600=0.33. After figuring out the independent GVI for each generator, the SVI can then be processed based on (6.8).

In this research, three data visualization methods are proposed as the coherency group color regions, the JS index, and the GVI/SVI, respectively. Overall, they aim for providing intuitive representation to operators, empowering faster situational awareness of system severe disturbances while utility-scale PV power involves. Specifically, they concentrate on different aspects: the coherency color groups together with the JS index represent for system immediate response; the GVI and SVI deliver the refined vulnerability-based metrics that reduces cognitive demands on operators.

A general coherent grouping and system vulnerability identifying procedure are presented in Figure 6.1. At every sampling moment, a data window of 2 s is updated by sliding the observing window one sample forward. Since only one data point of 100 ms interval is changed at each moment, the grouping and identifying algorithm thus iterates to correct the new group centers by taking the previous-step group centers as the initialization.

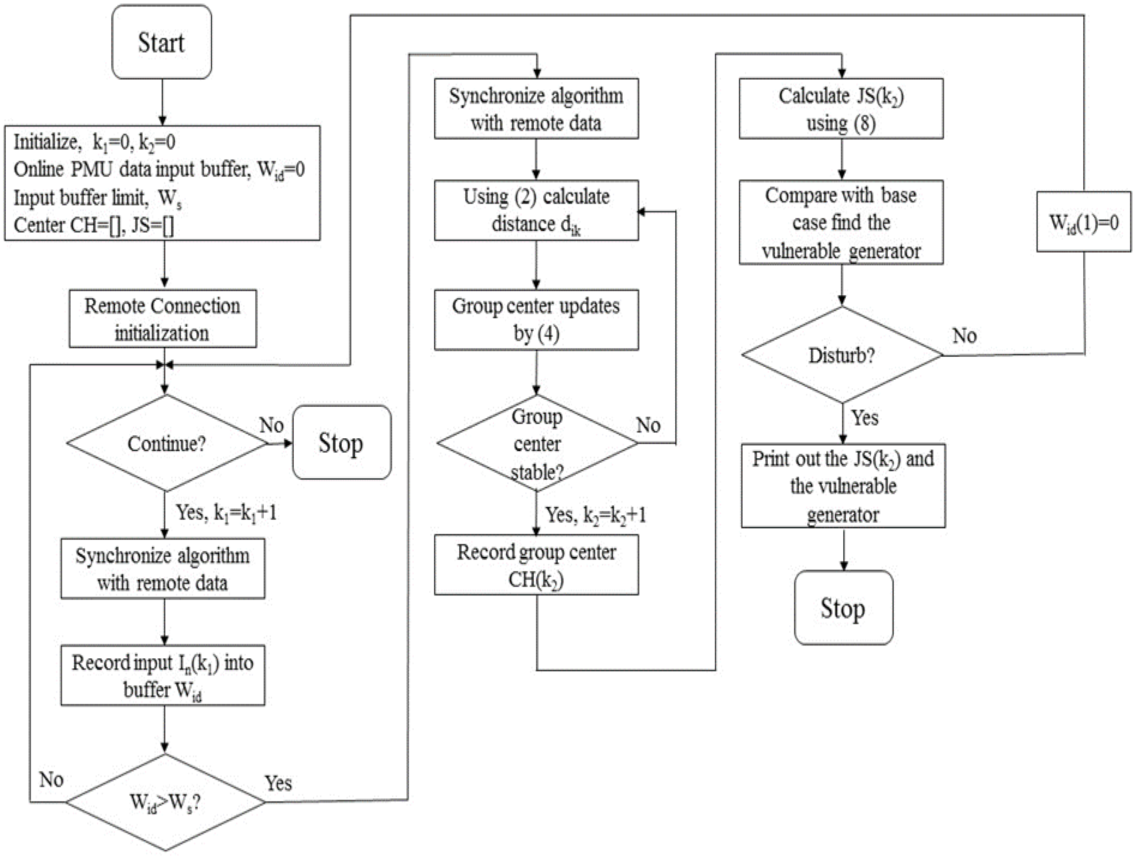

Figure 6.1 The general flowchart of the on-line coherent grouping using KHMC.

6.4 Results and Case Studies

In this section, the proposed online coherency grouping method is firstly visualized in single sampling data window using the aforementioned KHMC method, for purposes of elucidating the aftermath of the utility-scale PV penetration in multi-area power systems. An example of a generator coherency grouping is presented in Figure 6.2. Moreover, the GVI and SVI for operation application are calculated, presented, and explained in a synthetic dynamic PV penetration environment for multi-timescale data windows (2s, 5s, 10s, 30s, and 60s). Here, custom-tailored simulations are carried out for the inter-area disturbances that occur at different inter-connected buses.

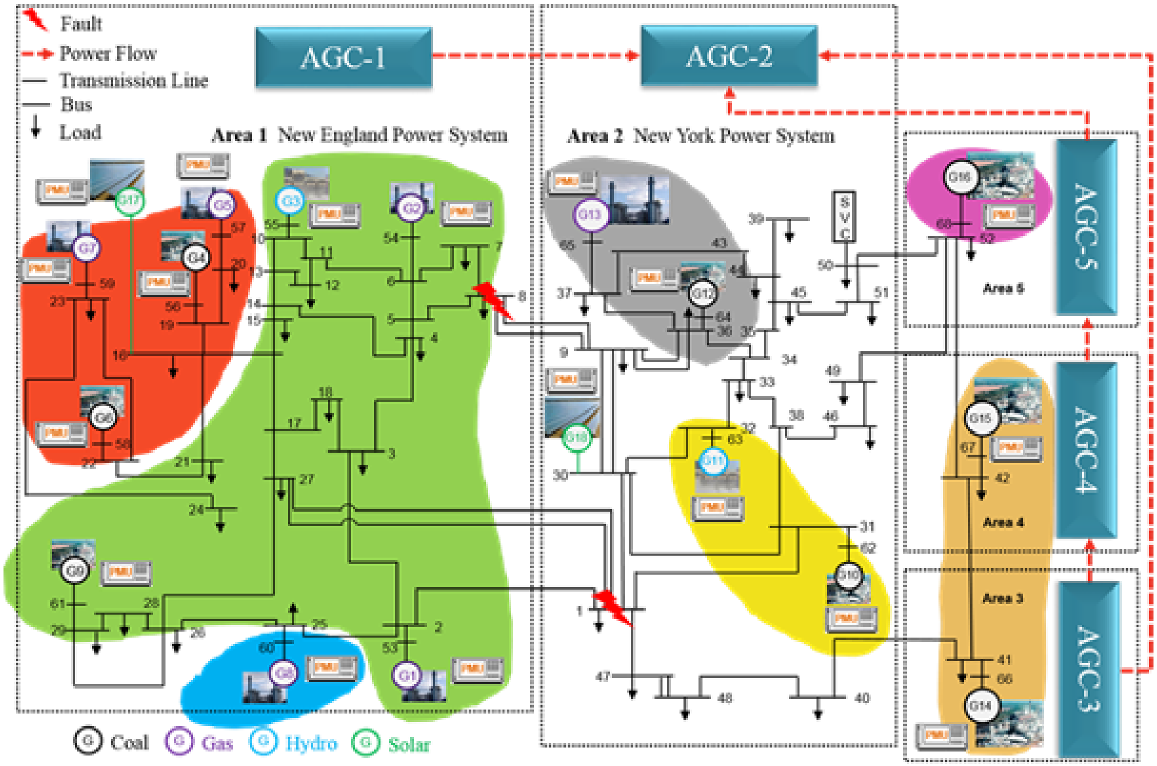

Figure 6.2 The real-time test bed system with utility-scale PV stations integrated. Coherent grouping result is presented as seven colored regions for steady state with peak PV power integration.

6.4.1 Fault Perturbed Coherency Grouping with Single PV Plant Penetration

As the PV replaces a significant amount of generation capacity with no inertia supplement, the occurrence of a fault results in its characterization by higher inter-area swings. In order to observe such oscillations, the 6-cycle and 10-cycle fault duration times are adopted as three-phase faults. The 10-cycle fault time is considered the premiere scenario as it generates the severest disturbance in this study. To closely observe the generator inter-area and intra-area oscillations in Area-1 and Area-2, tie-line Bus 1 and Bus 8 are chosen to apply the fault. In order to examine the utility-scale PV effects in coherency grouping, a step-by-step PV power penetration increase has been conducted for the following studies. A comparison of onsite generation values with zero and maximum PV penetration is presented in Table 6.1.

Case 1- Three-phase faults incorporate with PV in a single area

In this case study, the PV plants were deployed separately in each area for testing. A three-phase line-to-ground fault was applied separately at Bus 8 (Area 1) or Bus 1 (Area 2) to cause an inter-area disturbance. The coherency grouping results are shown in Figures 6.3-6.4 for Bus 8 fault and Figures 6.5-6.6 for Bus 1 fault with respect to the different PV penetration levels. As can be seen in Figures 6.3 (Bus 8 fault) and 6.5 (Bus 1 fault), the fault was applied at (*t*+2) s and the entire colored coherent groups disintegrated during the first 2 seconds, which indicated severe generator speed oscillations across the entire system. Although the speed oscillations decayed after 6 seconds, the system coherent groups as observed from the color map showed the active group exchanges for another 3 seconds. The comparisons of coherency grouping updates in terms of time are summarized in Tables 6.2 and 6.3.

Regarding the studies in Area 1 and Area 2, the coherency analysis presented a detrimental impact with respect to the increased PV power, specifically in terms of larger oscillation magnitudes for the second swing, from (*t*+4) s to (*t*+10) s that indicated a longer settling period, which was less similar to the reference cases. The coherency grouping pattern was also altered with an integration of 500 MW or more PV power. The similarity index was listed in Table 6.4 for all 16 generators shown in Figures 6.3-6.6. The Jaccard indices indicate that the system experienced a worse scenario when a fault time of 10-cycles was applied, as opposed to the 6-cycles. The results also indicate that the fault applied at Bus 1 led to a worse situation than the fault applied at Bus 8, whereas the PV at Area 2 was observed performing a passive role compared to the PV at Area 1

Table 6. 1 Onsite generation in a steady-state condition with zero and maximum PV

Generator	**Active Power with Zero PV (MW)**	**Active Power with Max PV (MW)**	**Generator**	**Active Power with Zero PV (MW)**	**Active Power with Max PV (MW)**
G1	250	247	G9	797	744
G2	546	486	G10	624	526
G3	602	498	G11	1422	1313
G4	652	609	G12	1634	1455
G5	506	453	G13	3032	2828
G6	697	644	G14	5834	5727
G7	558	506	G15	6083	5989
G8	648	549	G16	5475	5390
G17 (PV)	0	750			
G18 (PV)	0	700			
Total	29360 (Zero PV)		Total	27964 (Max PV)	

Table 6. 2 Case 1 - coherent groups with Area-1 maximum PV under Bus 1 and Bus 8 faults over a ten-cycle duration

Group Index	**at 2.5 s (Bus 1)**	**at 2.5 s (Bus 8)**	**at 5 s (Bus 1)**	**at 5 s (Bus 8)**	**at 10 s (Bus 1)**	**at 10 s (Bus 8)**
1	G4, G7, G9	G2, G3, G4, G7	G4, G5, G6, G7, G9	G4, G5, G6, G7, G9	G4, G5, G6, G7, G9	G4, G5, G6, G7
2	G1, G5, G6	G1, G5, G6, G9	G8	G1, G8	G2, G3	G2, G3,
3	G2, G3	G8	G1, G2, G3	G2, G3	G1	G8
4	G10	G11	G11	G10	G8	G1, G9
5	G8, G11	G10	G14, G15, G16	G14, G15, G16	G10, G11, G14	G10, G11
6	G12, G13	G12, G13	G10	G11	G15, G16	G12, G13
7	G14, G15, G16	G14, G15, G16	G12, G13	G12, G13	G12, G13	G14, G15,G16

Table 6. 3 Case 1 - coherent groups with Area-2 maximum PV under Bus 1 and Bus 8 faults over a ten-cycle duration

Group Index	at 2.5 s (Bus 1)	at 2.5 s (Bus 8)	at 5 s (Bus 1)	at 5 s (Bus 8)	at 10 s (Bus 1)	at 10 s (Bus 8)
1	G4 G7 G9	G1 G5 G6 G9	G4 G5 G6 G7 G9	G4 G5 G6 G7 G9	G1, G4, G5, G6, G7, G8	G4 G5 G6 G7
2	G1 G5 G6	G2 G3	G3 G8	G1 G8	G2, G3	G2 G3 G14
3	G2 G3	G4 G7 G8	G2	G2 G3	G9	G1 G8
4	G8	G11	G1 G11	G14 G15 G16	G10	G10 G15
5	G10	G10	G14 G15 G16	G11	G11	G11
6	G11	G12 G13	G10	G10	G12, G13	G9 G16
7	G12 G13 G14 G15 G16	G14 G15 G16	G12 G13	G12 G13	G14, G15, G16	G12 G13

Table 6. 4 the Jaccard similarity results for the case-1 static PV penetration studies

Cases	0 MW	50 MW	250 MW	500 MW	700 MW	750 MW
Area-1 PV with B1 6-cycle fault	1	0.7766	0.7666	0.7221	0.7167	0.7026
Area-1 PV with B8 6-cycle fault	1	0.8329	0.7871	0.7636	0.7433	0.7372
Area-2 PV with B1 6-cycle fault	1	0.9319	0.8825	0.8305	0.8036	N/A
Area-2 PV with B8 6-cycle fault	1	0.9122	0.8738	0.8303	0.8062	N/A
Area-1 PV with B1 10-cycle fault	1	0.7258	0.7598	0.7110	0.7273	0.7196
Area-1 PV with B8 10-cycle fault	1	0.7998	0.7918	0.7003	0.6747	0.6534
Area-2 PV with B1 10-cycle fault	1	0.8115	0.7527	0.8239	0.7480	N/A
Area-2 PV with B8 10-cycle fault	1	0.9103	0.8242	0.8200	0.8040	N/A

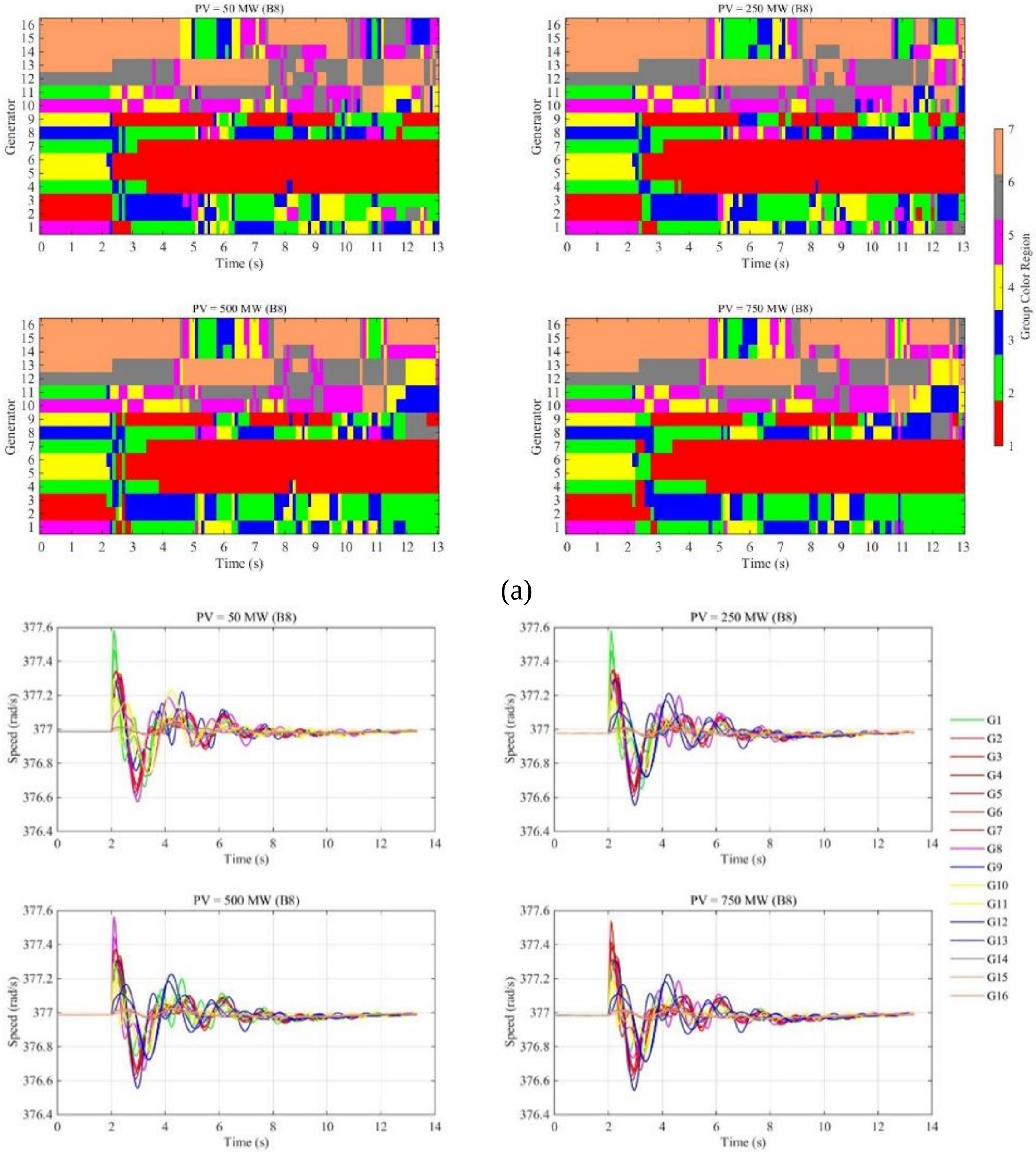

(a)

(b)

Figure 6. 3 (a) The PV penetration levels of all four coherent groups of the Area-1 Bus 8 three-phase fault a ten-cycle duration; (b) All generator responses for the corresponding PV penetration levels under the same fault conditions.

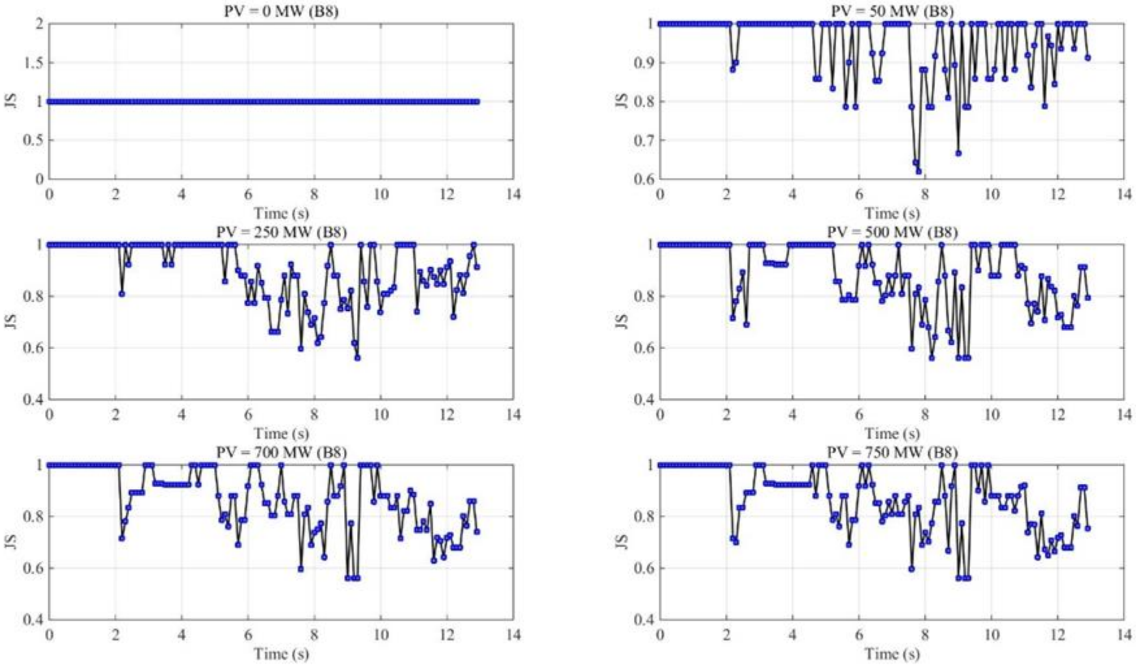

Figure 6. 4 The Jaccard similarity results for all PV penetration levels under same fault conditions.

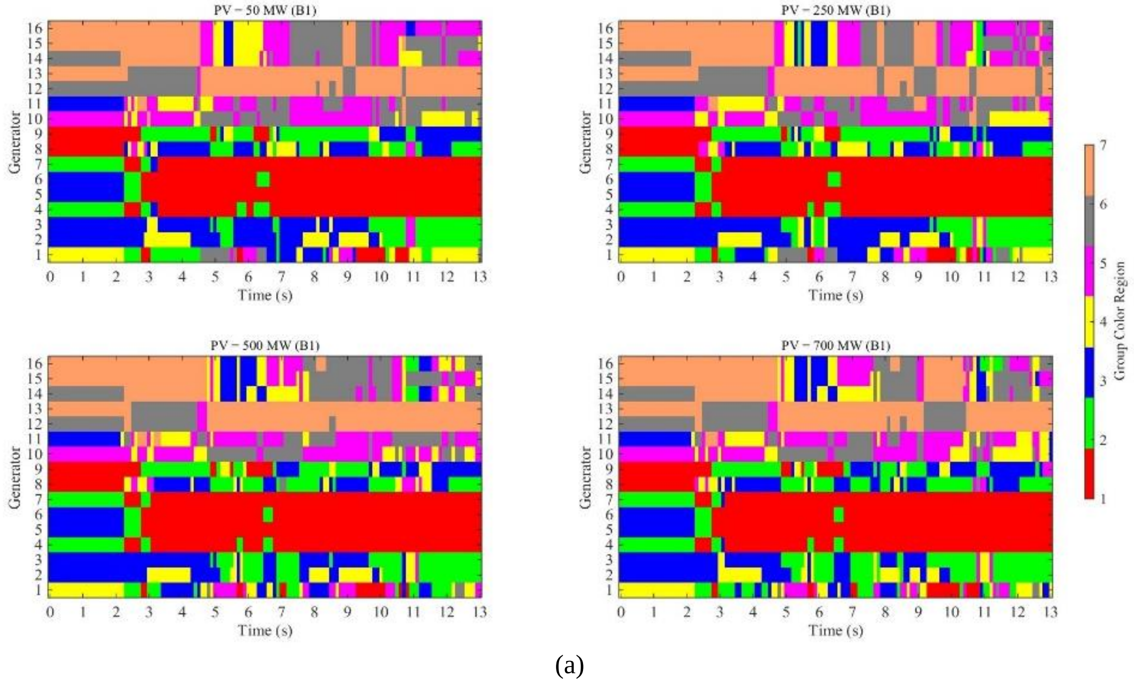

(a)

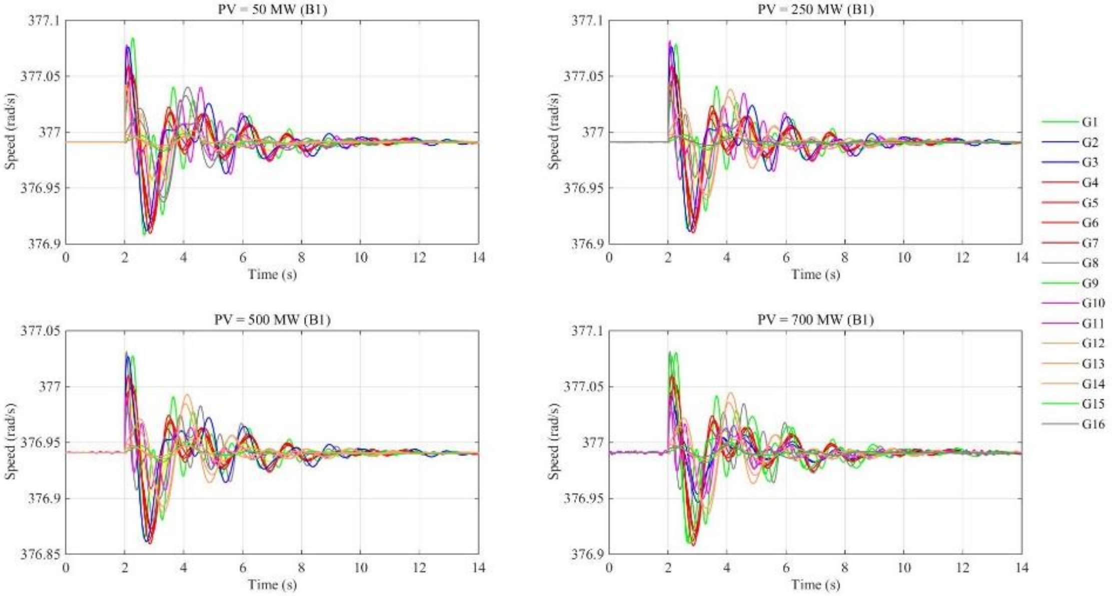

(b)

Figure 6. 5. (a) The PV penetration levels of all four coherent groups of Area-2 Bus 1 three-phase fault with a ten-cycle duration; (b) All generator responses for the corresponding PV penetration levels under same fault conditions.

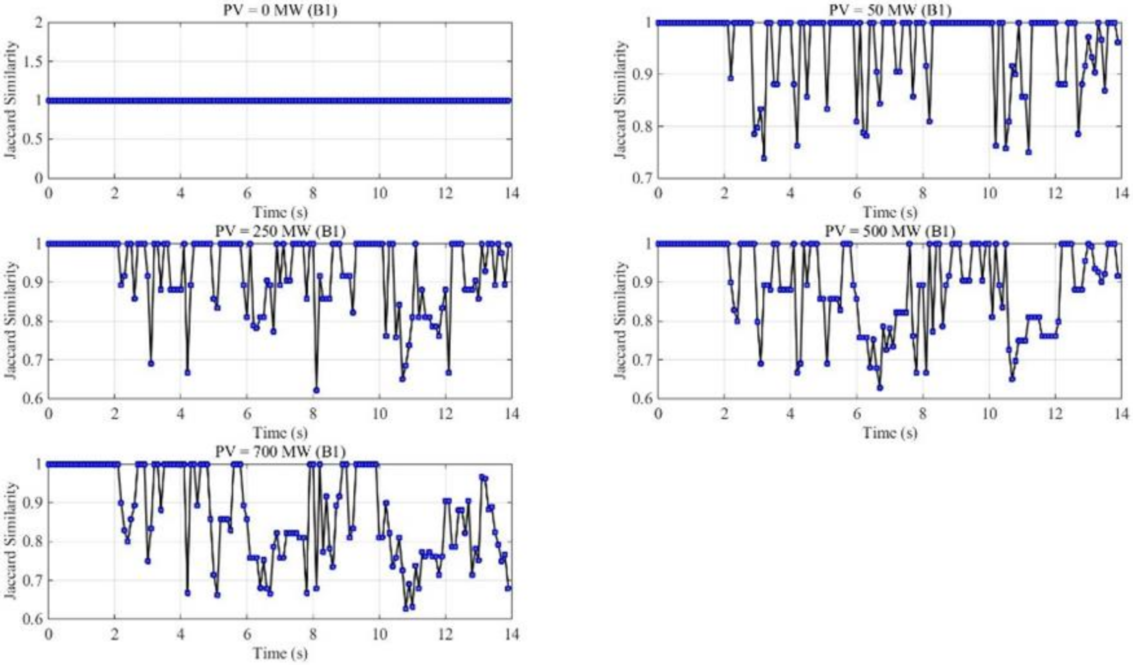

Figure 6. 6 The Jaccard similarity results for all PV penetration levels under the same fault conditions.

6.4.2 Fault Perturbed Coherency Grouping with Both PV Plant Penetration

Case 2- Three-phase faults with dynamic PV penetration in two areas

In this case study, two solar plants were simultaneously deployed in two distinct areas that penetrated the test bed with dynamic PV power (see Figure 6.7a). The similar tie-line Bus faults (Bus 8 at Area 1 and Bus 1 at Area 2) were initiated unlike that of Case 1. The corresponding frequency oscillations were presented in Figure 6.7b for a 500-second time period, and the multi-timescale data window VGIs and VSIs are presented in 2s, 5s, 10s, 30s, and 60s starting from *t*+66s (Bus 8 fault) or *t*+397s (Bus 1 fault). Therefore, in such circumstances, the operator has access to the global changes in the dynamic behavior of the system according to the GVIs and SVIs, as shown in Figures 6.8 and 6.9. Similar to the case 1 result, the GVIs, and SVIs decreased after 10s indicating a quick return of the system to a stable status.

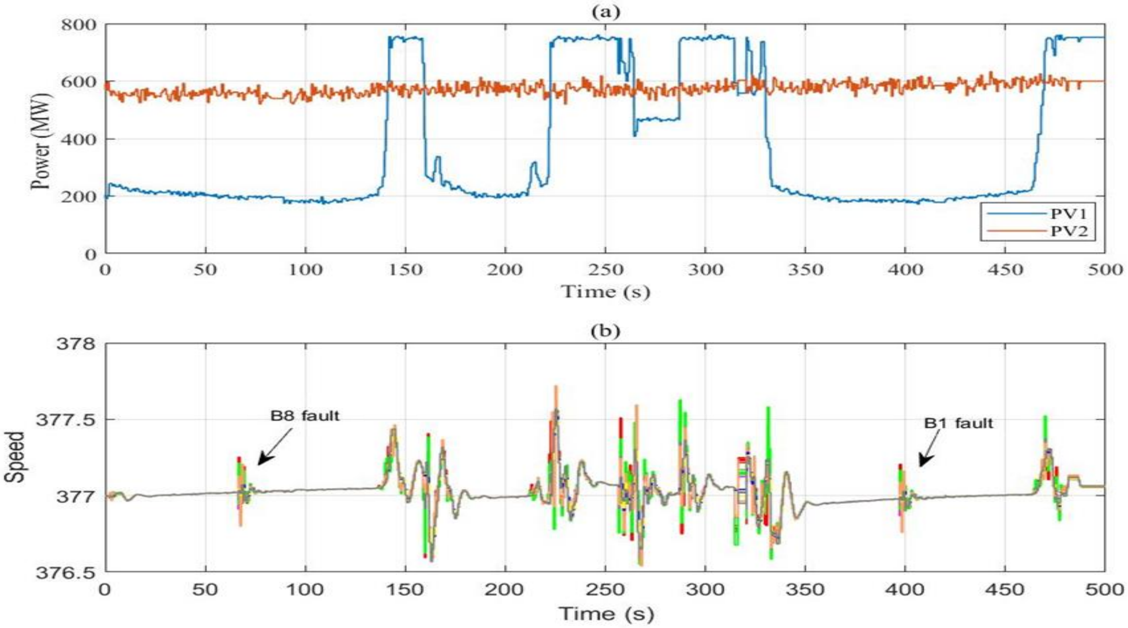

Figure 6. 7 (a) The dynamic PV power penetration on both Areas; (b) All 16 generator speed responses.

Case 3- Unexpected Dynamic PV Power Integration

For case 3, the PV plants utilized dynamic unbalanced solar irradiance to provide complex and severe disturbances for this multi-area power system coherency analysis. As can be seen in Figure 6.7a, the PV 1 in Area 1 explored several unexpected output power changes during the simulation, these specifically being a sudden spike and decrease in the PV power which was *t*+136s and *t*+329s, respectively. The duration time of the PV power change was 15s (indicating power-up) and 26s (indicating power-down). The all 16 generators' inertia H_{Gi} were 5.25; 3.553; 3.58; 3.575; 3.467; 3.480; 3.520; 3.471; 3.450; 3.543; 2.169; 4.615; 4.960; 3.000; 3.000; and 4.500, respectively. The corresponding GVIs and SVIs for five same data windows were shown in Figure 6.10 and 6.11. In this circumstance, the GVIs and SVIs did not decay within 15s comparing to cases 1 and 2 but rather increased after 10s owing to the continuous PV changes. The result was a larger display in the long-term observation window. In these simulations, the short term indicates for 2s, 5s, and 10s while the long-term for the 30s and 60s incorporating with the generator fluctuation behaviors.

The inference table of vulnerable generators for cases 2 and 3 are summarized in Table 6.5 based on GVIs and SVIs. The summary depicts the vulnerable generators vary for multiple time intervals as well as for different disturbances. With faults only disturbances applied at buses, the vulnerable generators existed for both short and long term based on the GVI and SVI results; however, disturbances with the PV power up or down, the vulnerable generators only appeared in the short term with similar but fewer generators. Bus faults are strictly worse case for the grid suffering compared to the PV power changes as can be expected, but the GVI and SVI result also present that the venerable generator outcome of the PV involved disturbances are as same as the bus fault cases. The operator needs to separate them correct for further actions. Therefore, though the GVI and SVI metrics, the operator could distinguish the dominant cause of the system abnormal and prepare for a different emergency plan.

The GVIs and SVIs are designed as a quick warning for the operator under disturbances. By comparing the different GVIs and SVIs behavior pattern during a disturbance, the operator can develop different load-frequency balancing strategies to manage the post-disturbance prior to occurrence. Therefore, in this study, five different data windows are presented that all address the multi-purpose environment.

Table 6. 5 the inference table of dynamic PV disturbances in cases 2 and 3

Fault/Variations	**Dominant GVI**		**Dominant SVI**		**Venerable Generator**	
	Short term	***Long term***	***Short term***	***Long term***	***Short term***	***Long term***
B8 fault at 66s	G1, G8, and G14	G1 and G8	G1 and G8	G1	G1, and G8	G1
B1 fault at 397s	G1, G8, and G12-14	G12, G13, and G16	G1, G8, G12, and G13	G1, and G13	G1, G8, G12, and G13	G13
PV1 power increases at 136s	G9, G10, and G12	G9, G10, G12, and G16	G9, G10, and G12	N/A	G9, G10, and G12	N/A
PV1 power decreases at 329s	G9, G12, G13, and G16	G9, G12, G13, and G16	G9 and G16	N/A	G9, and G16	N/A

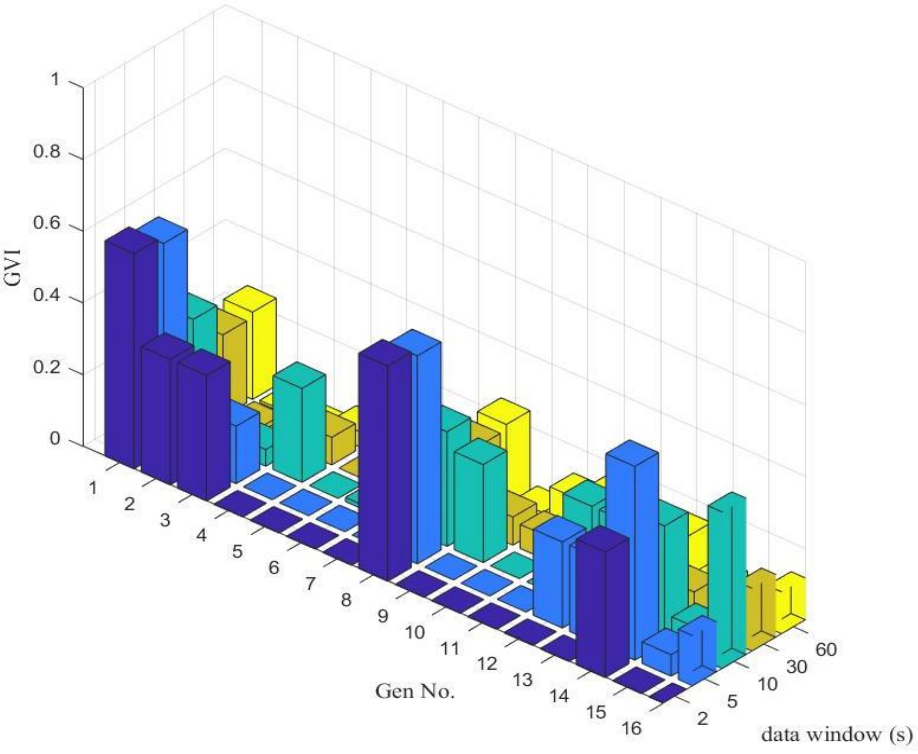

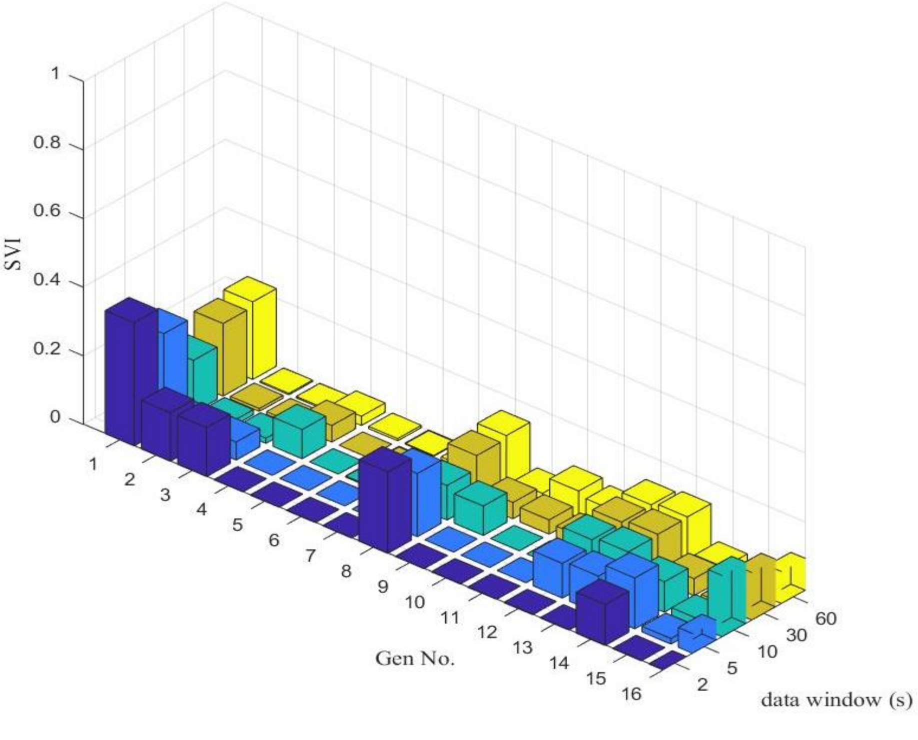

Figure 6.8 GVI and SVI results for multiple data windows beginning at 66s referring to a three-phase fault at B8.

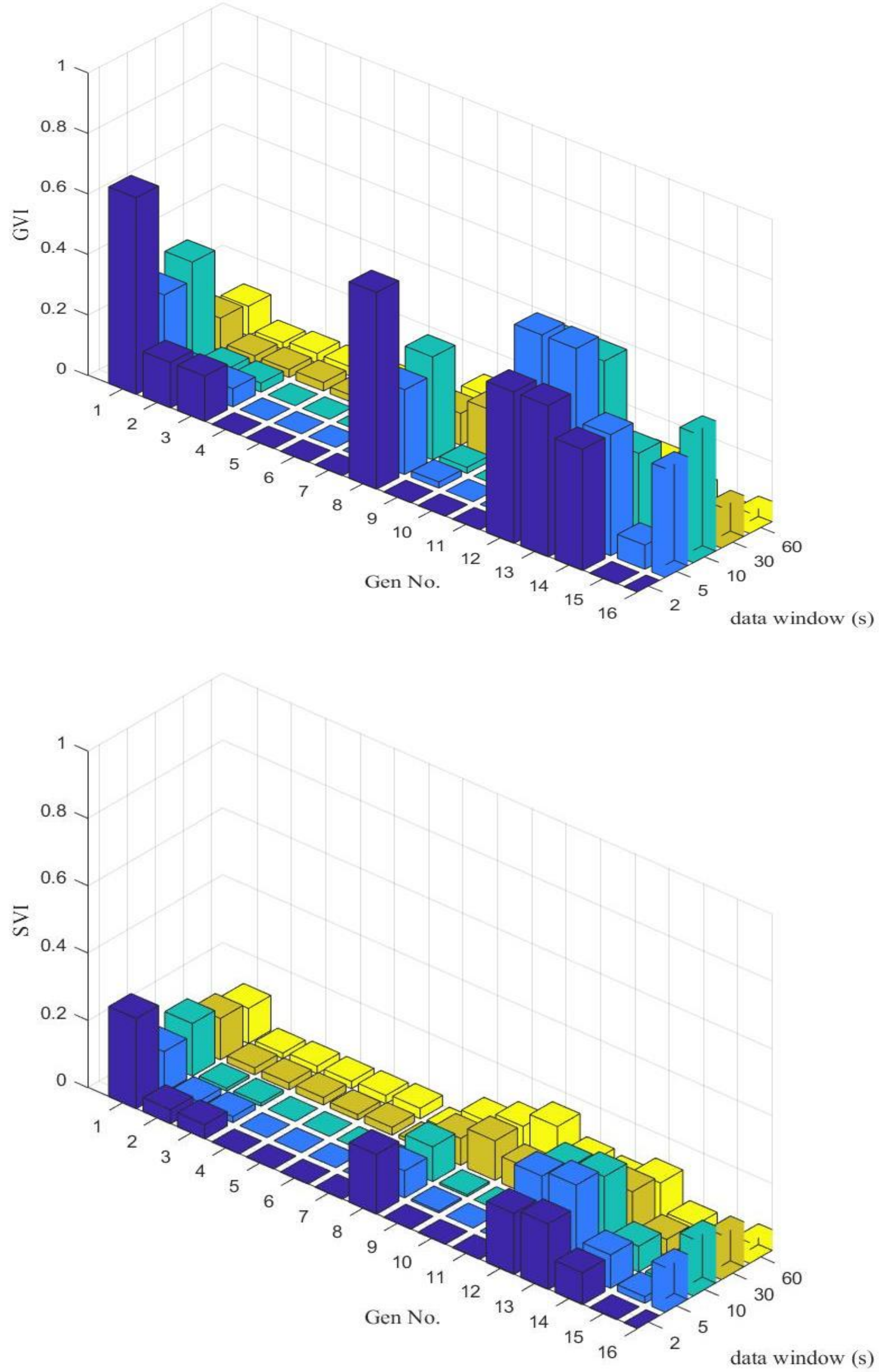

Figure 6. 9 GVI and SVI results for multi-data windows beginning at 397s referring to a three-phase fault at B1

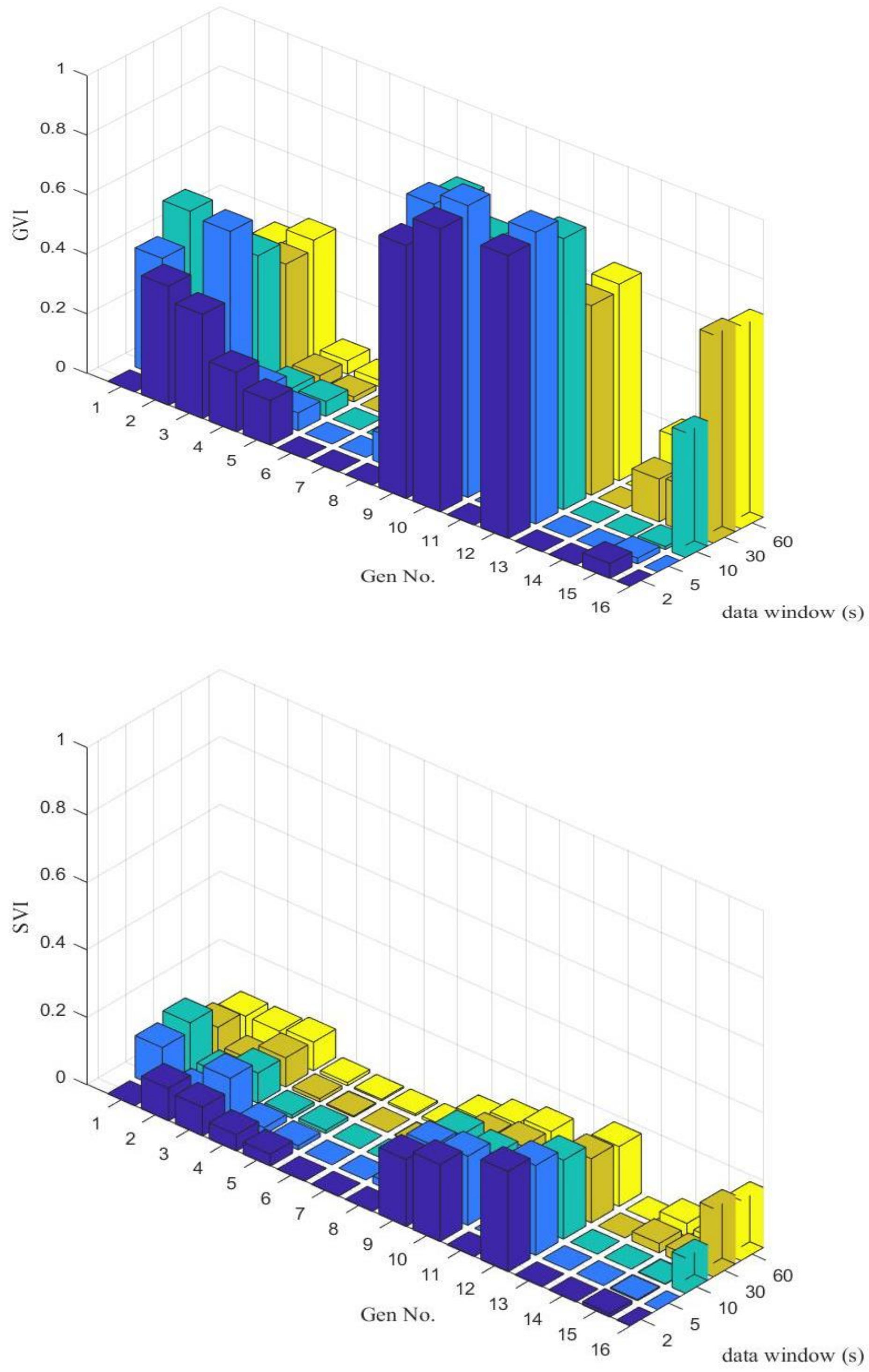

Figure 6. 10 GVI and SVI results for multiple data windows beginning at 136s referring to a sudden PV1 power increasing at Area 1.

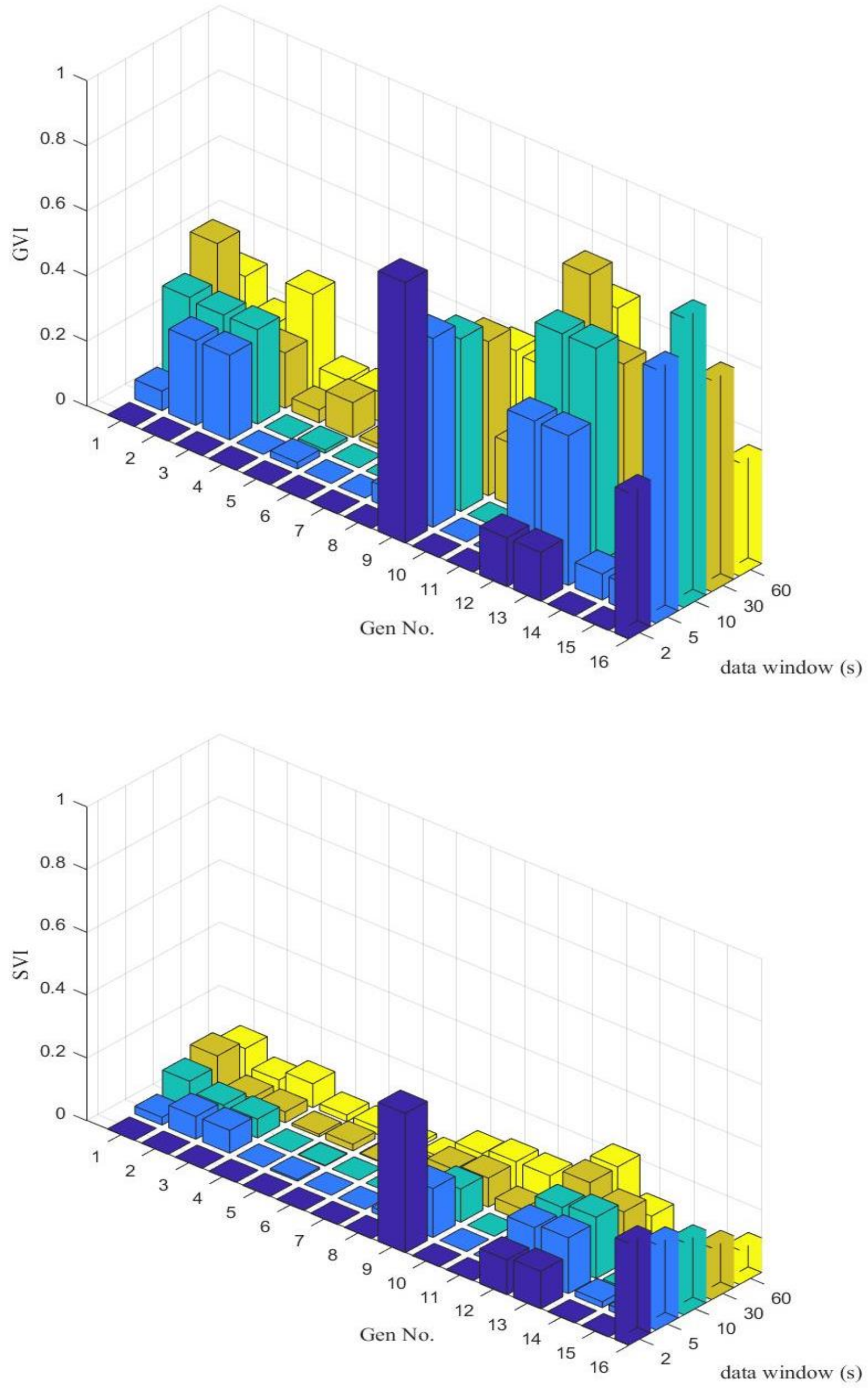

Figure 6. 11 GVI and SVI results for multiple data windows beginning at 329s referring to a sudden PV1 power decreasing at Area 1.

6.4.3 Discussion

All of these case studies detailed above elucidate the effects of the online coherency grouping with PV penetration. After obtaining the new coherent groups, it is crucial to undertake a visualization and corresponding similarity analysis for differentiation. By studying the coherent grouping color region maps, JS values, and generator/system vulnerability indices, operators can quickly comprehend the current system status, especially during new emergency situations.

Electric girds are moving towards a more complicated hybrid-system characterized by the deployment of large numbers of utility-scale PV plants deploying and penetrating to the main grid. Although the stability is not determined by PVs during a fault or a similar severe disturbance, the behaviors of both the fault and post-fault system-wide generator change substantially, manifesting in a new operational challenge for transmission system management. This lack of a coherent overview of the interconnected main-grid means that any local emergency operations can adversely affect the attempt of the entire system to stabilize (i.e. settle down). Understanding the integrated performance of these generators a priori both in and out the control-region will eventually benefit from system operator decision-making or emergency controls.

6.5 Summary

This chapter elaborated a new algorithm, indices and visualization tools to enhance situational awareness in control centers and demonstrated using a real-time testbed. The coherency behavior of synchronous generators in presence of variable PV power can be identified using new tools online using synchrophasor data and actionable information is available to system operators to ensure the secure and stable operation of the power system during variable generation and severe system disturbances. This chapter elucidated a new online coherent grouping relationship between the MW-scale PV plants and the system conventional on-site generators. Real-time simulation results have been provided to illustrate the new indices and visualization tools developed. The next chapter will present the FSI implemented frequency predictions for generator coherency analysis.

CHAPTER 7

FSI FOR ONLINE COHERENCE ANALYSIS

7.1. Overview

As demonstrated in the previous chapter, the coherency analysis reveals the dynamic behavior of synchronous generators in a system-wide perspective. In this chapter, frequency situational intelligence is integrated to provide frequency predictions for synchronous generator coherency grouping. Instead of using the actual frequency measurements captured via PMUs, the coherency grouping utilized predicted frequencies for mitigating the latency. Multi-timescale frequency predictions, as 100 *ms* and 200 *ms* ahead, enable the coherency grouping to provide an insight to the synchronous generators' coherent behaviors a priori.

7.2. Frequency Situational Intelligence for Prediction

The aforementioned CCN structure is adopted for frequency prediction. In this study, the computing algorithm utilizes the MLP method and the learning algorithm is the backpropagation method. The IEEE New-England and New-York benchmark model, as introduced in chapter 2, is used for validation. The corresponding cell-oriented system simplification is shown in Figure 7.1. As can be seen, each generator is connected with two or three nearest neighbors. As an example, the CCN based frequency prediction description for generator G1 is presented in (7.1).

$$\hat{f}_{\mathrm{G1}}(k+1) = F\{f_{\mathrm{G1}}(k), \Delta V_{ref-G1}(k),\ f_{\mathrm{G1}}(k\text{-}1), \hat{f}_{\mathrm{G2}}(k),\ \hat{f}_{G8}(k),\ \hat{f}_{G10}(k)\} \qquad (7.1)$$

where the $\hat{f}_{G1}(k+1)$ stands for the k+1 frequency prediction; $\Delta V_{ref-G1}(k)$ is G1 reference voltage; $f_{G1}(k)$ and $f_{G1}(k-1)$ represent the historical inputs of G1; $\hat{f}_{G2}(k)$, $\hat{f}_{G10}(k)$ and $\hat{f}_{G8}(k)$ are known as the G1 closest neighbors frequencies with forecasting.

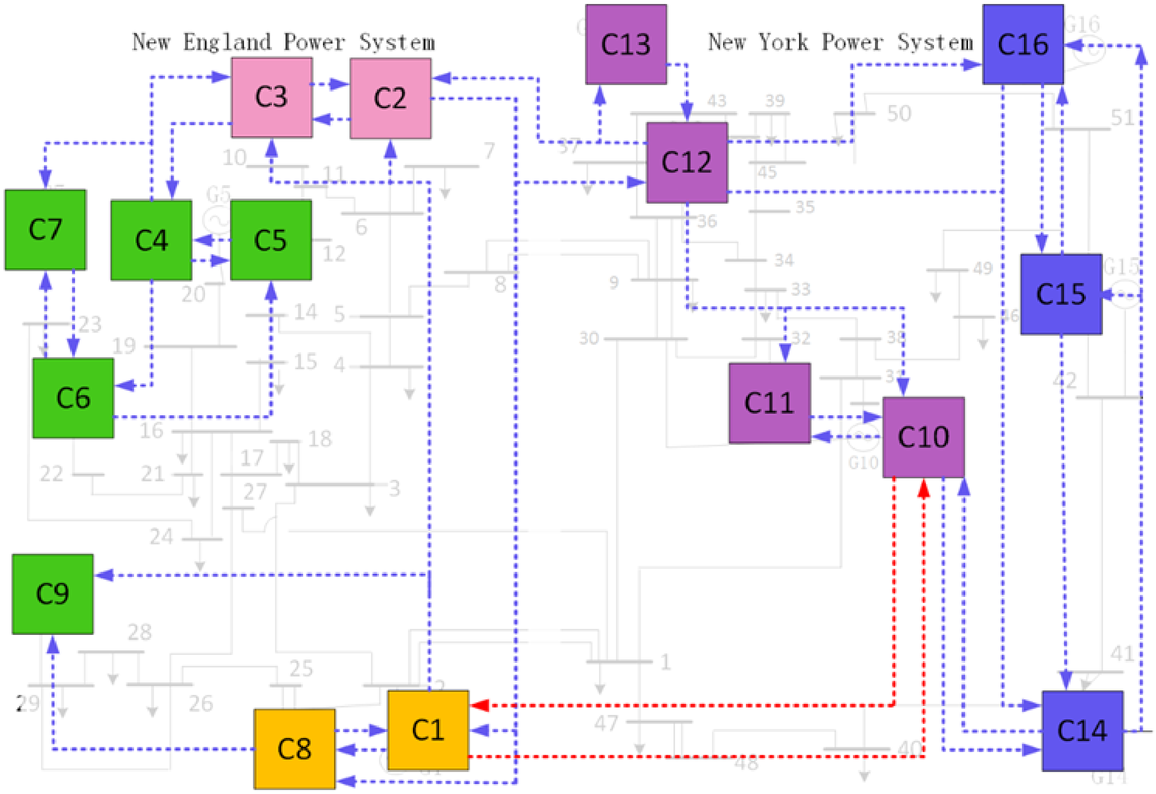

Figure 7.1 NE-NY IEEE benchmark power system. CCN cells are shown in boxes and coherent groups based on offline clustering are shown using colored boxes.

7.3. Online Coherency Analysis with FSI

The IEEE NE-NY benchmark system is chosen in this study. The system is modeled using the Real-Time Digital Simulator (RTDS); with PMUs on each generator bus. The pseudo-random binary signal (PRBS) is adopted for applying frequency fluctuations for CCN training process. The trained network is then applied for frequency predictions (in steps of 100 *ms* and 200 *ms* timescale ahead) under the three-phase line to ground fault 8 with adjustable fault duration time from 50 *ms* to 100 *ms*. Online coherency analysis with predicted frequencies of the generators is carried out using a 2-second sliding window at a sampling rate of 10 Hz. The overview of the online coherency analysis with FSI is shown in Figure 7.2.

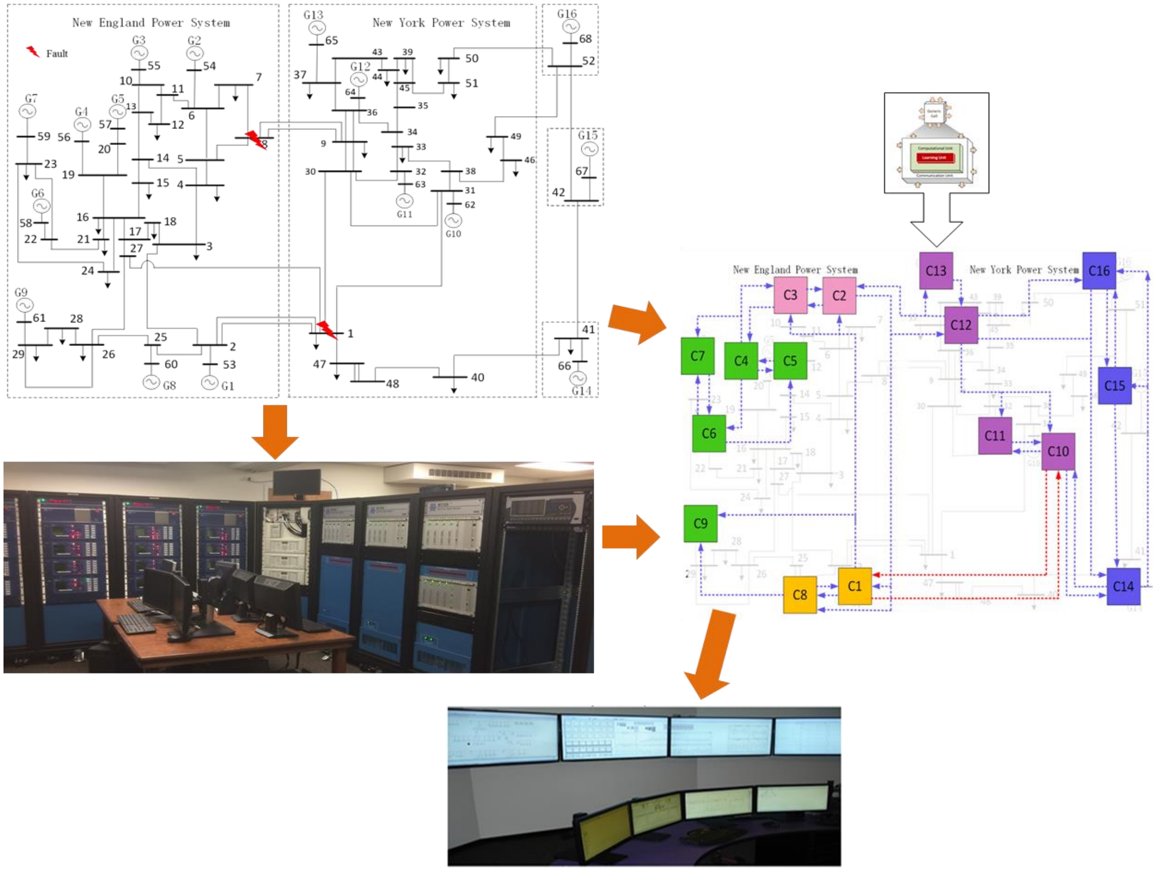

Figure 7. 2 The big picture of FSI integrated online coherency analysis.

7.4. Offline and online grouping results

7.4.1. Offline grouping result

The offline case was generated as the three-phase line to ground (3LG) fault in between bus 1 and 2 for 50 *ms* fault duration time. The CCN based frequency actual; 100 *ms* and 200 *ms* predictions are shown in Figure 7.3. In Figure 7.4, the all 16 generators frequency responses are presented with coherent groups. G1 and G8 are grouped in blue lines, whereas the G2 and G3 are represented in green lines. G4, G5, G6, G7, G9 are concentrated in yellow lines, whereas black lines groups the G10, G11, G12, and G13. In the end, G14, G15, G16, and G17 are grouped in red lines. Table 7.1 presents the comparison results between actual and 200 *ms* ahead predictions.

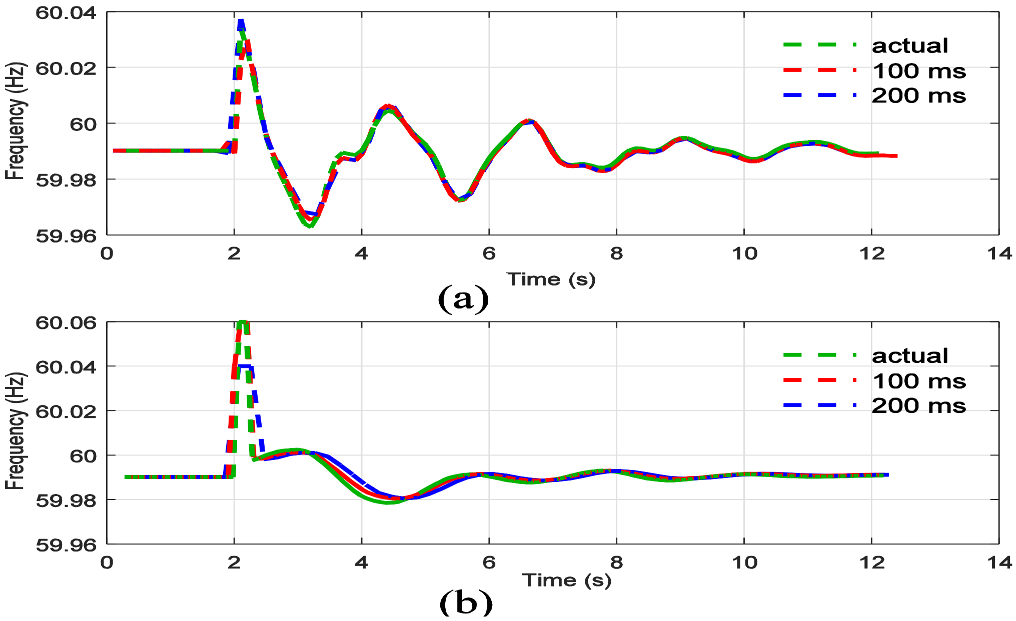

Figure 7.3 100 *ms* and 200 *ms* Frequency prediction comparisons for selected two coherency groups in Figure 6.1. (a) G1 offline group 1 and (b) G16 offline group 5.

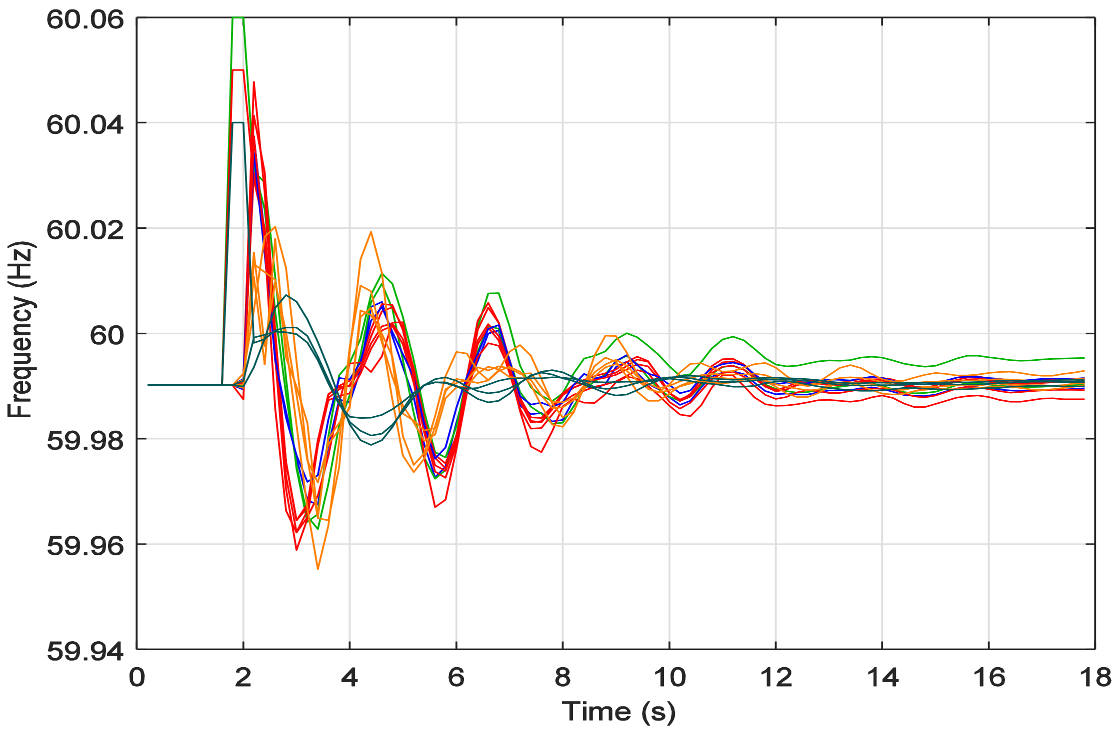

Figure 7.4 Frequency responses of the 16 machines in Figure 7.1.

Table 7.1 offline Clustering Result

Group Index	**Actual**	**Predicted (200 *ms*)**
1	G1, G8	G1, G8
2	G2, G3	G2, G3
3	G4, G5, G6, G7, G9	G4, G5, G6, G7, G9
4	G10, G11, G12, G13	G10, G11, G12, G13
5	G14, G15, G16	G14, G15, G16

7.4.2. Online grouping result

Case I. A 100 *ms* three-phase short circuit fault at bus 1.

A 100 *ms* 3LG fault was applied at bus 1 at t = 2 *s*. The frequency predictions using CCN are presented in Figure 7.5 with actual measurements for the first 12 seconds. The frequency response and online coherent generator groups are shown in Figures 7.6 and 7.7, respectively. Table 7.2 presents the actual measurement based offline grouping results versus 200 *ms* prediction based results for all 18 seconds. The online coherent groups with predicted frequencies are presented in Table 7.3 (snapshots for an actual time at 8 *s*, 10 *s*, and 15 *s*). Note that the online clustering result with predictions is given the identical coherency analysis 200 *ms* ahead regarding the actual time instance.

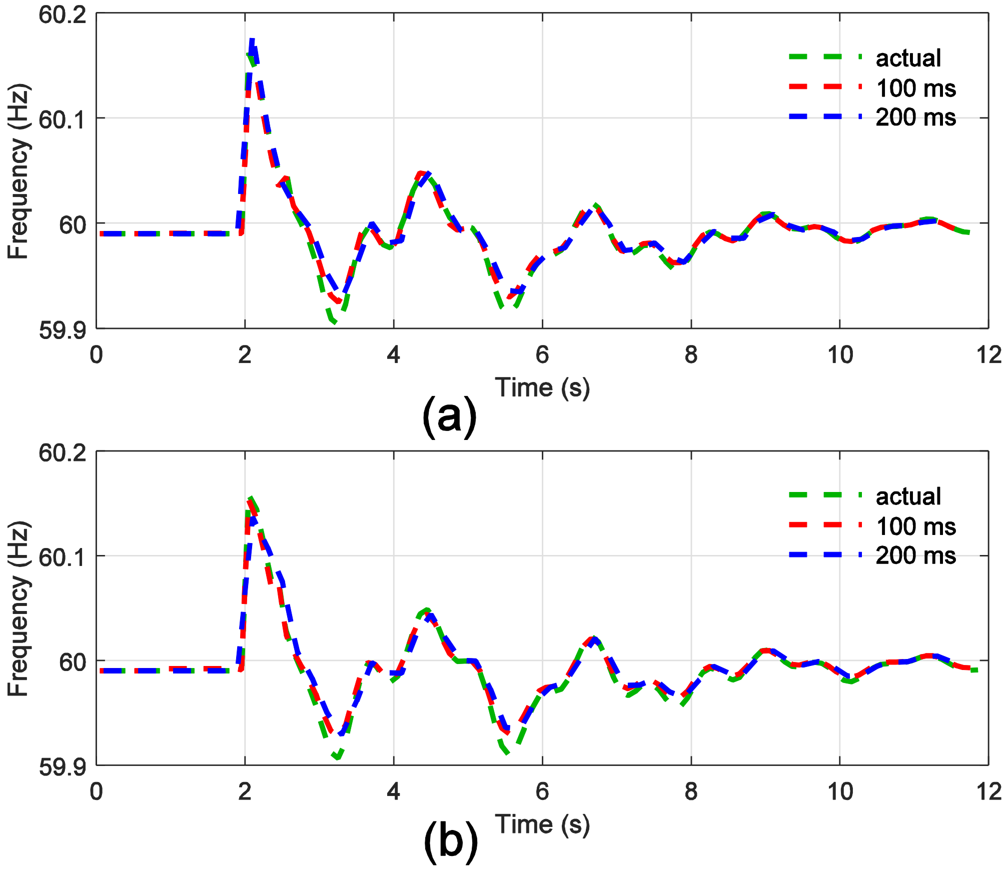

Figure 7.5 Case I selected coherency groups 100 and 200 *ms* frequency predictions for bus 1 3LG fault. (a) G1 for group 1 and (b) G14 for group 7.

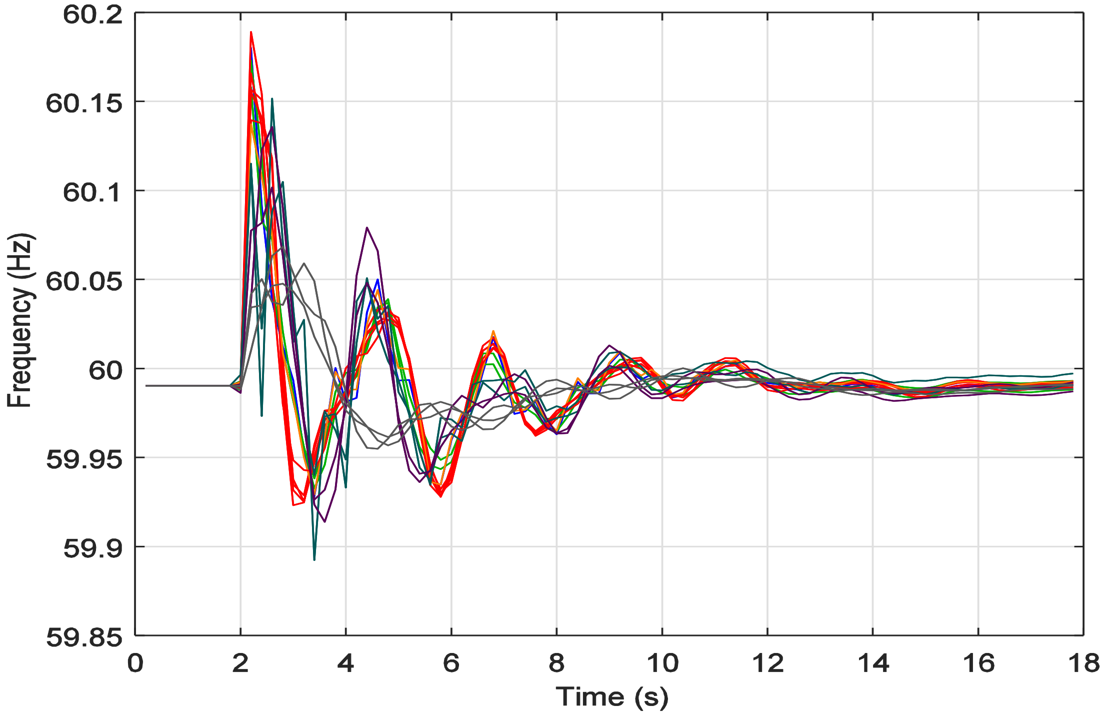

Figure 7.6 Frequency response for bus 1 3LG fault at Figure 7.1

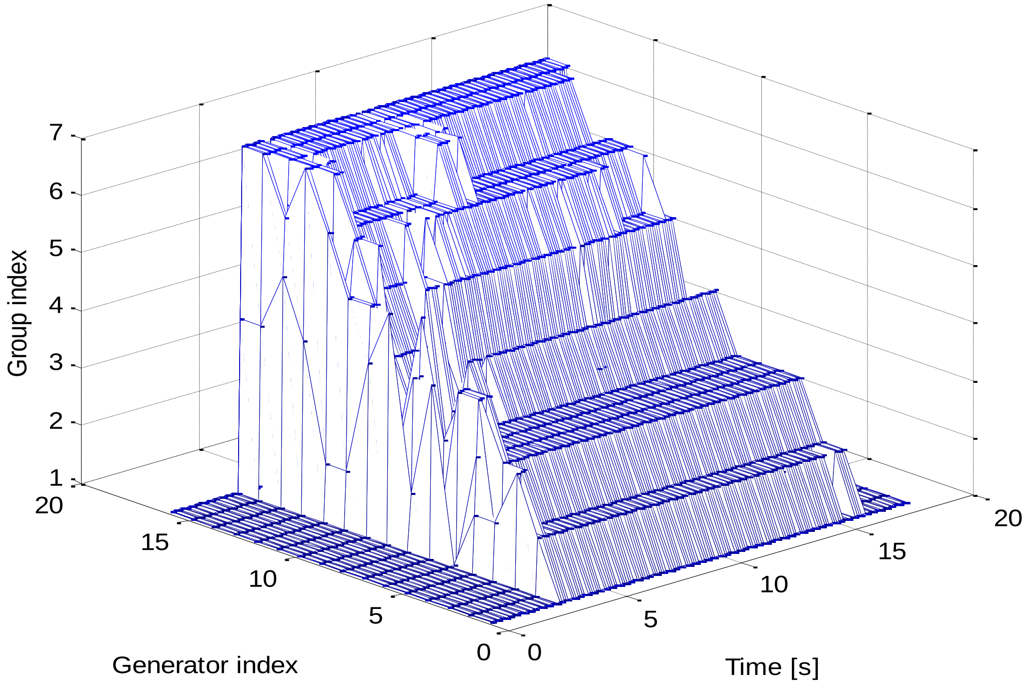

Figure 7. 7 3D online coherent machine groups for bus 1 3LG fault in Figure 7.1

Table 7.2 Coherency Grouping Result for Case I

Group Index	Actual	Predicted (200 *ms*)
1	G1	G1
2	G2, G3	G2, G3
3	G4, G5, G6, G7, G9	G4, G5, G6, G7, G9
4	G8	G8
5	G10, G11	G10, G11
6	G12, G13	G12, G13
7	G14, G15, G16	G14, G15, G16

Table 7.3 Case I : Online Coherency Grouping Based on Predicted and Actual Data

Group Index	Predicted at 7.8 s	Actual at 8 s	Predicted at 9.8s	Actual at 10 s	Predicted at 14.8 s	Actual at 15 s
1	G1	G1	G1	G1	G1	G1
2	G2, G3	G2, G3	G2, G3	G2,G3	G2,G3	G2,G3
3	G4, G5, G6, G7, G9	G4, G5, G6,G7,G9	G4, G5, G6, G7, G9	G4,G5, G6,G7,G9	G4,G5,G6, G7,G9	G4,G5,G6, G7,G9
4	G8	G8	G8	G8	G8	G8
5	G10,	G10,	G10,	G10,	G10, G11	G10, G11
6	G12, G13	G12,G13	G11,G12, G13	G11,G12,G13	G12, G13	G12, G13
7	G11,G14,G15, G16	G11,G14,G15, G16	G14, G15, G16	G14,G15, G16	G14,G15,G16	G14,G15,G16

Case II. A 100ms three-phase fault at bus 8.

A similar 100 *ms* 3LG fault was applied at bus 8 as t = 2s. The frequency response and online coherent generator groups are shown in Figures. 7.8 and 7.10, respectively. The frequency predictions using CCN are presented in Figure 7.9 with actual measurements for 12 seconds. The online coherent groups with predicted frequency values are presented in Table IV (snapshots for an actual time at 8s, 10s, and 15s). Table 7.5 presents the actual measurement offline group results versus 200 ms predictions coherent results for 18 seconds.

Comparing Figures 7.7 and 7.9, the 3D-online coherent groups present that the more serious fault is, the more severe generator grouping changes. In such circumstance, offline and fixed grouping is not sufficient, thus predicted online grouping is applied and providing situational intelligence in grid-wise.

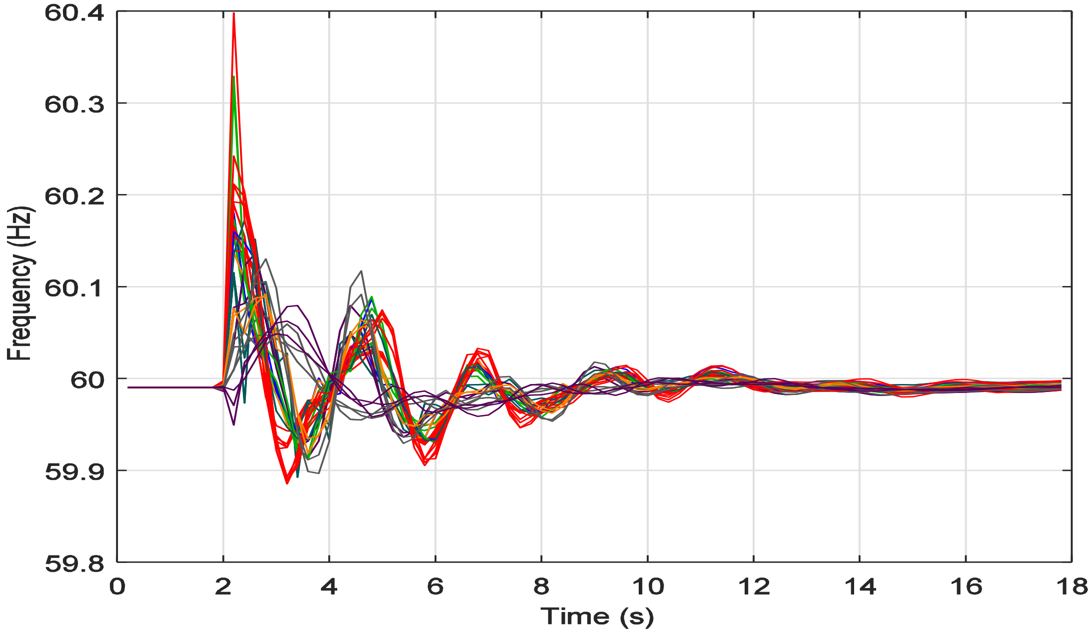

Figure 7. 8 Speed response of generators with a fault at bus 8.

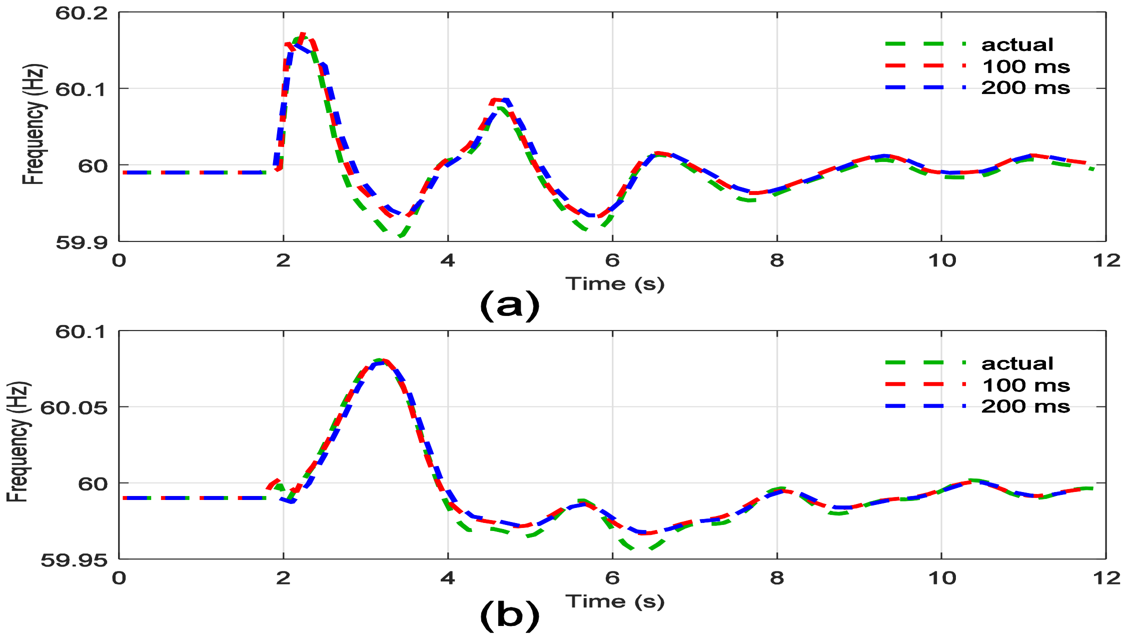

Figure 7.9 Case II selected coherency groups 100 and 200 *ms* frequency predictions for bus 8 3LG fault. (a) G1 for group 1 and (b) G15 for group 17.

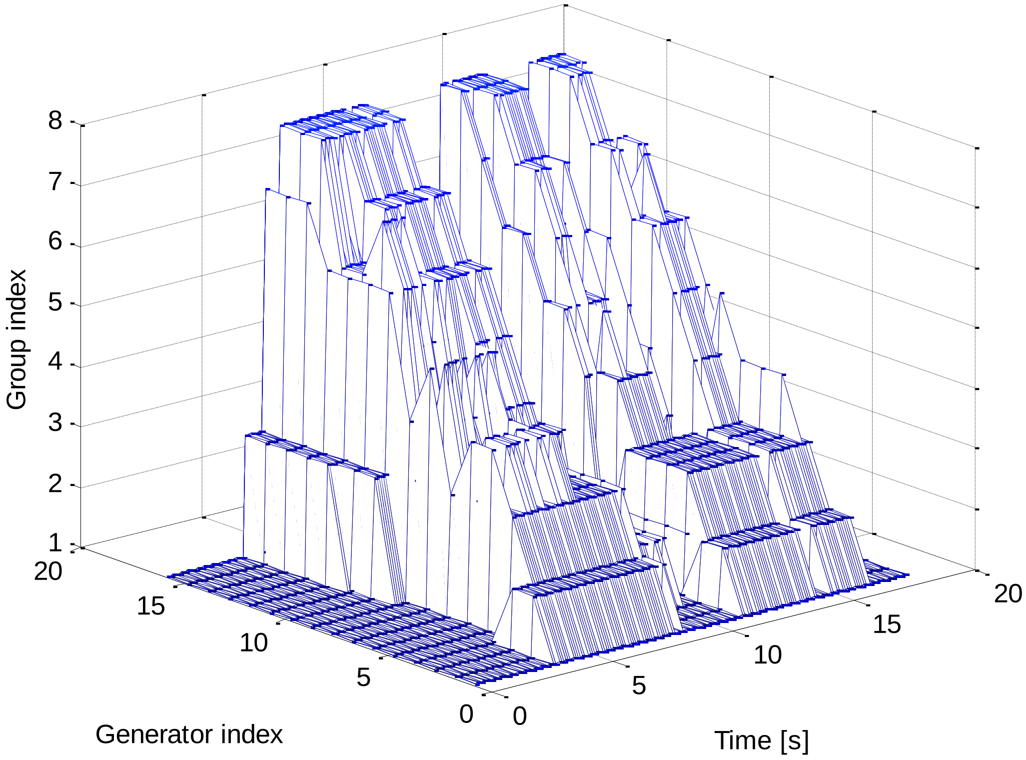

Figure 7.10 Online coherent generator groups for the fault at bus 8 in Figure 6.1

Table 7.4 Coherency grouping result for case II

Group Index	**Actual**	**Predicted (200 ms)**
1	G1	G1
2	G2, G3	G2, G3
3	G4, G5, G6, G7, G9	G4, G5, G6, G7, G9
4	G8	G8
5	G10, G11	G10, G11
6	G12, G13	G12, G13
7	G14, G15, G16	G14, G15, G16

Table 7.5 Predicted and actual data compared coherency grouping result for case II

Group Index	Predicted at 7.8 s	Actual at 8 s	Predicted at 9.8s	Actual at 10 s	Predicted at 14.8 s	Actual at 15 s
1	G1, G8	G1 G8	G1, G2, G3, G8, G10, G11, G12, G13	G1, G2, G3, G8, G10, G11, G12, G13	G1,G8	G1,G8
2	G2, G3	G2,G3	G4, G5,G6, G7,G9	G4,G5,G6, G7,G9	G2,G3	G2,G3
3	G4, G5, G6, G7	G4,G5 G6,G7	G14, G15, G16	G14, G15, G16	G4,G5,G6, G7,G9	G4,G5,G6, G7,G9
4	G9	G9			G10, G11, G12, G13	G10, G11, G12, G13
5	G10, G11	G10,G11			G14, G15, G16	G14, G15, G16
6	G12, G13	G12,G13				
7	G14,G15,G16	G14,G15,G16				

7.5. Summary

This chapter elaborated the predicted frequency included generator clustering under different fault situations. The online coherent analysis method adopted KHMC method for online coherency grouping comparison. Based on the result, the frequency predictions achieved the same result as the actual measurements. Thus, the FSI is demonstrated for mitigating the system latency without lowing the accuracy

CHAPTER 8

OPTIMAL AUTOMATIC GENERATION CONTROLLERS IN A MULTI-AREA INTERCONNECTED POWER SYSTEM UTILITY-SCALE PV PLANTS

8.1 Overview

The interconnection of bulk power systems has greatly accelerated the growing market percentage of centralized utility-scale Photovoltaic (PV) plants, a growth, however, which has been characterized by uncertainty and variability in the management of system frequencies. Consequently, the successful integration of solar PV power in large-scale power systems requires a reliable and efficient multi-area Automatic Generation Control (AGC) system within the control center. Specifically, Area-AGCs that perform tie-line bias control, in which the area frequency regulates the tie-line power flow, must balance the operational control area supply power-and-demand loads within a pre-tuned parameter set. Traditional AGC control systems have area linear controllers that must be periodically tuned to manage the high fluctuation of PV power.

Therefore, in this chapter, a two-step tuning, and an asynchronous tuning method have been developed and applied to determine the different optimal parameters for multi-area AGCs working in different situations. A five-area multi-machine power system with two large PV plants is used as the exemplar. The power system was equipped with the synchrophasor based monitoring system, with a real-time simulation platform serving as the application host.

8.2 Automatic Generation Control Review

8.2.1 Classic AGC Scheme Design

AGC must function rapidly and optimally in a system to ensure a minimum Area Control Error (ACE). Although classical control techniques such as Proportional (P), Proportional-Integral (PI), and Proportional-Integral-Derivative (PID) are effective at load management, the extended scale, increased PV power, and structural merging means that AGC is no longer work-separated [45-46, 86]. Thus, the AGC parameter tuning is of critical importance in terms of practical power system operational especially given the interconnections with different generator types and network configurations. Although Ziegler Nichols and trial and errors tuning methods are widely used classical control techniques, the proper tuning of multi-area AGCs is difficult with such methods [86]. Moreover, the response time delays, nonlinearities, and generator rate constrain that characterize operations at aging power plants, optimal control methods, such as the Fractional-Order PID (FOPID) that uses reheated turbine and redox flow battery have been used to improve multi-area power system performance [87-88]. Similarly, a two-degree-of-freedom internal model control (IMC) method is available for PID controller tuning in a two-area system and the H_2/H_∞ control technique is utilized for load and generation balance control in a multi-area system [89]. An H_∞ damping control used in the linear matrix inequality (LMI) frame for the multi-sensitivity formulation of multi-area AGC is also available as a multi-source controller with output feedback [90-92]. Note, however, that the H_2/H_∞ and H_∞ methods transform the multi-area AGC control problem into nonconvex bilinear matrix inequalities that may not converge to a global optimal result through iterative algorithms.

8.2.2 Soft Computing Algorithm Based AGC Scheme Design

Intelligent algorithms such as the Artificial Neural Network (ANN), Fuzzy Logic (FL), Genetic Algorithm (GA), Bacterial Foraging Optimization Algorithm (BFOA), Grey Wolf Optimizer (GWO), and Artificial Bee Colony (ABC) method are all options for multi-area AGC implementation. A multilayer perceptron ANN used for reinforced learning in a three-area power system is characterized by an FL algorithm linearizing the target into a mathematic model followed the use of *a priori* knowledge to solve the problem [93]. However, local minimization characterizing these NN based methods encounter means using only proper initial conditions. FL controller based AGC, GA controller based AGC, and a neuro-fuzzy controller are available for multi-area controls [94-100]. Other available intelligent algorithms include a BFOA method for managing the tuning fraction-order-PID AGC controller, a GWO method embedded AGC with wind power penetration, and the ABC method for multi-area AGC tuning [101-103]. Particle Swarm Optimization (PSO) is effective in solving multi-dimension optimization problems [105-110]. Regarding specific PSO concepts, the chaotic PSO method, characterized by a self-adaptive configuration, schedules the short-term hydro-system generation and then tunes the integral gains [105-106]. Further research has been undertaken to combine the craziness based PSO and the hybrid bacterial foraging method for tuning multi-area AGCs [107]. A PSO based fuzzy PI controller is also available for multi-area AGCs [108-109]. Finally, an adaptive deadbeat controller provides a fast frequency response to the National Grid system operability framework of Scotland [110]. Clearly, the GA and PSO based metaheuristic optimization algorithms indicate its efficacy in solving complex power-system optimization problems. However, their tuning process is separate from the system as a learning mode and leaves the development of multi-area system global tuning as a remaining task. Currently, the task upgraded harnesses rather than curtails a large amount of PV power while ensuring the independence of the control area load-generation balance.

8.2.3 Multi-lateral AGC Design for Energy Imbalance Market

Most of the established onsite AGCs service their power system with outdated requirements which are designed in a time with mostly considering conventional high inertia, slow fluctuation fossil fuel plants in local balancing areas [45]. As can be expected, these on-duty AGCs will be challenged coping with the complex dynamic fluctuations generated by the PV power plant. Moreover, the Supervisory Control And Data Acquisition system (SCADA) needs to be upgraded as two slow to catch the frequency excursion with a typical sampling rate of 2-4 second [43]. Recently, the Wide Area Measurement System (WAMS) using PMUs has provided an enhanced monitoring infrastructure with a 30 to 60 Hz sampling rate. Comparing to the SCADA system, the WAMS opens the tuning possibility for AGCs of multi-area interconnected power systems with the frequency and tie-line power close observability. As such, the Independent System Operator (ISO) in different balancing authority (BA) now can facilitate low-cost PV power to meet real-time consumer demand over multiple BA's geographic areas through the Energy Imbalance Market (EIM) in the western region [111-112].

Most of the effective PV power consuming within the EIM is bilateral or trilateral balancing, which brings a new requirement for AGC cooperation in the corresponding area. Recent studies on the multi-area AGC cooperation for multiple ISOs focus on two parts: distributed AGC scheme [113-116] and globalized AGC parameter tuning [117-118], and [35]. In [114], a web-of-cell based distributed load frequency control has encapsulated both the primary governor control and the secondary AGC control with local direct measurements, therefore the control and information exchange between neighbors are independent for operators. Ref. [115] and [116] discuss the generation companies (GENCO) and distribution companies Participation Factor (PF) for distributed AGC scheme design. However, the distributed AGC deployment involves a wide range of electric grid participators as well as the ISOs, which is not a reachable solution within the near future. Refs. [117-118], and [35] optimize the multi-area together with different global evaluation settings. The tuned AGCs perform better, but lack of the test with sub-area (bilateral or trilateral) based power transfer balancing.

8.3 Two-step and Asynchronous Tuning Method for Multi-area AGCs

A two-step tuning method is first applied to the multi-area AGC parameters for a wide interconnected power system that encounters PV power. The purpose is to divide the multi-objective optimal problem into the respective global (first-step) and local (second-step) tuning processes. Thereby, the outcome can achieve the system-wide optimal value to satisfy the new emerging challenges of renewable energy source while maintaining balance performance in their corresponding control area. The developed two-step method is capable of tuning the parameters synchronously with first-step tuning involving by the simultaneous consideration of stability, disturbance tracking, and PV penetration, and second-step tuning involving a narrow of the search space into suboptimal spaces.

Thereafter, the asynchronous bilateral or multi-lateral tuning is developed and presented for multiple ISOs to adapt their AGCs with the prioritized neighbors for PV power transfer.

8.3.1. Performance Evaluation of the Multiple AGCs

Although multi-area AGC tuning includes a variety of attribute sets, which reflects the changing performance, it is possible to circumvent this challenge by compounding to formulate this constrained optimization problem [104]. It is thus possible to use the designed cost function (8.1) with a variety of optimization algorithms to evaluate the AGC performance. Specifically, to minimize the cost function value in terms of tuning: the Integral of Time multiplied Absolute Error (ITAE), the Integral of Squared Error (ISE), the Integral of Time multiplied Squared Error (ITSE) and Integral of Absolute Error (IAE). A comparison of these methods means that any cost function for multi-area AGC tuning must entail calculating the cumulated ACE of both positive and negative responses. Furthermore, in terms of multi-area AGC parameter tuning, the outcome will affect the entire power system for a sensitive control system. Further, in comparison with ITAE, although the ITSE has both time and deviations, they manifest in smaller amounts, making it more suitable for AGC tuning. Thus, the general cost function is a summation of the normalized ITSE for the tie-line power ACE values in all areas with the application of load step changes. The expression is as follows:

$$\begin{aligned}&\min_{J} \quad J=\sum_{i=1}^{n}\sum_{T=t_0/\Delta t}^{t_2/\Delta t} |ACE_i(T)| \times (A\times \Delta t)\\&s.t. \quad \rightarrow \forall n \in \mathbb{Z}^{+}, n=\{1,\ldots,s\}\end{aligned} \tag{8.1}$$

where i and ACE_i represent the tie-line power ACE values in Area i; T the simulation time in seconds, Δt the simulation time-interval in seconds, t_0 the load change applied time, t_2 the simulation end time, A the constant value, and n the area number.

The first step of the tuning process requires tuning AGC parameters as a single unit. After first tuning completed, the final cost value of each AGC is saved and sorted in a descending order. The sequence of the tuning in this second step is based on the cost evaluation results in which the AGC with the worst performance is tuned first. Herein, in the second step, using the results from the sorted AGC order created in the first step, each set of the AGC parameter is updated for the enhanced second-step tuning.

The first step tuning focuses on global searching and second step tuning focuses on local searching. Therefore, tuning boundary parameters in the second step (local) are restricted to a smaller search space than a first step (global). For n AGCs, n time second tunings are conducted to dramatically reduce the dimension of the to-be-tuned AGCs in this step. Herein, the computation numbers are less along with faster computing time. The multi-area AGC two-step tuning (global-local tuning) overview is shown in Figure 8.3.

8.3.2. Two-step AGC Tuning Process

The two-step tuning method is a general framework designed to figure out the suitable parameters for AGCs working in an interconnected power system with PVs. The inner searching algorithms have no limitation for each tuning step. In this paper, it shows demonstration results based on Particle Swarm Optimization (PSO). PSO is a heuristic optimization method that is suitable for complex system optimization problems [104-105].

By setting the objective function, PSO can provide system-wide optimal value to satisfy the demand. For the tuning of multi-area AGC parameters, PSO searches all AGC parameters in a single loop. However, the required time for tuning increases exponentially with a corresponding increase in the area number. To compare and simplified the coarse and fine tuning results, PSO algorithm is utilized in both tuning steps in this study.

8.3.3. Asynchronous AGC Tuning Process

Similarly, as the two-step tuning method, the performance evaluation formula for asynchronous tuning utilizes the integral of squared error but includes tie-line power flows and tie-line bus frequencies.

$$\begin{aligned}
\min_{J_i} \quad & J_i = \int_{t_i}^{t_{ss}-t_i} [\alpha_1(\sum_i \Delta f_i)^2 + \alpha_2(\sum_i ACE_i)^2 + \\
& \quad \ldots + \alpha_3(\sum_i P_{i-j})^2]dt \\
s.t. \quad & \rightarrow \forall i \in \mathbb{Z}^+, i = \{1, \ldots, n\} \\
& \Delta P_{ij\min} \le \Delta P_{ijss} \le \Delta P_{ij\max} \\
& \Delta f_{\min} \le \Delta f_{ss} \le \Delta f_{\max}
\end{aligned} \tag{8.2}$$

Where the ACE_i is the area control error between area i and j, P_{ij} is the tie-line power flow between area i and j, α_i is the weighting factor; t_i and t_{ss} are the initial and steady-state time of the rolling window. Δf_i is the frequency variation of area i.

The asynchronous AGC tuning flowchart is shown in Figure 8.2 and the corresponding five AGCs with direct information exchange between neighbor for bilateral or trilateral asynchronous tuning is shown in Figure 8.3, which uses the AGC 2 and AGC 1 as an exemplar.

8.3.4. Tuning Algorithm Using PSO

A general two-dimensional PSO algorithm searching process is depicted in (8.3), in which *Xp* and *Vp* represent the position and velocity of *p* th particle in a *d* dimensional space. The *Xpbest,p*, and *Xgbest* stand for the particle historical local best and the society global best for all particles.

Initiating a PSO requires the use of pre-defined upper and lower boundaries to randomly generate the position and velocity value of each particle. The expression of a general PSO velocity updating process is as follows:

$$\begin{aligned}
&V_p^{k+1} = wV_p^k + C_1R_1[X_{pbest,p}^k - X_p^k] + C_2R_2[X_{gbest}^k - X_p^k] \\
&s.t. \quad \rightarrow X_p^k(\gamma) \in \mathbb{Z} \cap \{X_{min}(\gamma) \le X_p^k(\gamma) \le X_{max}(\gamma)\} \\
&\qquad\;\; \rightarrow \forall \gamma \in \mathbb{Z}^+, \gamma = \{1, \ldots, n\} \\
&X_{gbest}(\gamma) = arg \min_{X_p^k(\gamma)} \{J_p^k, X_p^k(\gamma) \in [X_{min}(\gamma), X_{max}(\gamma)]\}
\end{aligned} \tag{8.3}$$

where k is the iteration number, w is the inertia weight; and C_1 and C_2 are the respective cognition and social acceleration constants, both of which are 2; and R_1 and R_2 the random numbers within the range of [0,1].

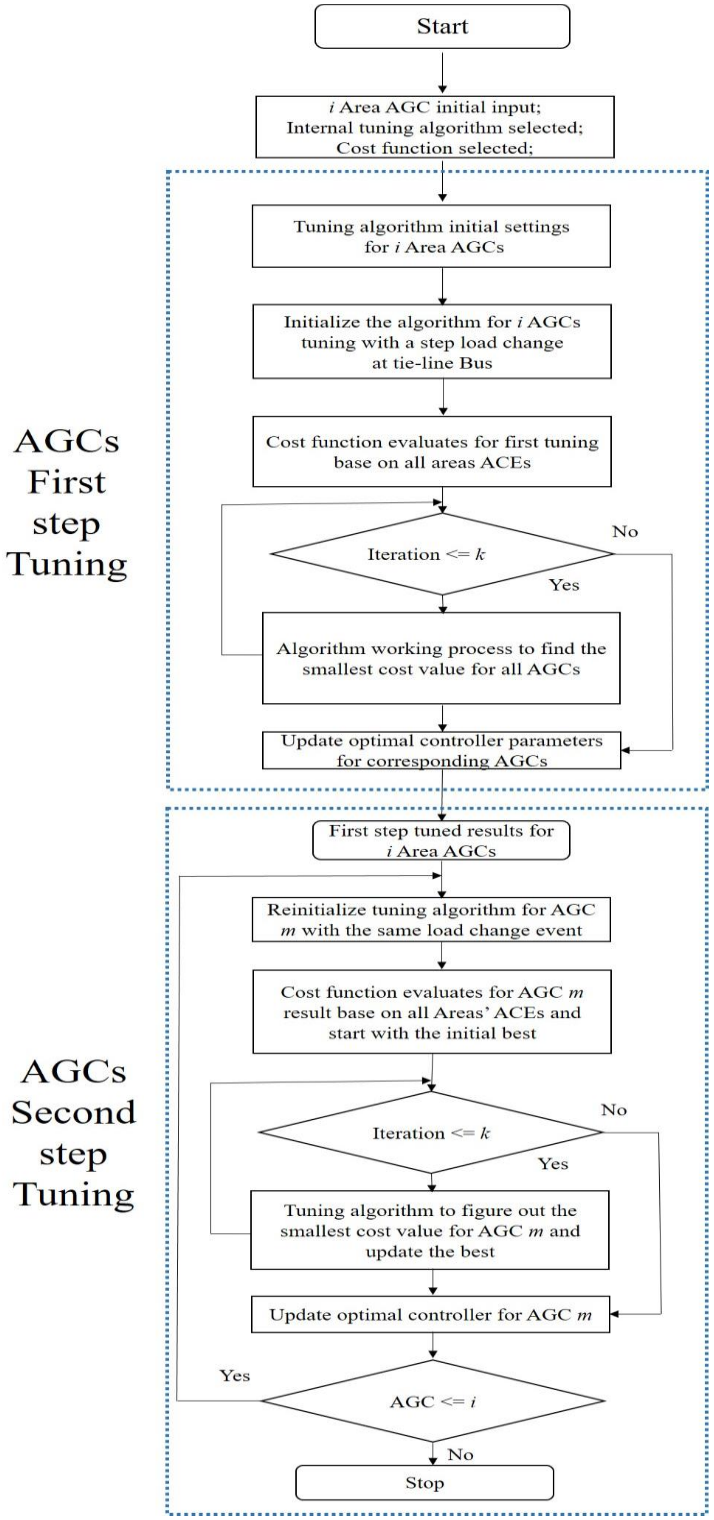

Figure 8.1 Multi-area multiple AGCs two-step tuning process.

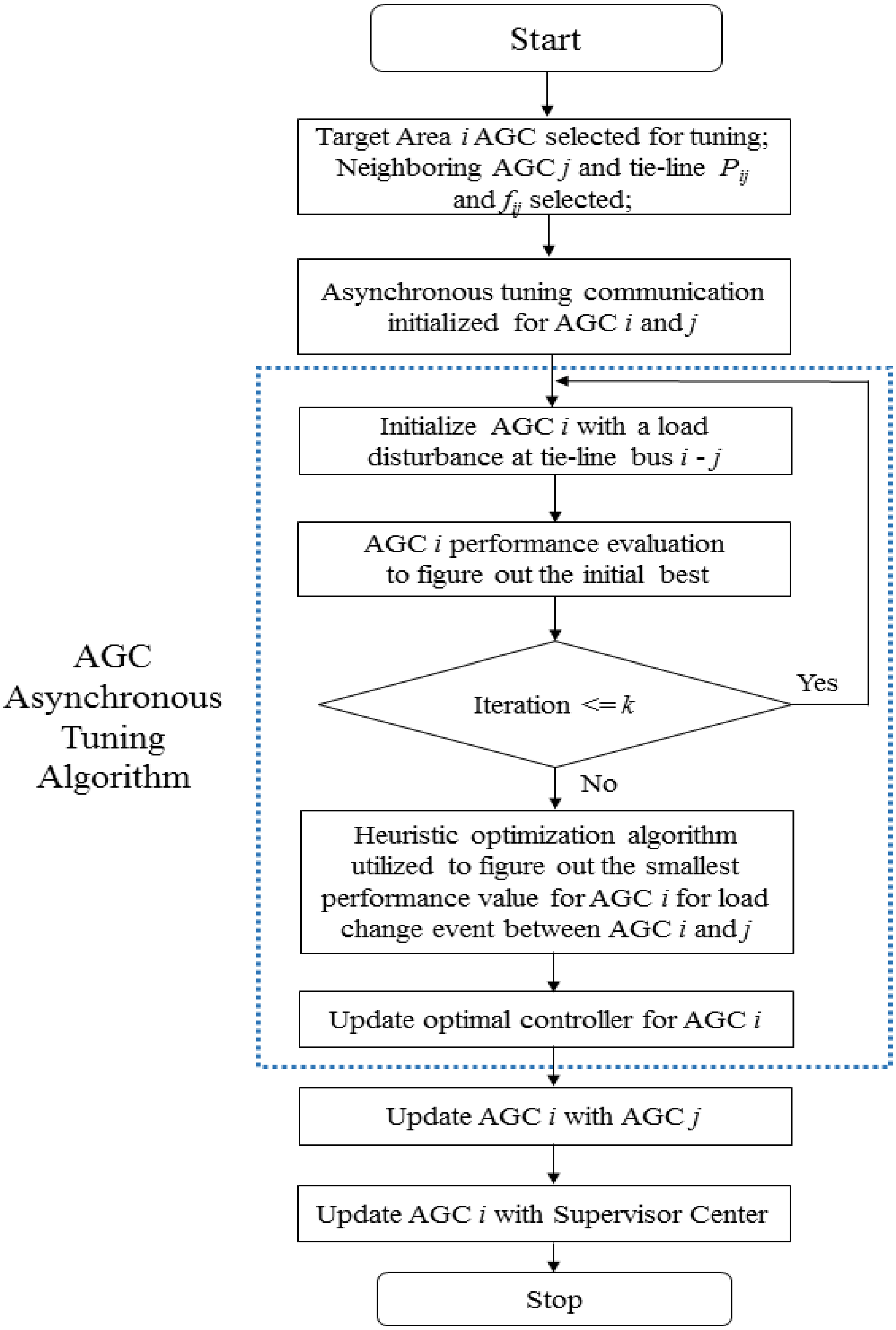

Figure 8.2 Multi-area multiple AGCs two-step tuning process.

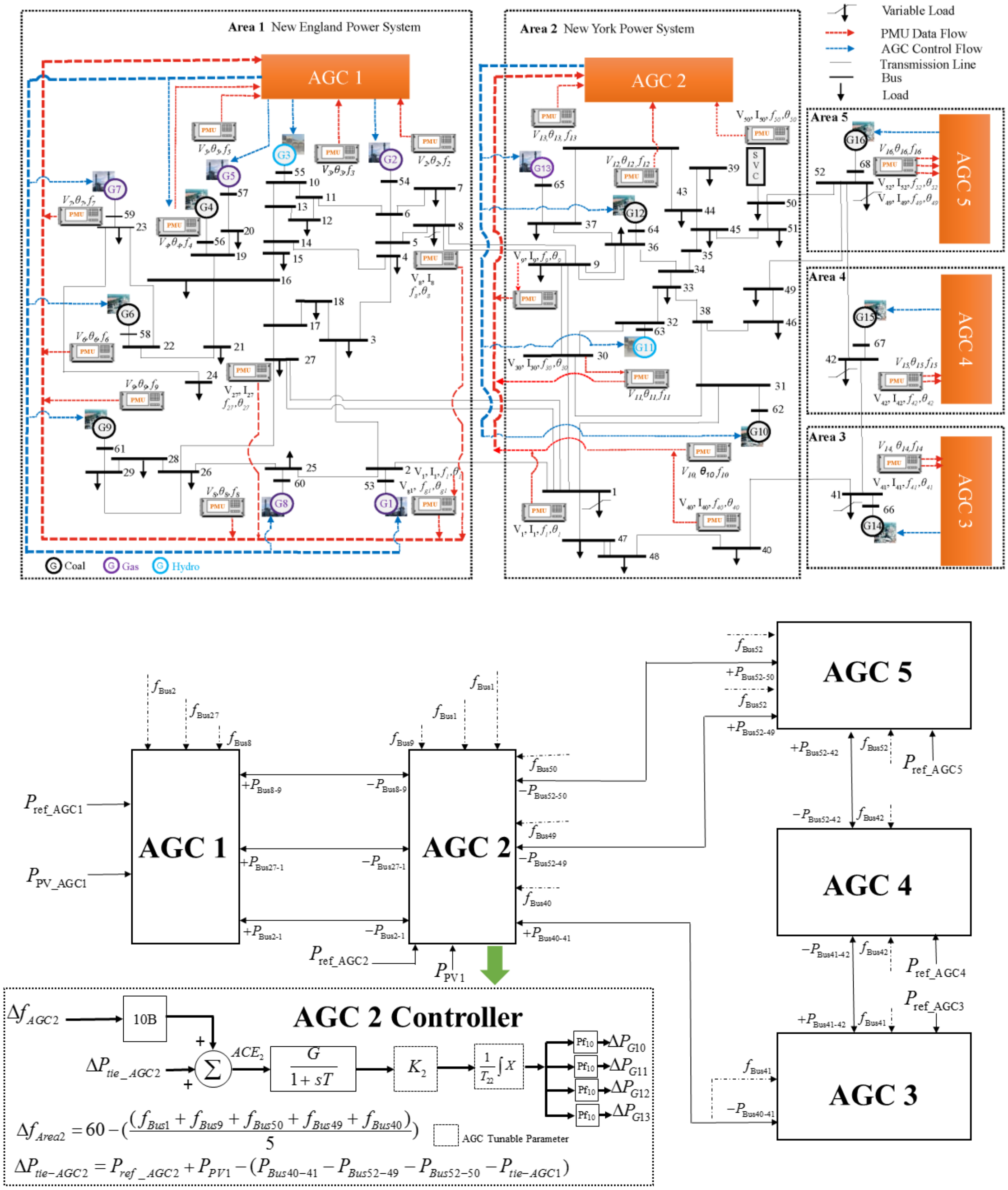

Figure 8.3 AGC 2 and AGC 1 for bilateral generation balancing.

When the velocity calculation completes, the new particle position is then as follows:

$$X_p^{k+1} = X_p^k + V_p^{k+1} \tag{8.4}$$

where X^k_p is the position of the p th particle for k th iteration. We next use a trial-and-error method to examine the parameters' upper and lower boundaries for tuning.

In the PSO circumstance, the cost function is a fitness evaluation function. Based on the general cost function expressed in (8.3), the PSO fitness evaluation, considering particle and position updates, is modified as follows:

$$\begin{aligned} &\min_{J_p^k} \quad J_p^k = \sum_{i=1}^{n} \sum_{T=t_0/\Delta t}^{t_2/\Delta t} |\, ACE_i(T) \,| \times (A \times \Delta t) \\ &s.t. \quad \rightarrow \forall p \in \mathbb{Z}^+, \, p = \{1,2,3...m\} \\ &\qquad\;\; \rightarrow \forall k \in \mathbb{Z}^+, k = \{1,2,3...m\} \\ &\qquad\;\; \rightarrow \forall n \in \mathbb{Z}^+, n = \{1,\ldots,s\} \end{aligned} \tag{8.5}$$

where p and k are the particle number and iterations of J.

As can be seen in (8.5), the total parameters for the five-area testbed are 10, as shown in Figure 8.6. Therefore, for (8.3) and (8.4), during the first and second step tuning, the X^k_p includes different parameter groups as (8.6) for the first-step and (8.7) for the second-step:

$$\begin{aligned} X_p^k(\gamma) = \{ &[K_1, T_{21}]_p^k, [K_2, T_{22}]_p^k, [K_3, T_{23}]_p^k \\ &, [K_4, T_{24}]_p^k, [K_5, T_{25}]_p^k \} \end{aligned} \tag{8.6}$$

$$\begin{aligned} &X_p^k(\gamma) = \{ [K_n, T_{2n}]_p^k \} \\ &s.t. \quad \rightarrow \forall n \in \mathbb{Z}^+, n = \{1,\ldots,s\} \end{aligned} \tag{8.7}$$

The multi-area AGC first and second-step tuning flowcharts are shown in Figure 8.4 and 8.5, respectively.

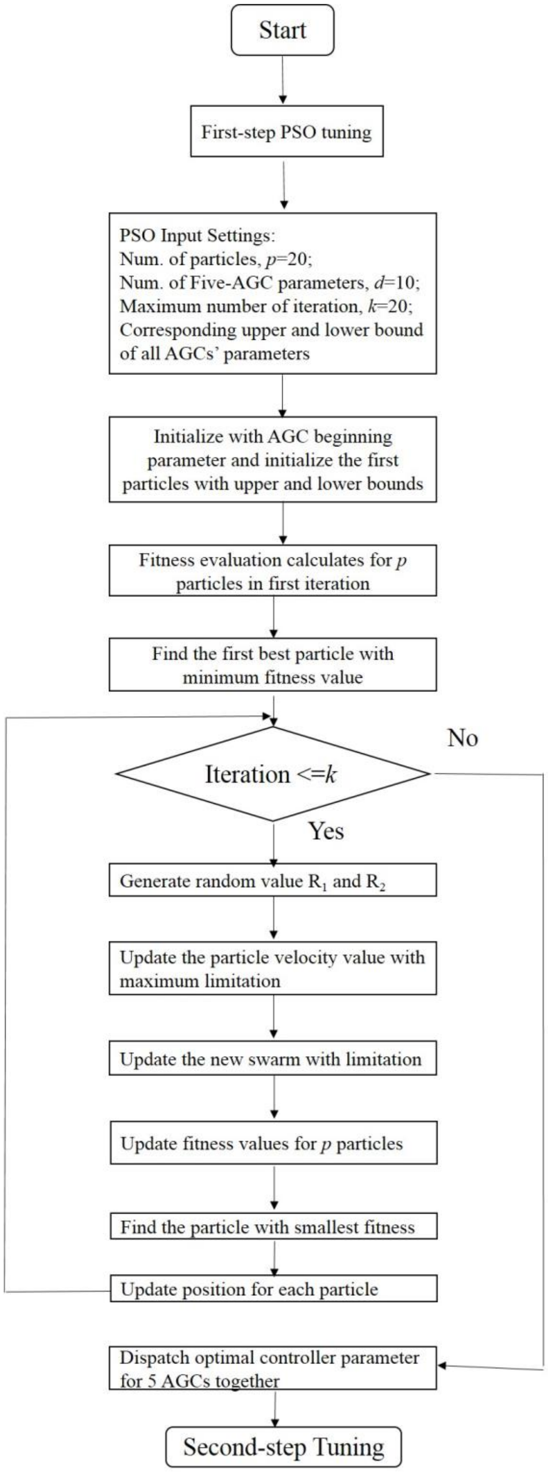

Figure 8.4 First-step tuning for 5 AGC controllers using the particle swarm optimization algorithm

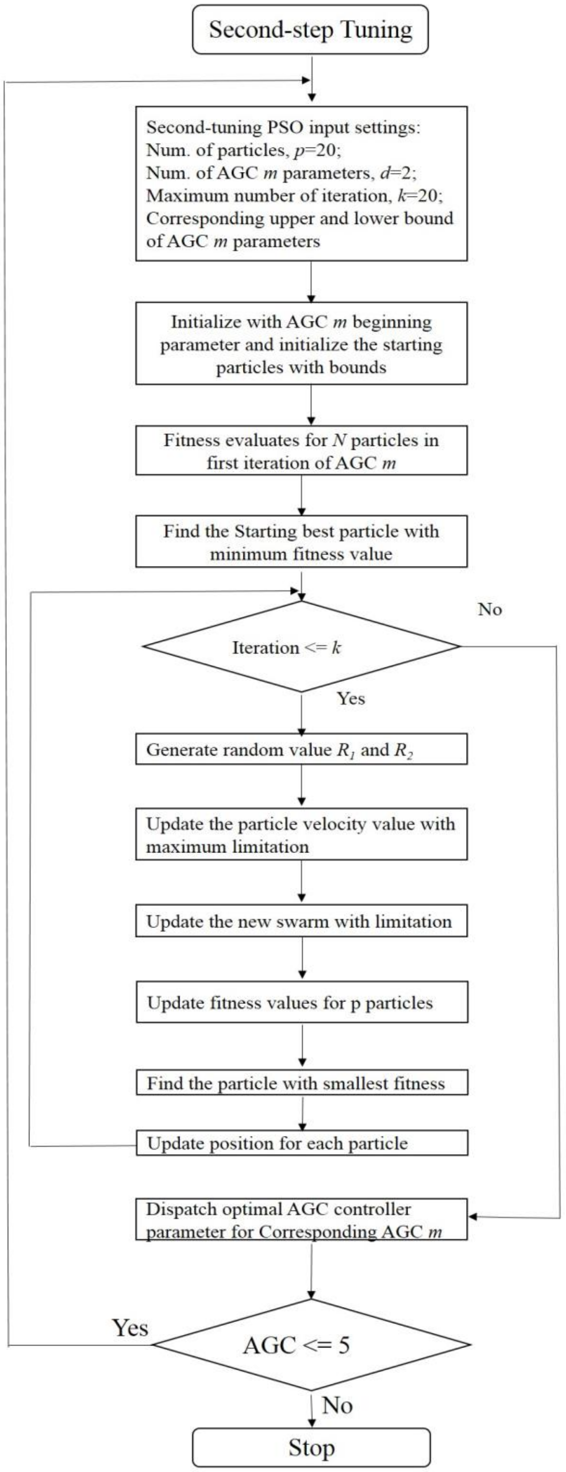

Figure 8.5 Second-step tuning for an individual AGC *m* controller using the particle swarm optimization algorithm.

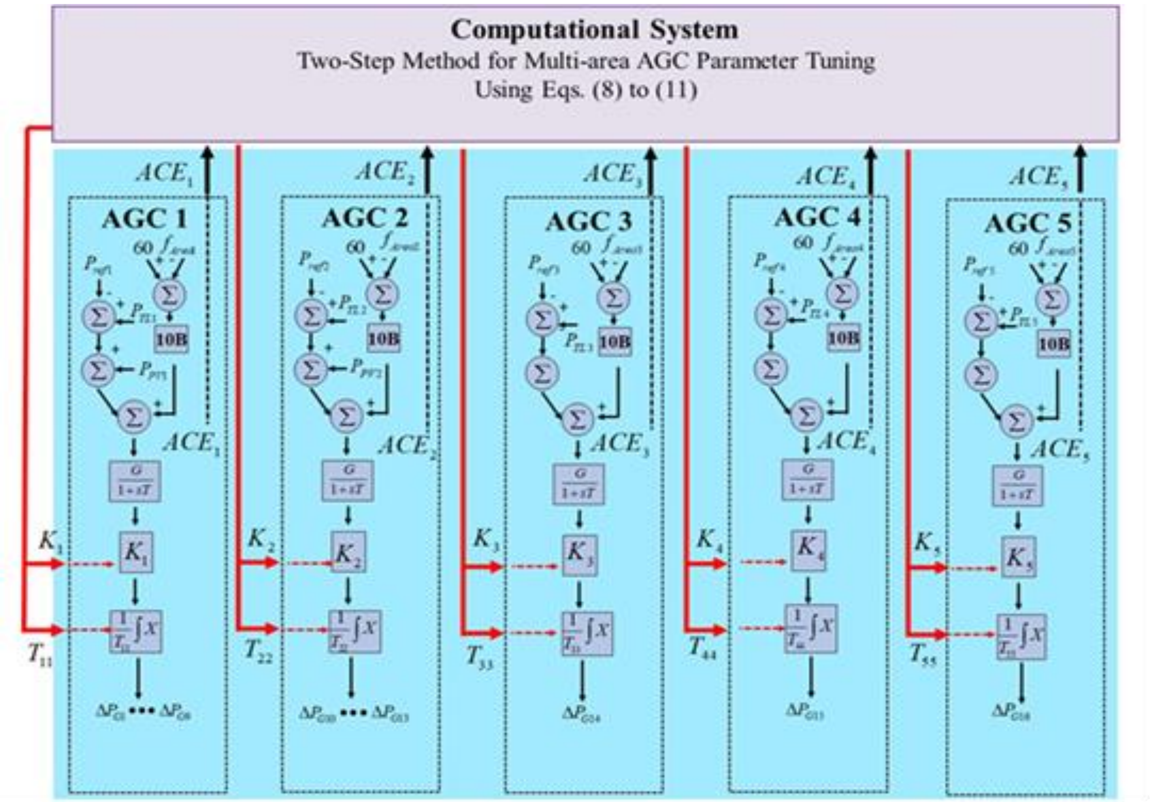

Figure 8.6 Distributed computational system for the Five-Area AGCs tuning.

8.4 Results and Discussions

Load disturbances were periodically applied to obtain the optimal parameters of AGCs in the five-area real-time testbed. Although there are five interconnected transmission lines among the entire system, only Areas 1 and 2 have utility-scale PV plants and multiple types of generators. In addition, Area 2 imports power from multiple areas under heavy load conditions; thus, a load disturbance occurring in this region indicates the least optimal situation for the testbed, which can be seen at Figure 3.3 in Chapter 3.

Therefore, a 400 MW step load change is applied at the tie-line Bus 1 (located at Area 2) with approximately 10% of Area 2 total on-site conventional generation values. MATLAB and via TCP/IP protocol is used to execute the tuning program to communicate with RSCAD software in RUNTIME. The distributed computational tuning system in Figure 8.6 was developed in the Clemson University Real-Time Power and Intelligent System (RTPIS) Laboratory. Both the first and second step tuning processes on the real-time mode have then verified the effectiveness of the method.

Thereafter, the asynchronous tuning method is applied for AGC 2 tuning in respective to AGC 1 for methodology validation. The load step change for the asynchronous tuning is 200 MW and PV plants in both Areas (Area 1 and 2) are set evenly as 150 MW for the initial test.

8.4.1. AGCs Performance with the Initial Settings

Case 1- Initial AGCs with generator base case settings:

The first case, as shown in Figure 8.5, entails a simulation with zero PV power for the testbed multi-area AGC testing. For a 250MW PV penetration, the tie-line power ACE for Area 2 presents the largest deviation during a 400MW load step change at tie-line Bus 1 (Figure 3.3, Chapter 3). For Area 2, 4, and 5, the overshoot values increase to 210MW, 315MW, and 180 MW with a subsequent settling time of 60 seconds, which is slower than the NERC CPS1 requirements [43-44].

8.4.2. Two-step Tuned AGCs Performance for Comparison

The two-step tuning method is applied to enhance the tuning of the multi-area AGC parameters with unified upper and lower boundaries in both first-step and second-step tuning process, which are [0.01 4] for *K*, [0 3] for T_2, and 0.1 for *V* maximum or minimum searching step. A 400MW step-load change disturbance at Bus 1 is used for both the first-step and second-step tuning to compare the enhanced AGC performance, followed by the use of various PV penetration levels to examine the performance of the two-step tuned controllers.

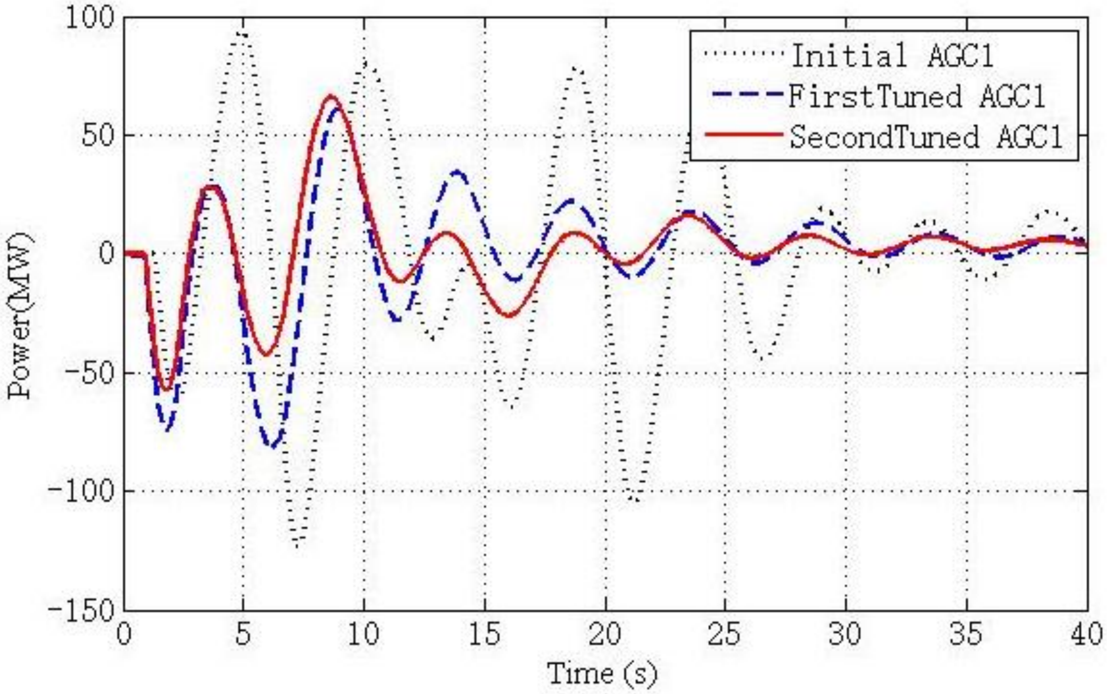

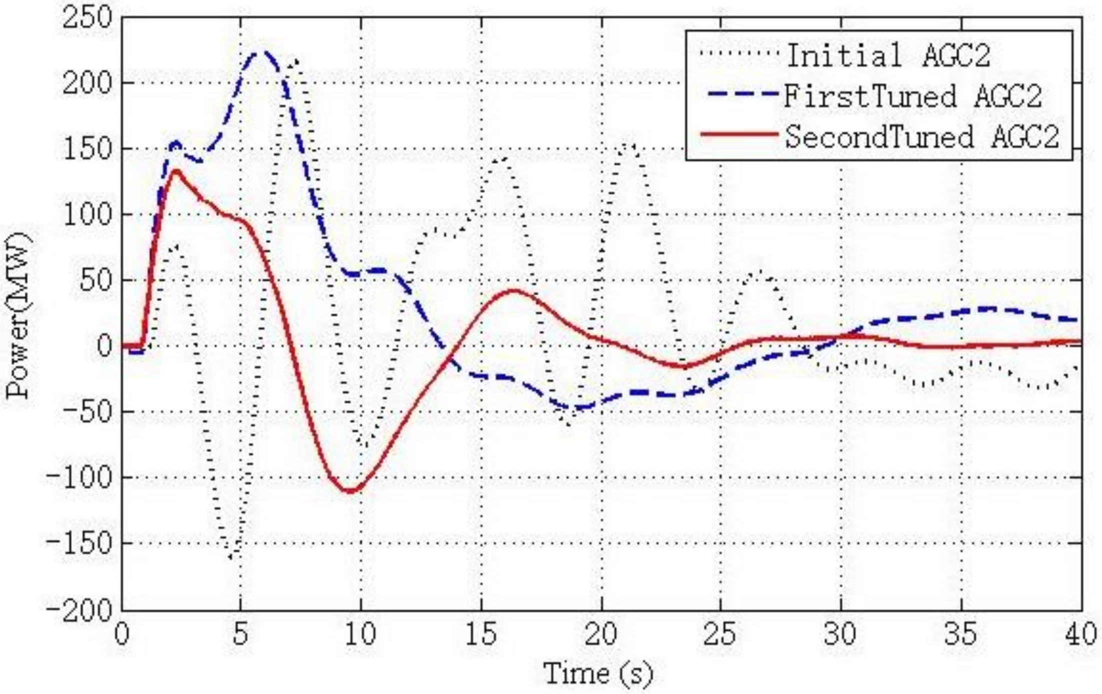
Initial AGC2
FirstTuned AGC2
SecondTuned AGC2
Power(MW)
Time (s)
250
200
150
100
50
0
-50
-100
-150
-200
0
5
10
15
20
25
30
35
40

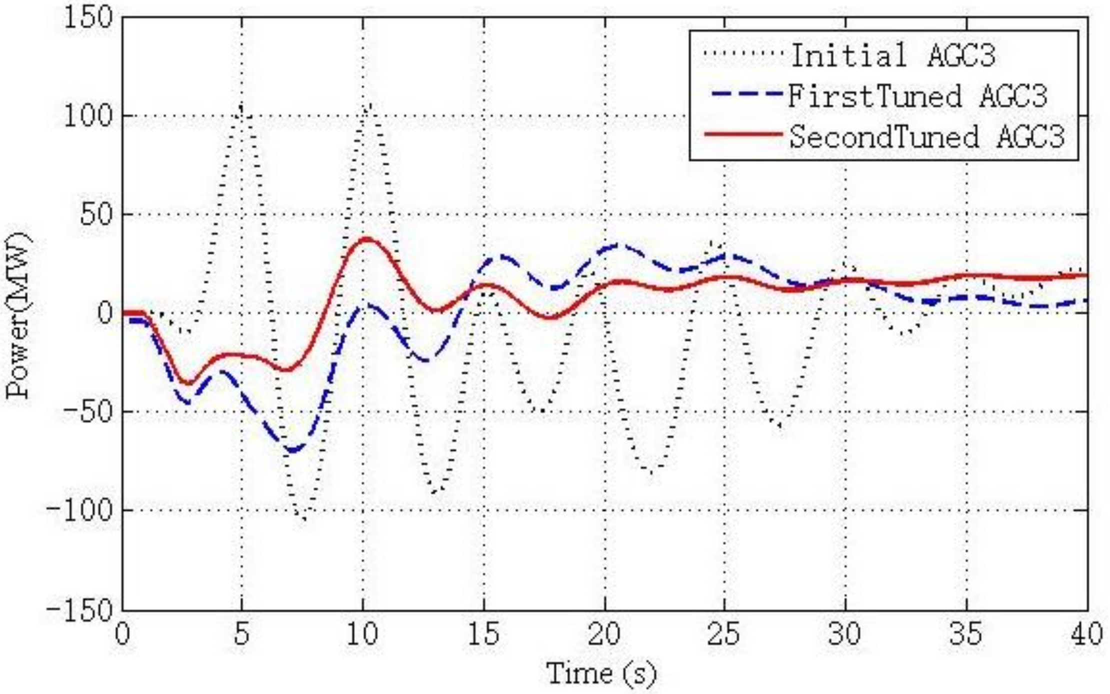
Initial AGC3
FirstTuned AGC3
SecondTuned AGC3
Power(MW)
Time (s)
150
100
50
0
-50
-100
-150
0
5
10
15
20
25
30
35
40

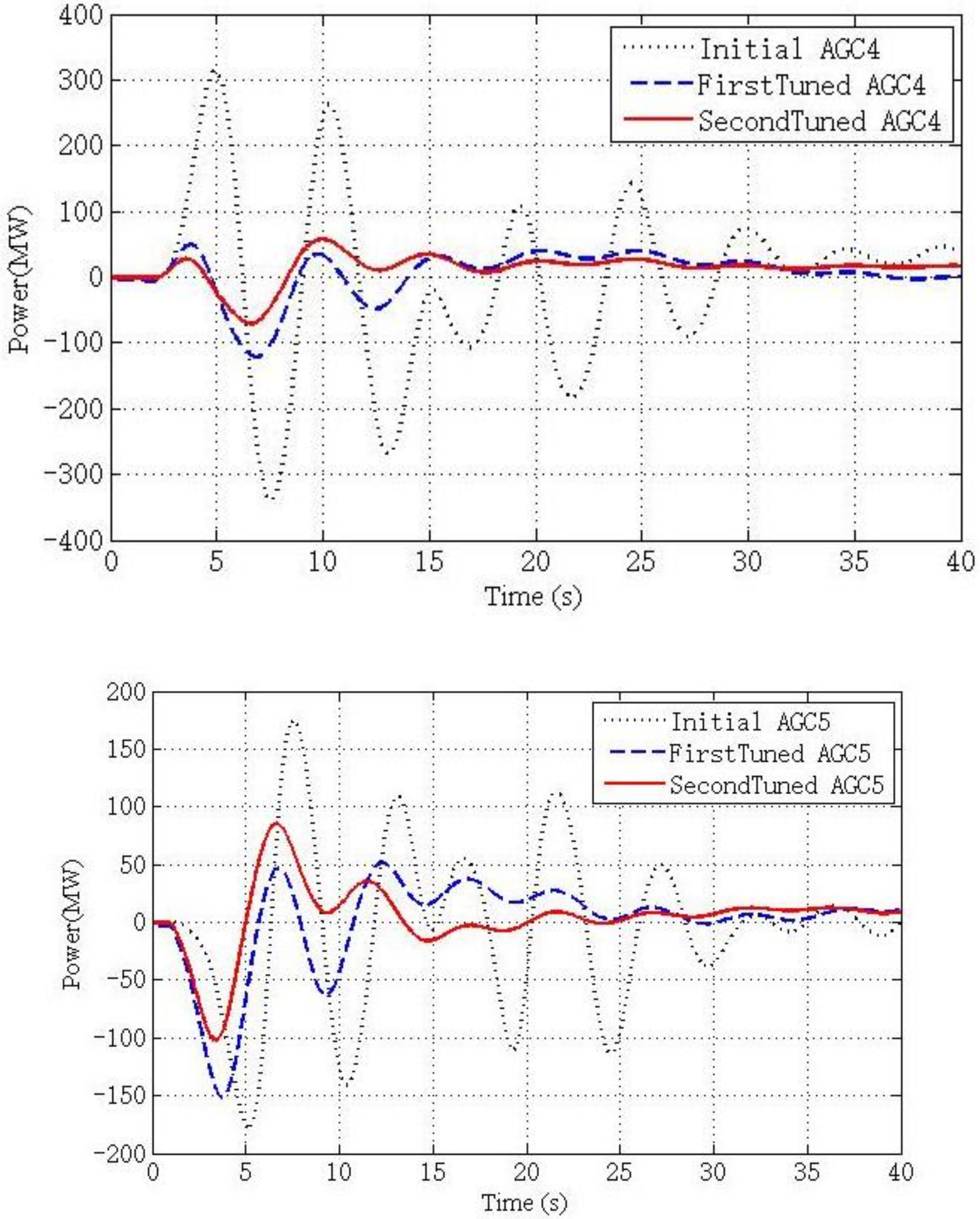

Figure 8.7 ACE response based on first and second step tuned AGCs at Bus 1, a 400MW load change with 500 MW PV penetration in Areas 1 and 2 and for Area 1-5 above.

Case 2- AGC parameters comparison for initial, first-step and second-step tuned:

Here the two-step method is used to tune the AGCs with both the PV penetration (250 MW for both regions) and a 400MW step load change at tie-line Bus 1. The maximum overshoot and settling time comparisons for the initial, first-step tuned, and second-step tuned parameters are shown in Table 8.1 and comparison plots for the same load changes at tie-line Bus 1 are shown in Figure 8.5, with all five-area AGCs. As shown in Figure 8.5, the dotted lines represent the initial settings, the dashed lines in blue represent the first-step tuning, and solid red lines represent the second-step results.

The two-step method refined parameters are provided in Table 8.2. As the data in Table 8.1 and Figure 8.5 indicate, the two-step tuned AGCs exhibited the optimal performance among all three types of parameters. Especially, when compared to the initial AGC in Area 2, the settling time decreased from 60 seconds to 25 seconds and the maximum overshoot was reduced from 210 MW to 132 MW, with a 37% rate of improvement, denoting a more stable AGC performance during a severe step-load disturbance.

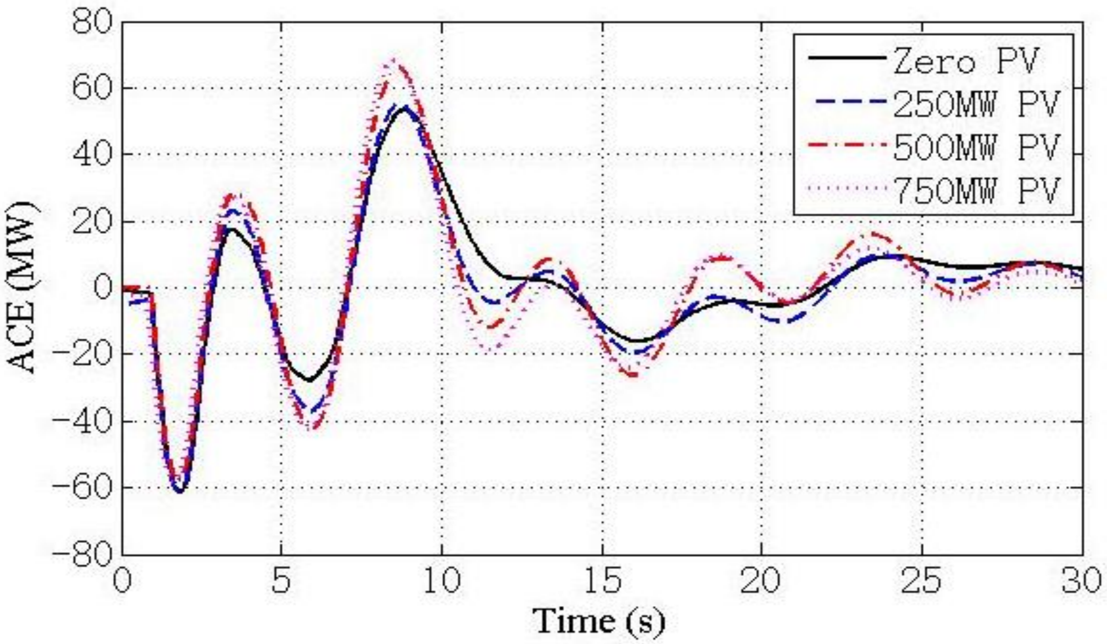
ACE (MW)
80
60
40
20
0
−20
−40
−60
−80
0
5
10
15
20
25
30
Time (s)
Zero PV
250MW PV
500MW PV
750MW PV

(a)

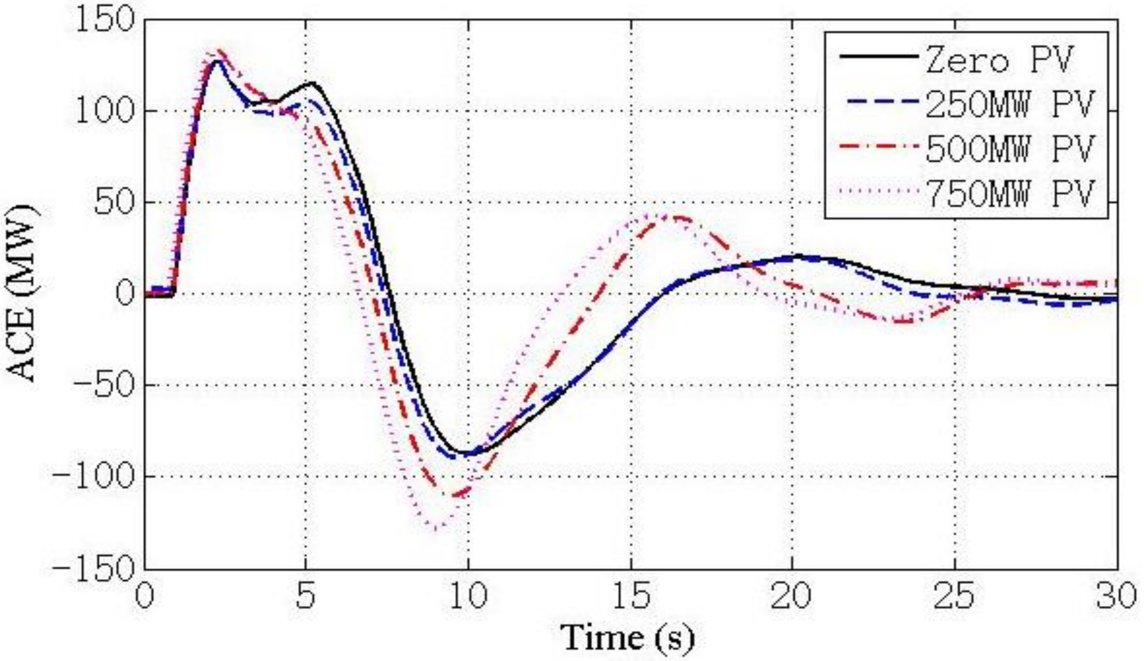
ACE (MW)
150
100
50
0
−50
−100
−150
0
5
10
15
20
25
30
Time (s)
Zero PV
250MW PV
500MW PV
750MW PV

(b)

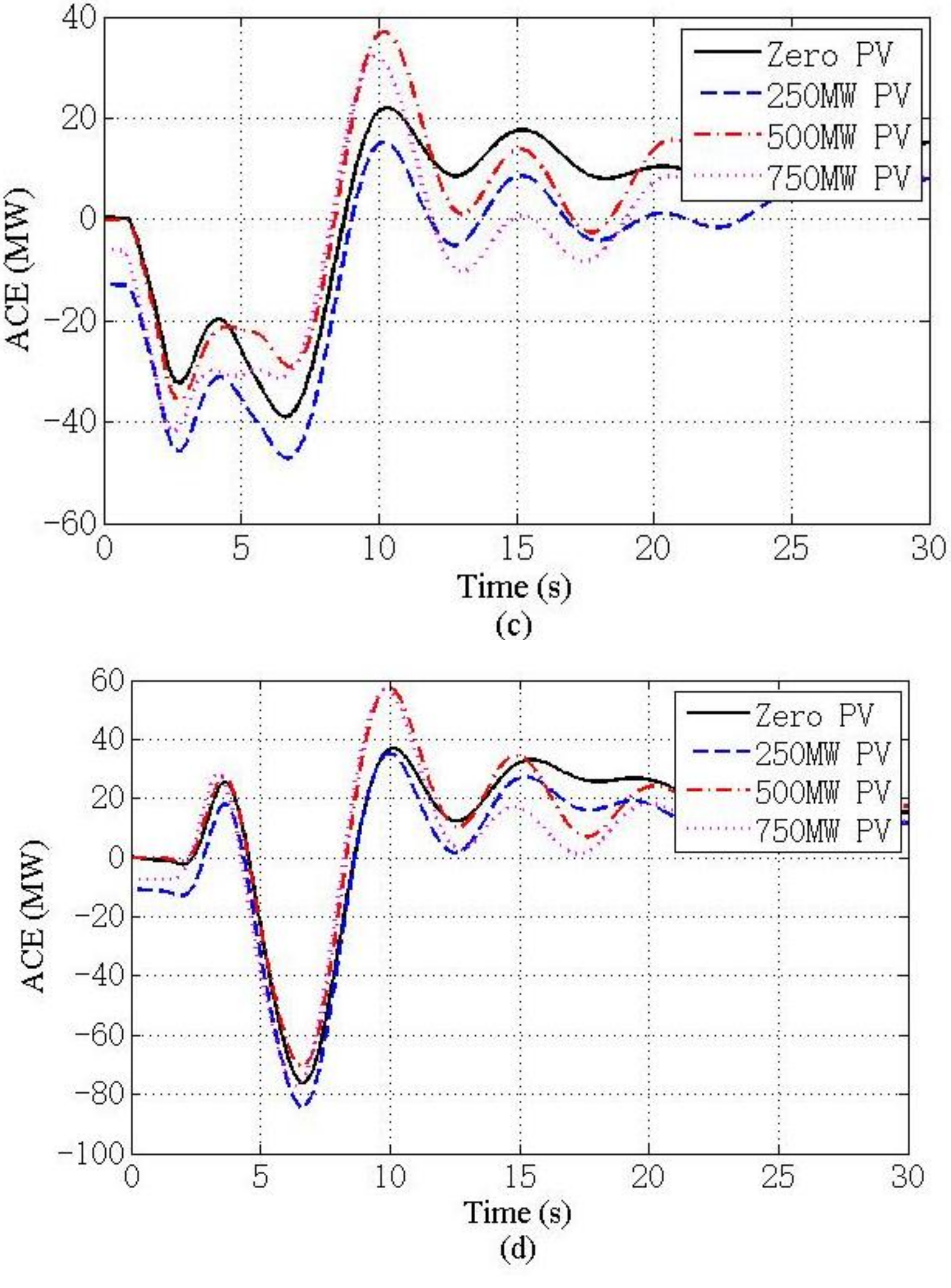
ACE (MW)
Time (s)
Zero PV
250MW PV
500MW PV
750MW PV
40
20
0
-20
-40
-60
0
5
10
15
20
25
30
(c)
ACE (MW)
Time (s)
Zero PV
250MW PV
500MW PV
750MW PV
60
40
20
0
-20
-40
-60
-80
-100
0
5
10
15
20
25
30
(d)

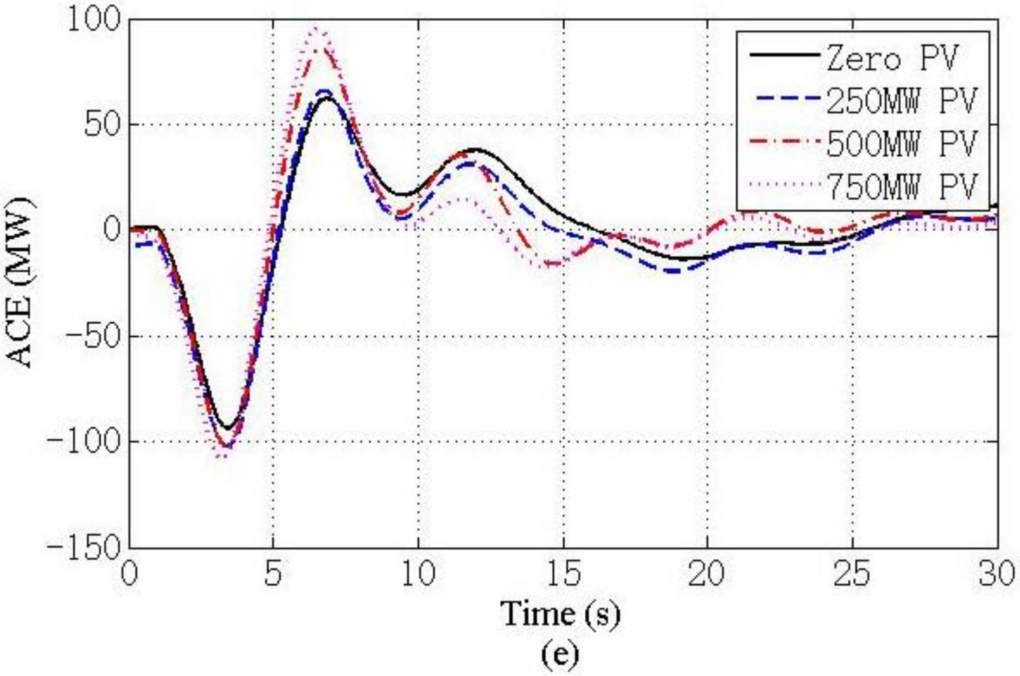

Figure 8.8 Two-step tuned AGCs responses for Zero, 250MW, 500MW, and 750MW PV penetration on Areas 1 and 2, altogether with a 400MW load change at tie-line Bus 1: (a) Area 1; (b) Area 2; (c) Area 3; (d) Area 4; (e) Area 5.

Case 3- AGC controller performance validation with two-step tuned parameters

To further examine the AGCs enhanced by the two-step method, the following PV penetration levels were applied for Areas 1 and 2 (i.e. zero, 250 MW, 500 MW, and 750 MW) with the same load disturbance (i.e. the 400 MW step load change at Bus 1) AGCs were used to adjust the operational conditions of the generation to absorb PV power. The generation conditions of these four case studies are in Table 8.3 with the performances plotted and presented in Figure 8.6 for all regions. For the maximum PV integration scenario (750 MW PV 1 in Area 1 and 700 MW PV 2 in Area 2), an on-site value of 4735 MW encompasses the total generation in Area 1, and an on-site value of 5774 MW encompasses Area 2.

Therefore, the peak PV power penetration is 15.42% (Area 1) and 12.12% (Area 2) of the total power in their corresponding region

As the results of maximum overshoot and the settling time in Table 4 show, the two-step tuned AGCs exhibit enhanced performance for the continuously increasing level of PV penetration as compared to the base case.

Case 4- Multi-area AGC performance validation with both real-time PV mitigation and load disturbance

Here, a dynamic PV power penetration using real-time weather information is used to examine and compare the two-step enhanced AGCs with the initial AGCs through a 300-second simulation time. As can be seen in Figure 8.7a, three major PV power fluctuations occurred.

The first enhanced the PV from 300 MW up to 650 MW from (t+12) s to (t+90)s, and the second enhanced the PV from 400 MW upto 580 MW from (t+100) s to (t+120) s. As shown in Figure 8.7, during those instances of sharp increases, the two-step tuned AGCs reduced the ACE fluctuation substantially in all regions with respect to the maximum overshoots and settling times. For the first PV fluctuation, the largest ACEs captured by tuned and initial AGC1 is 148 MW and 220 MW, with a 72 MW, or 32.2% reduction. Similarly, the situation reoccurred during scenarios two and three with a forward oscillation of PV power from 400 MW to 650 MW and a reverse from 650 MW to 280 MW.

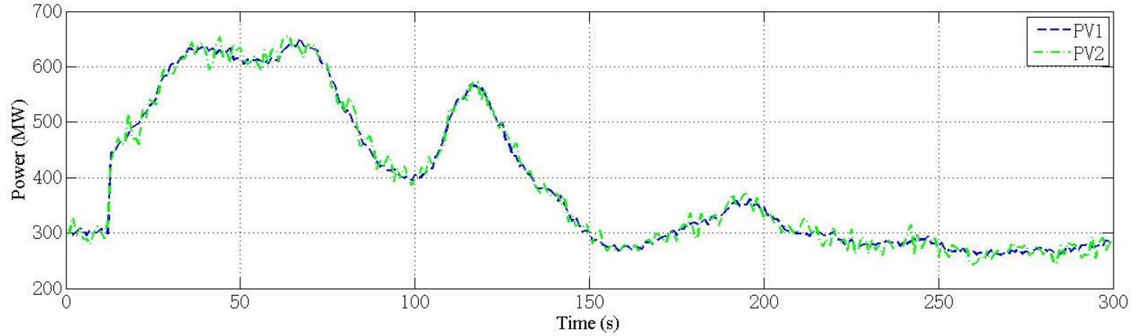
PV1
PV2
Power (MW)
700
600
500
400
300
200
0
50
100
150
200
250
300
Time (s)

(a)

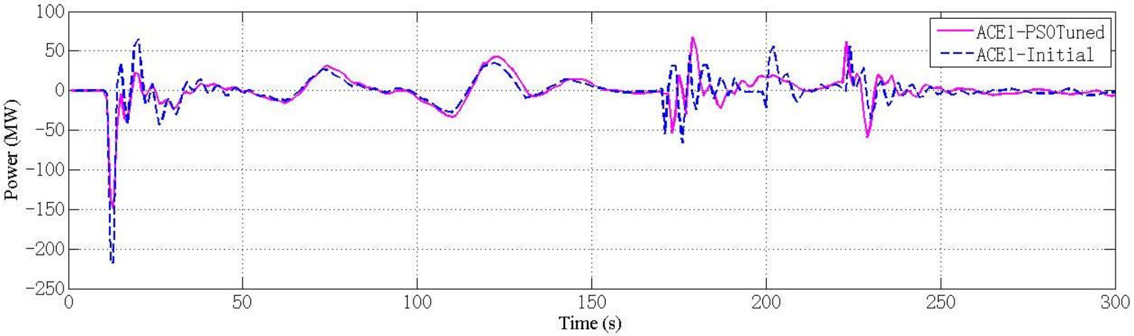
ACE1-PSOTuned
ACE1-Initial
Power (MW)
100
50
0
−50
−100
−150
−200
−250
0
50
100
150
200
250
300
Time (s)

(b)

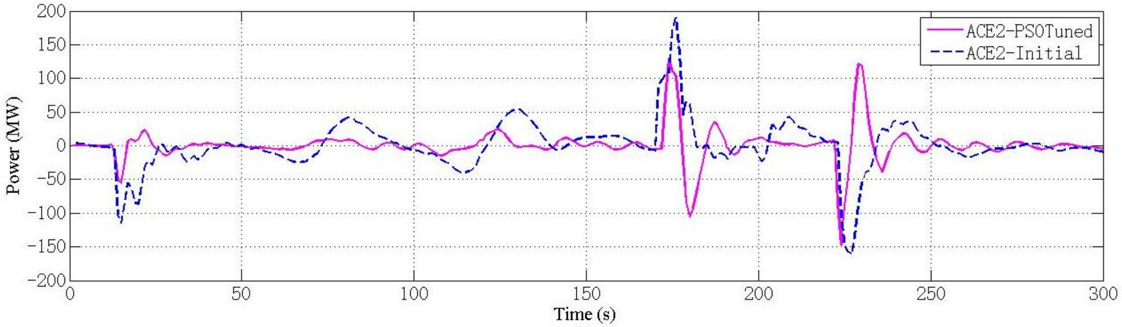
ACE2-PSOTuned
ACE2-Initial
Power (MW)
200
150
100
50
0
−50
−100
−150
−200
0
50
100
150
200
250
300
Time (s)

(c)

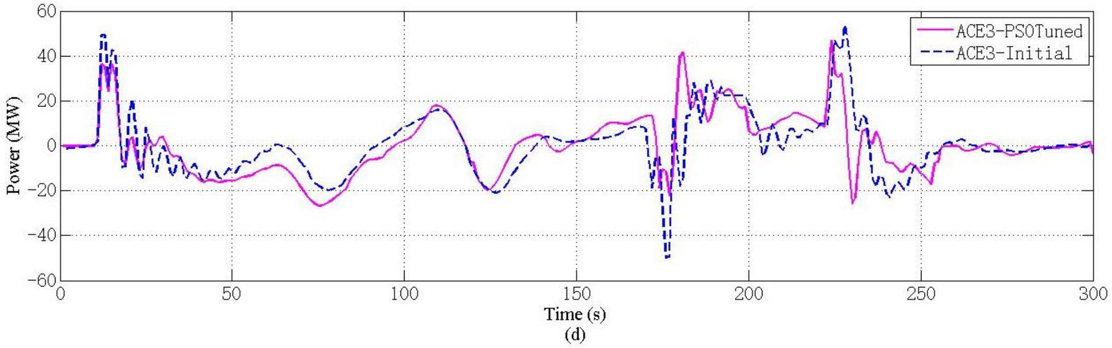
ACE3-PSOTuned
ACE3-Initial
Power (MW)
60
40
20
0
-20
-40
-60
0
50
100
150
200
250
300
Time (s)

(d)

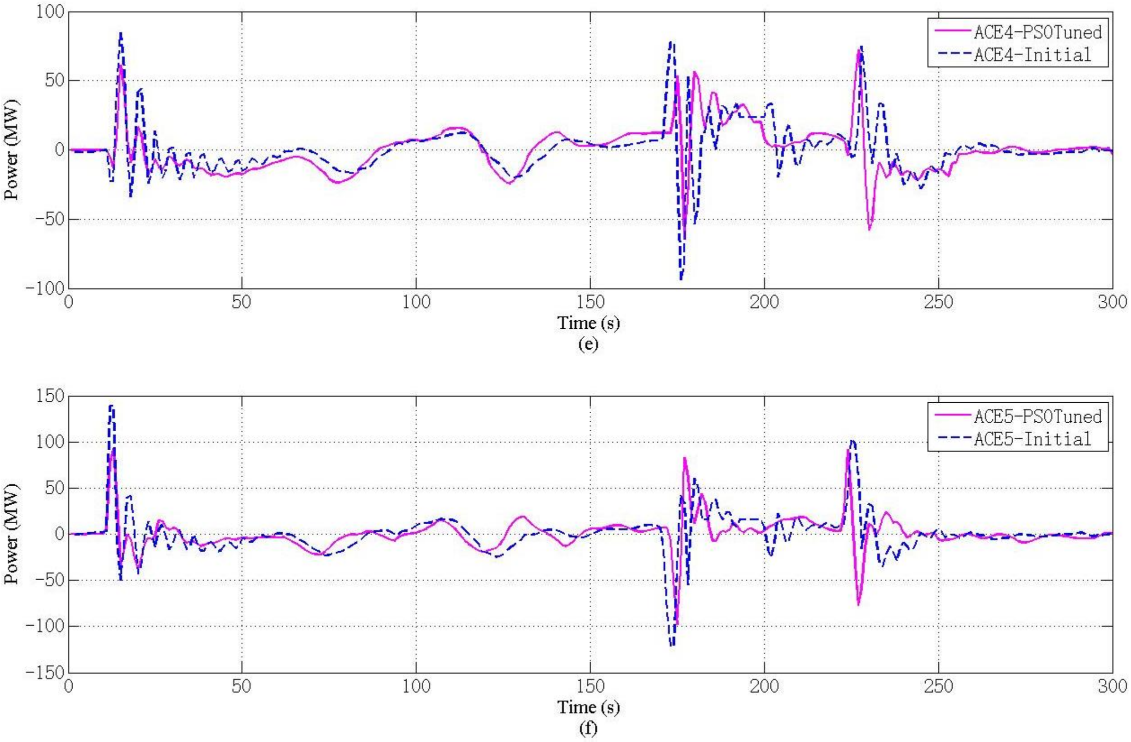

Figure 8.9 Utility-scale PV dynamic penetration for the initial AGC and the two-step tuned AGCs: (a) dynamic PV power oscillation; (b) five ACEs for Area 1; (c) five ACEs for Area 2; (d) five ACEs for Area 3; (e) five ACEs for Area 4; (f) five ACEs for Area 5.

In addition to the natural fluctuations, a forced disturbance was also applied to evaluate the two-step tuned AGCs. In this dynamic PV power penetration test, a 400 MW step load change at tie-line Bus 1 was applied concurrently at (t+170) s.

The AGC performance in a dynamic situation was determined using the Transient Energy (T.E.) and corresponding Performance Improvement formulations (8.8), as summarized in Table 8.5.

$$
\begin{aligned}
&T.E._{i} = \int_{t+start}^{t+end} |P_i(t)|\,dt \cong \sum_{T=t+start/\Delta t}^{t+end/\Delta t} |P_i(T)| \times \Delta t \\
&s.t. \quad \to \forall i \in \mathbb{Z}^{+}, i = \{1,2,3,4,5\}
\end{aligned}
\tag{8.8}
$$

During an established timeframe AGCs both maintained within a small range or quickly restored as necessary the system to normal operation during any disturbance, ensuring a stable and reliable performance of the tuned AGCs. A stable and reliable performance of the tuned AGCs was the result. The case studies further illustrate the effectiveness of the two-step method for multi-area power system AGC tuning, in which a multi-area power system with five interconnected areas was used to analyze and validate the utility-scale PV power penetration.

Although PI control schemes have been used to manage automatic generation control (AGC) power systems for over a century, the limitations of power plants installed in a particular year prevented any consideration of renewable energies [45-46]. However, the rapid commercialization of renewables has now made possible the commercialization utility-scale PVs for use in of AGCs. Further, the mitigation of energy loss from poorly tuned AGCs, as shown in case 4, delivered optimal performances on both ACEs with transient energy savings. Results from this two-step tuning method ensured that the system determined an optimal set for managing the PV penetration problem and severe step load disturbance.

Table 8.1 Performance Analysis for Case 2

AGCs	Maximum Overshoot (MW)			Settling Time (s)		
	A	B	C	A	B	C
AGC1	130	78	66	60	35	25
AGC2	210	210	132	60	35	25
AGC3	100	76	32	60	35	25
AGC4	315	120	76	60	35	25
AGC5	180	150	85	60	35	25

A, B, and C refer to AGC initial, the first step tuned, and the second step tuned parameters.

Table 8.2 Initial, First, and Second Tuned Parameters for Five-area AGCs

Area	**Tuning Conditions**	**Five-Area AGC Tie-line Bias Controller Parameters**	
		K	***T*₂**
Area 1	Initial values	0.1000	0.2500
	First-step Tuned	1.0718	2.0102
	Second-step Tuned	0.2675	0.7346
Area 2	Initial values	0.1000	0.2500
	First-step Tuned	3.4161	1.4140
	Second-step Tuned	1.2788	0.6161
Area 3	Initial values	0.1000	0.2500
	First-step Tuned	1.0000	2.4437
	Second-step Tuned	0.4582	1.2170
Area 4	Initial values	0.1000	0.2500
	First-step Tuned	0.3917	0.6439
	Second-step Tuned	0.4840	2.0268
Area 5	Initial values	0.1000	0.2500
	First-step Tuned	0.3418	1.2031
	Second-step Tuned	0.3081	1.5986

Two-step tuned parameters are round to 4 decimal numbers, however, the actual parameters processed by RSCAD are up to 16 decimal numbers.

Table 8.3 Initial, First, and Second Tuned Parameters for Five-area AGCs

Gen	**Base Case (MW)**	**Reactive Power (MVAr)**	**Volt (p.u.)**	**PV1 250 PV2 250 (MW)**	**Reactive Power (MVAr)**	**Volt (p.u.)**	**PV1 500 PV2 500 (MW)**	**Reactive Power (MVAr)**	**Volt (p.u.)**	**PV1 750 PV2 700 (MW)**	**Reactive Power (MVAr)**	**Volt (p.u.)**
G1	250	34	1.0010	250	15	1.0010	252	1.96	1.0010	263	-3	1.0010
G2	562	136	0.9818	539	125	0.9842	514	117	0.9858	487	116	0.9872
G3	630	171	0.9869	588	155	0.9891	543	144	0.9916	490	143	0.9934
G4	663	149	0.9952	646	131	0.9988	631	116	1.0000	614	115	1.0010
G5	520	179	1.009	499	177	1.0150	478	178	1.0200	454	180	1.0220
G6	711	206	1.019	690	199	1.0260	671	196	1.0310	600	198	1.0330
G7	572	60	1.020	552	39	1.0220	531	24	1.0240	500	19	1.0250
G8	661	-7	0.9947	642	-15	0.9963	622	-19	0.9977	600	-20	0.9991
G9	811	36	1.011	791	23	1.0120	771	13	1.0130	727	8	1.0130
G10	617	80	0.9979	562	62	0.9991	515	52	0.9999	486	53	1.0000
G11	1422	197	0.9872	1378	181	0.9908	1212	162	0.9929	1109	156	0.9944
G12	1620	320	0.9958	1493	320	1.0130	1387	324	0.9980	1319	343	0.9985
G13	3019	1234	1.0130	2922	1228	1.0010	2837	1228	1.0130	2860	1247	1.0130
G14	5786	783	1.0010	5787	775	1.0010	5781	763	1.0010	5791	761	1.0010
G15	6088	774	1.0010	6084	774	1.0010	6175	772	1.0010	6167	771	1.0010
G16	5465	1168	1.0010	5468	1174	1.0010	5502	1168	1.0010	5499	1185	1.0010

Table 8.4 Performance Analysis for Case 3

AGCs	Maximum Overshoot (MW)				Settling Time (s)			
	Zero PV	250 MW PV	500 MW PV	750 MW PV	Zero PV	250 MW PV	500 MW PV	750 MW PV
AGC1	123	125	126	129	25	25	25	25
AGC2	199	203	203	204	25	25	25	25
AGC3	52	52	53	53	25	25	25	25
AGC4	65	68	68	69	25	25	25	25
AGC5	112	113	113	115	25	25	25	25

Table 8. 5 Transient Energy for Case 4 with the Initial and Two-step Tuned AGC.

Dynamic Time Period (t+k s)	**AGCs**	**Initial T.E (MWsec)**	**Two-Step Tuned T.E (MWsec)**	**ΔT.E (MWsec)**	**P.I.**
t+12 to t+90 (PV Sudden Change)	AGC1	127.6	107.3	20.3	15.9%
	AGC2	172.1	52.4	19.6	69.5%
	AGC3	107.8	90.7	17.1	18.8%
	AGC4	105.1	100.8	4.3	4.3%
	AGC5	108.3	83.2	25.1	23.2%
t+170 to t+220 (400 MW Step Load Increase)	AGC1	76.2	63.5	12.7	16.7%
	AGC2	169.7	120.0	49.7	29.3%
	AGC3	79.1	73.8	5.3	7.2%
	AGC4	119.3	98.4	20.8	17.5%
	AGC5	120.3	83.6	36.7	30.5%
t+220 to t+300 (400 MW Step Load Decrease)	AGC1	55.2	44.8	10.4	23.2%
	AGC2	166.7	122.9	43.8	26.3%
	AGC3	68.2	52.3	15.8	23.2%
	AGC4	66.8	77.5	10.7	16.0%
	AGC5	76.5	65.7	10.8	14.1%

8.4.3. Asynchronous Tuned AGCs Performance for Comparison

AGC 2 parameter through asynchronous tuning were compared with previous initial values, synchronous tuned values, manual tuned values, which is listed in Table 8.6. Note that the manual tuning is based on the synchronous tuned (two-step method) parameters but with multiple trial and error tests. Thereafter, the performance comparison between these three tuning methods was listed in Table 8.7.

Table 8.6 Asynchronous, synchronous, manual tuned and initial value comparison

Area	***Tuning Method***	***K***	***T***
Area 2 AGC 2	Initial values (I.T.)	0.1	0.25
	Synchronous Tuned (S.T.)	1.2788	0.6161
	Manual Tuned (M.T.)	3.46	1.49
	Asynchronous Tuned (A.T.)	3.3909	1.4708

Table 8.7 Performance comparison for Asynchronous tuned, manual tuned and synchronous tuned AGC 2

AGC 2	**Maximum Overshoot**			**Settling Time (s)**		
	S.T.	***M.T.***	***A.T.***	***S.T.***	***M.T.***	***A.T.***
ACE	82 MW	83MW	80 MW	30	33	27
Tie-line Power	343 MW	342 MW	346 MW	30	34	27
Frequency	59.958 Hz	59.921 Hz	59.965 Hz	32	45	30

The results for ACE, frequency, and tie-line power response under the aforementioned tuned parameters are shown in Figures 8.10 - 8.13, respectively.

The results present that the asynchronous tuned parameters achieve a superior performance for tie-line power and frequency in between Area 1 and 2. The frequency maximum overshoots response demonstrate a higher value during load change, which is more secure. Thereafter, A 100 MW PV power-up is applied at Area 1 and transfer to Area 2.

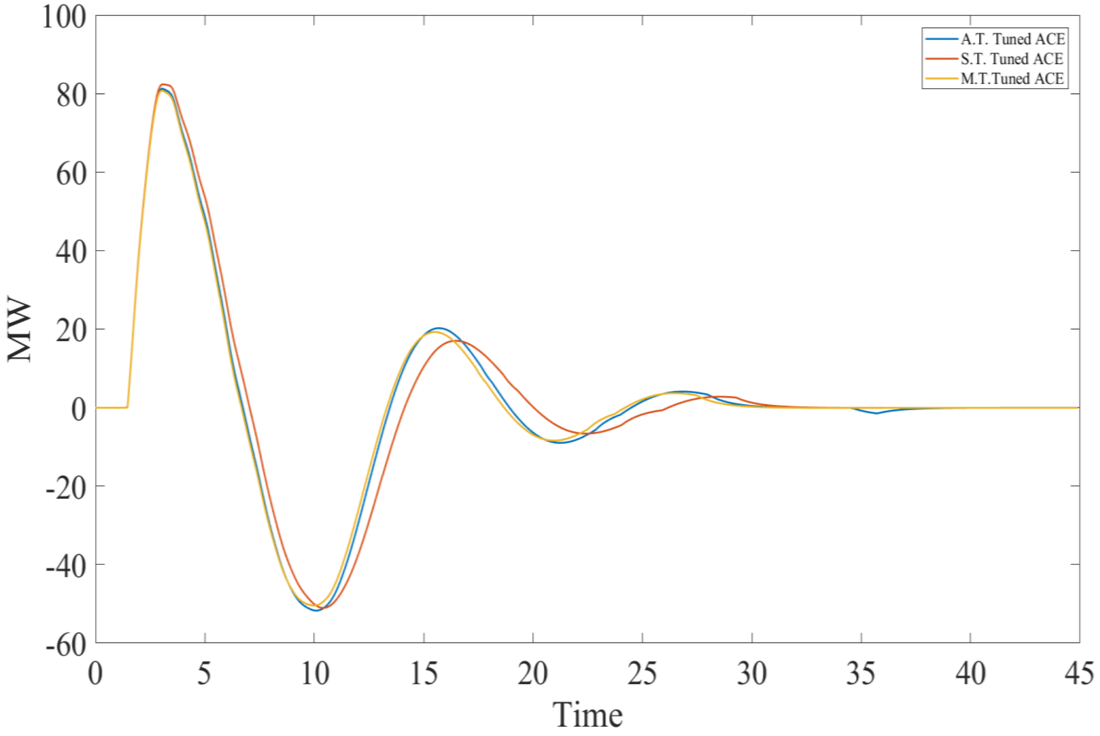

Figure 8.10 ACE response for asynchronous tuned (A.T.), synchronous tuned (S.T.) and manual tuned (M.T.) comparison.

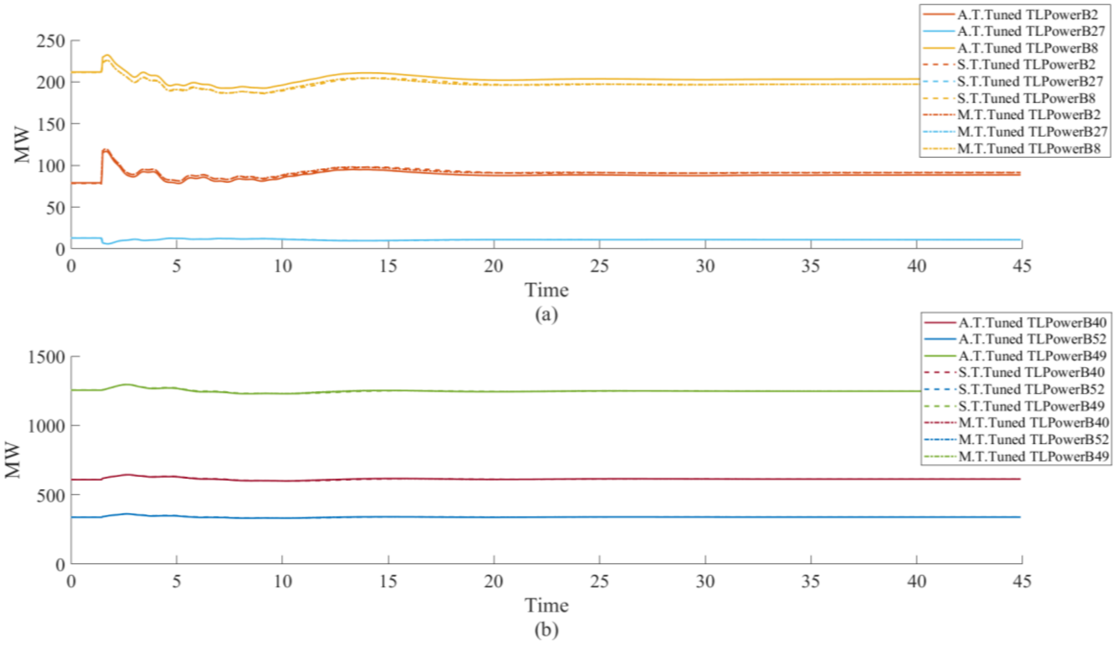

(a)

(b)

Figure 8.11 Power response for asynchronous tuned (A.T.), synchronous tuned (S.T.) and manual tuned (M.T.) comparison.

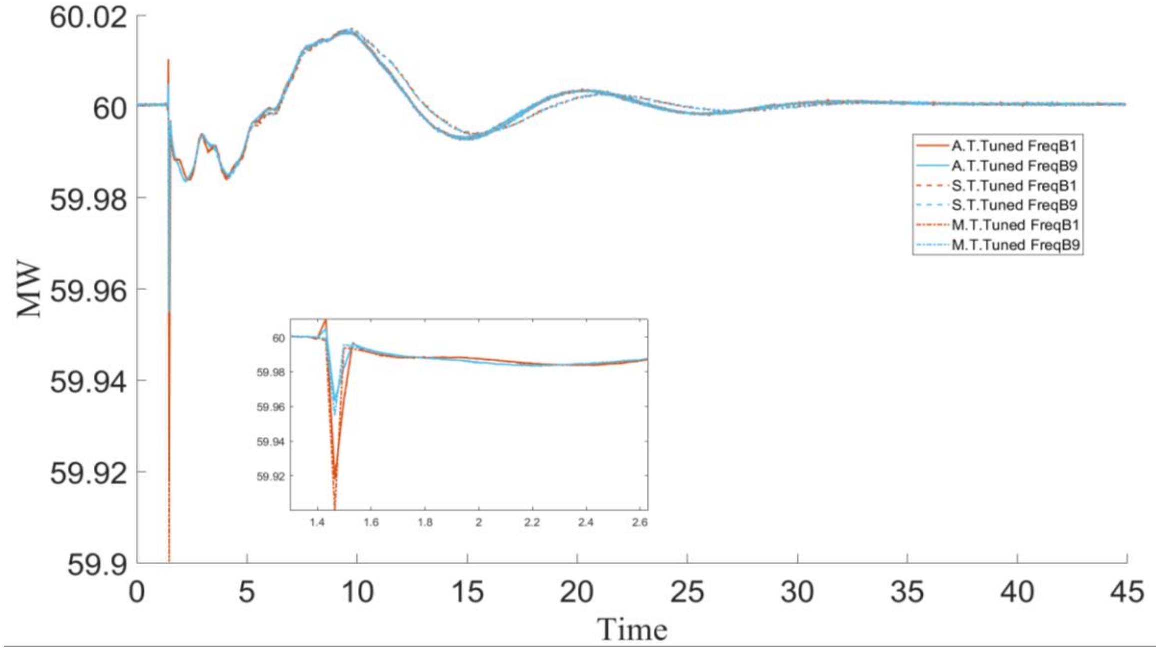

Figure 8.12 Frequency response for asynchronous tuned (A.T.), synchronous tuned (S.T.) and manual tuned (M.T.) comparison.

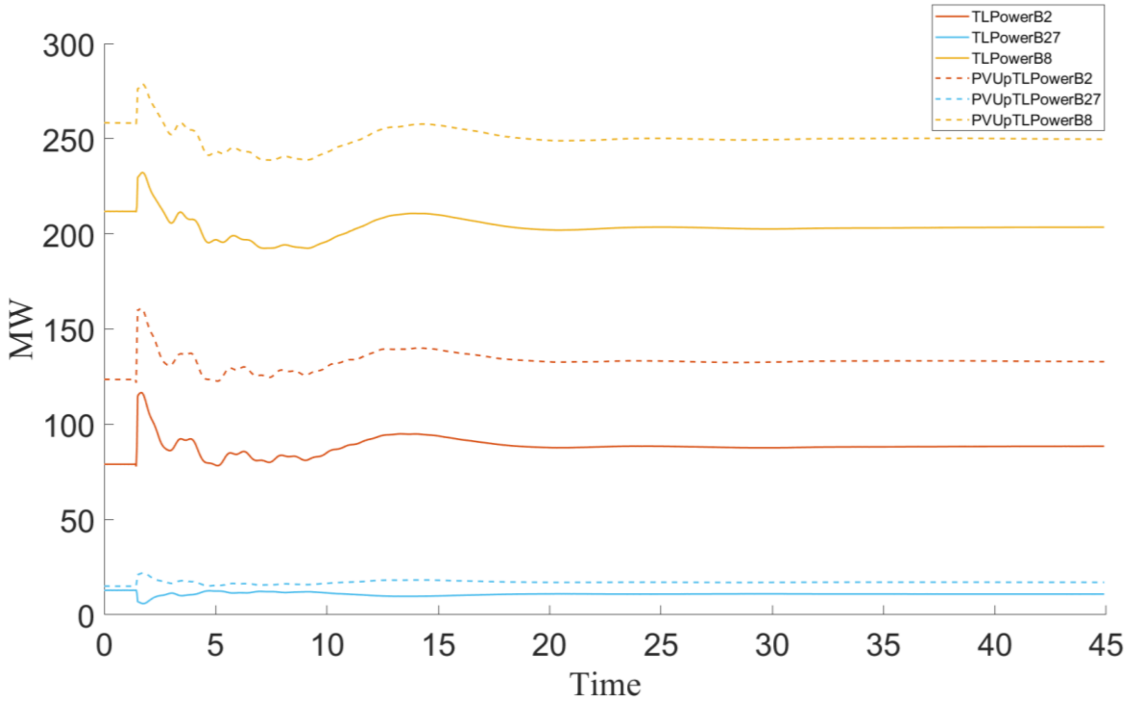

Figure 8.13 Tie-line power response for asynchronous tuned (A.T.) AGC with a 100MW PV power increasing in Area 1.

8.5 Summary

This chapter developed a two-step tuning and an asynchronous tuning for use in multiple AGC parameters in an interconnected multi-source multi-area power system with utility-scale PV. Results of the real-time simulations of the five-area 70-bus power system determined that the two-step tuning method with PSO optimization algorithm did indeed enhance the AGC performances characterized by high levels of variability and uncertain renewable energy sources (e.g. solar PVs). Furthermore, the asynchronous tuning results indicated that the AGC performance can be specifically improved for bilateral or trilateral areas generation balancing.

CHAPTER 9

CONCLUSION

9.1 Overview

Power system operation center maintains the electric grid in a steady 60 Hz frequency and a balanced generation-load situation even under severe disturbances. However, conventional operation with the SCADA system is facing a great challenge as mitigating the increased penetration level of PV power in any situation. Thus, a distributed, data-oriented, and scalable intelligence structure is needed for improving the operation center situational intelligence. Cellular computational network based frequency prediction algorithms are implemented, which is suitable for PMU measurements integration.

9.2 Research Study Summary

In the first part of this dissertation, three IEEE standard benchmark power systems are developed and simulated on the Real-Time Digital Simulator for FSI performance validation. A novel real-time test bed with multi-type generators and utility-scale PV plants are then established for investigation.

Two CCN based frequency prediction methods are applied for multi-timescale and multi-bus type forecasting. These methods have been adopted for system frequency predictions with actual weather information integrated PV plant.

The continuous effects of high penetration PV power are analyzed by online coherency analysis. A generator vulnerability index and power system vulnerability index based visualization has been presented for operation center utilization. Besides, the FSI application for online coherency grouping is presented as well, mitigating the latency and providing an insight of the system dynamic behavior beforehand.

Moreover, the optimal tuning method of the multi-area automatic generation controllers with PV integration are developed and presented as the two-step tuning procedures and the asynchronous tuning method.

9.3 Future Research Suggestions

The following works can be further proceeded based on the aforementioned studies in section 9.2 as a continuation of this dissertation:

- The multi-area interconnected power system AGC scheme can be further analyzed for PV penetration in more areas.
- The CCN structure for power system frequency prediction can be further visualized for understanding and utilization.
- The CCN prediction framework for distributed parallel deployment needs to be considered and analyzed for the large-scale power system utilization.
- The synchronous generator vulnerability indices can be applied to multi-area AGC emergency control scheme, especially with dynamic PV power penetration.
- The optimal tuning method of the multi-area AGCs can be further improved for distributed and asynchronous tuning.

9.4 Summary

In this chapter, the research work in this dissertation has been summarized and presented. The discussion of the future work has been presented and highlighted.

APPENDICES

Appendix A

Parameters of the Real-time Test Bed

Table A-1. Synchronous generator dynamic parameters of the NE-NY system.

Gen	MVA	Rs	Xd	Xd’	Xd’’	Tdo’	Tdo’’	Xls	Xq	Xq’	Xq’’	Tqo’	Tqo’’
1	800	0.002	0.80	0.24	0.20	10.2	0.05	0.10	0.55	0.22	0.20	1.50	0.035
2	850	0.002	2.50	0.59	0.42	6.56	0.05	0.29	2.39	0.51	0.42	1.50	0.035
3	1000	0.002	2.49	0.53	0.45	5.70	0.05	0.30	2.37	0.50	0.45	1.50	0.035
4	800	0.002	2.09	0.34	0.28	5.69	0.05	0.23	2.06	0.32	0.28	1.50	0.035
5	750	0.002	2.47	0.49	0.37	5.40	0.05	0.20	2.32	0.45	0.37	0.44	0.035
6	1000	0.002	2.54	0.50	0.40	7.30	0.05	0.22	2.41	0.45	0.40	0.40	0.035
7	750	0.002	2.21	0.36	0.30	5.66	0.05	0.24	2.19	0.33	0.30	1.50	0.035
8	700	0.002	2.03	0.39	0.31	6.70	0.05	0.19	1.96	0.35	0.31	0.41	0.035
9	1000	0.002	2.10	0.57	0.45	4.79	0.05	0.29	2.05	0.50	0.45	1.96	0.035
10	875	0.002	1.47	0.40	0.35	9.37	0.05	0.17	1.01	0.39	0.35	1.50	0.035
11	1300	0.002	1.66	0.23	0.15	4.10	0.05	0.13	1.59	0.19	0.15	1.50	0.035
12	2000	0.002	2.02	0.62	0.50	7.40	0.05	0.44	1.90	0.56	0.50	1.50	0.035
13	10000	0.002	1.48	0.27	0.20	5.90	0.05	0.15	1.43	0.25	0.20	1.50	0.035
14	10000	0.002	1.80	0.28	0.23	4.10	0.05	0.17	1.73	0.25	0.23	1.50	0.035
15	10000	0.002	1.80	0.28	0.23	4.10	0.05	0.17	1.73	0.25	0.23	1.50	0.035
16	10000	0.002	1.78	0.35	0.27	7.80	0.05	0.20	0.20	0.30	0.27	1.50	0.035

Table A-2. Photovoltaic station parameters for both NE and NY system.

PV Gen	Bus	kV	MW	PV Type	Irradiance Rated (w/m^2)	Array shape (series*parallel)
17	69	345	1148	Polycrystalline	1000	115*285
18	70	345	840	Polycrystalline	1000	115*285

Table A-3. Photovoltaic module parameters for both NE and NY system.

PV Gen-17	Per string per module	36
	Number of parallel string	1
	Module Open Circuit Voltage	21.7 V
	Module Short Circuit Voltage	3.35 A
	Module Voltage at Pmax	17.4 V
	Module Current at Pmax	3.05 A
PV Gen-18	Per string per module	42
	Number of parallel string	1
	Module Open Circuit Voltage	21.7 V
	Module Short Circuit Voltage	3.35 A
	Module Voltage at Pmax	17.4 V
	Module Current at Pmax	3.05

Table A-4. Speed governor and AVR parameters of the NE-NY power system.

Gen	Bus	Tr	Ka	Ta	Kf	Tf	Efm	Efn	1/R	Tm	Tn	Tg	T1	T2	T3
1	53	0.01	50	0.02	0.1	0.5	4	-4	20	1.1	0	0.1	0.1	0	0
2	54	0.01	50	0.02	0.1	0.5	4	-4	20	1.1	0	0.1	0.1	0	0
3	55	0.01	50	0.02	0.15	0.5	4	-4	20	1.1	0	0.2	0.5	0	0
4	56	0.01	50	0.02	0.15	0.5	4	-4	20	1.1	0	0.2	0.1	2.5	8
5	57	0.01	50	0.02	0.15	0.5	4	-4	20	1.1	0	0.1	0.1	0	0
6	58	0.01	50	0.02	0.15	0.5	4	-4	20	1.1	0	0.2	0.1	2.5	8
7	59	0.01	50	0.02	0.15	0.5	4	-4	20	1.1	0	0.1	0.1	0	0
8	60	0.01	50	0.02	0.025	0.5	4	-4	20	1.1	0	0.1	0.1	0	0
9	61	0.01	50	0.02	0.1	0.5	4	-4	20	1.1	0	0.2	0.1	2.5	8
10	62	0.01	50	0.02	0.025	0.5	4	-4	20	1.1	0	0.2	0.1	2.5	8
11	63	0.01	50	0.02	0.025	0.5	4	-4	20	1.1	0	0.2	0.5	0	0
12	64	0.01	50	0.02	0.1	0.5	4	-4	20	1.1	0	0.2	0.1	2.5	8
13	65	0.01	50	0.02	0.1	0.5	4	-4	20	1.1	0	0.1	0.1	0	0
14	66	0.01	50	0.02	0.05	0.5	4	-4	20	1.1	0	0.2	0.1	2.5	8
15	67	0.01	50	0.02	0.05	0.5	4	-4	20	1.1	0	0.2	0.1	2.5	8
16	68	0.01	50	0.02	0.05	0.5	4	-4	20	1.1	0	0.2	0.1	2.5	8

Table A-5. PSS parameters of the NE-NY power system.

Gen	Bus	Gw	Tw	T1	T2	T3	T4	dVmax	dVmin
3	54	40	1.5	0.24	0.08	0.24	0.08	0.2	-0.2
9	61	40	1.5	0.25	0.10	0.25	0.10	0.2	-0.2
10	62	40	1.5	0.21	0.07	0.21	0.07	0.2	-0.2
12	64	40	1.5	0.24	0.08	0.24	0.08	0.2	-0.2
14	66	40	1.5	0.60	0.20	0.60	0.20	0.2	-0.2
15	67	40	1.5	0.36	0.11	0.36	0.11	0.2	-0.2
16	68	40	1.5	0.69	0.23	0.69	0.23	0.2	-0.2

Table A-6 Bus Parameters for IEEE NE-NY system in MVA base.

Bus	Pgen	Pload	Qload			Bus	Pgen	Pload	Qload
1		252.7	118.56			19		0	0
2		0	0			20		680	103
3		322	2			21		274	115
4		200	73.6			22		0	0
5		0	0			23		248	85
6		0	0			24		484	-80
7		234	84			25		224	47
8		208.8	70.8			26		139	17
9		104	125			27		281	76
10		0	0			28		206	28
11		0	0			29		284	27
12		9	88			30		0	0
13		0	0			31		0	0
14		0	0			32		0	0
15		320	153			33		352	24
16		504	44			34		0	0
17		0	0			35		0	0
18		158	30			36		102	-19.5
37		6000	3			54	545		
38		0	0			55	650		
39		267	12.6			56	632		
40		65.63	23.53			57	505.2		
41		5000	400			58	700		
42		6150	400			59	560		
43		0	0			60	540		
44		267.55	4.84			61	800		
45		448	45			62	500		
46		150.7	28.5			63	1000		
47		203.12	32.59			64	1350		
48		241.2	2.2			65	2796		
49		164	29			66	5785		
50		100	-147			67	6000		
51		337	-122			68	5500		
52		3970	223			69	1184		
53	2.5	0	0			70	740		

Appendix B

Control Diagram of the Utility-scale PV Plant

The PEIs are a DC-DC buck converter providing the maximum power and voltage of PV-array at each weather conditions as input to a two-level VSI. The MPPT algorithm implemented in order to harness the maximum amount of power at each solar irradiance and ambient temperature operating point condition is the Perturb and Observe (P&O) method. While P&O is considered as a slow tracking method and might fail under fast variations in irradiance, its implementation is quite simple in comparison to other conventional as well as novel MPPT algorithms. A passive low-pass filter (LPF) is further installed at the output terminals of the inverter in order to eliminate the high frequency switching harmonics in output current waveform.

The switch-model VSI and its associated control structure comprising of PI Controllers have been implemented based on the popular SRF theory in RSCAD; this has been illustrated in both Figure 2.5 and Figure B-1. The goal is to regulate the current output of the inverter to track a specified reference signal.

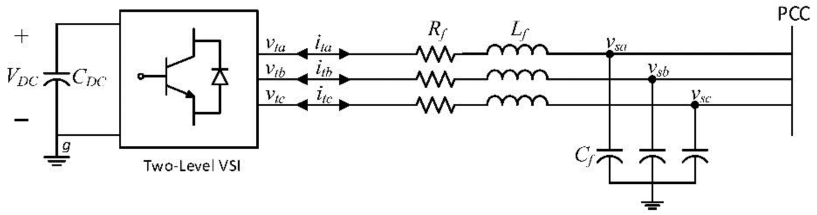

Figure B-1 Circuit diagram for a mathematical description

REFERENCES

[1] R. C. Armstrong, C. Wolfram, K. P. de Jong, R. Gross, N. S. Lewis, B. Boardman, A. J. Ragauskas, K. E. Martinez, G. Carbtree, M. V. Ramana, The Frontiers of energy, *Nat. Energy*, 1 (2016) 1-8.

[2] A. A. Faecett et al., Can Paris pledges avert severe climate change?, *Science*, 350 (2015) 1168-1169.

[3] B. Obama, The irreversible momentum of clean energy, *Science,* 09 (2017). 1-4.

[4] Department of Energy, Revolution…Now: The future Arrives for Five Clean Energy Technologies—2016 Updates, (DOE, Washington, DC, 2016): http://bit.ly/2iQjPbD.

[5] B. V. Mathiesen, H. Lund, and K. Karisson, 100% Renewable energy systems, climate mitigation and economic growth, *Applied Energy,* 88 (2011) 488-501.

[6] S. Eftekharnejad, V. Vittal, G. T. Heydt & J. Loehr, Impact of Increased Penetration of Photovoltaic Generation on Power Systems, *IEEE Trans. on Power Syst.*, 28 (2) 2013.

[7] S. Eftekharnejad, G. T. Heydt, & V. Vittal, Optimal Generation Dispatch With High Penetration of Photovoltaic Generation, *IEEE Trans. on Sustainable Energy*, 6 (3) 2015.

[8] M. Kezunovi, V. Vittal, S. Meliopoulos, & T. Mount, The Big Picture: Smart Research for Large-Scale Integrated Smart Grid Solutions, *IEEE PES Mag.*, 10 (4) (2012) 22-34.

[9] G. K. Venayagamoorthy, K. Rohirg, & I. Erlich, One step ahead: short-term wind power forecasting and intelligent predictive control based on data analytics, *IEEE PES Mag.*, 10 (2012) 70-78.

[10] C. Ji, et al. Large-scale data analysis of power grid resilience across multiple US serivice regions, *Nature Energy*, 1 (16052) (2016) 1-8.

[11] F. Aminifar, M. Fotuhi-Firuzabad, A. Safdarian, A. Davoudi, & M. Shahidehpour, Synchrophasor measurement technology in power systems: panorama and state-of-the-art, *IEEE Access*, 2 (2014) 1607-28.

[12] Y. Haibo, V. Vittal & Y. Zhong, Self-healing in power systems: an approach using islanding and rate of frequency decline-based load shedding, *IEEE Trans. on Power Syst*, 18 (1) (2013) 174-81.

[13] A. G. Phadke & J. S. Thorp, *Synchronized phasor measurements and their applications*, New York: Springer, 2008.

[14] G. K. Venayagamoorthy, Synchrophasor Data Driven Situational Intelligence for Power System Operation, *in CIGRE Grid of the Future Symposium*, Houston, TX, USA, 2014.

[15] IEEE Standard for Synchrophasor Measurements for Power Systems, IEEE Std C37.118.1-2011 (Revision of IEEE Std C37.118.1-2005).

[16] U.S. Energy Information Administration, New technology can improve electric power system efficiency and reliability, 2012. http://www.eia.gov/todayinenergy/detail.php?id=5630.

[17] North American Synchrophasor Initiative. Phasor Measurement Units in North American Power Grid, 2015.

[18] P. Pinceti, M. Vanti, C. Brocca, M. Carnesecchi, & G. P. Macrea, Design crietia for a power management system for microgrids with renewable sources, *Electr. Power Syst. Res.*, 122 (2015) 168-179.

[19] C. Ventura & G. M. Tina, Utility scale photovoltaic plant indices and models for on-line monitoring and fault detection purposes, *Electr. Power Syst. Res.*, 136 (2016) 43-56.

[20] V. Salehi, A. Mohamed, A. Mazloomzadeh, & O. A. Mohammed, Laoratory-Based Smart Power System, Part I: Design and System Development, *IEEE Trans. on Smart Grid*, 3 (3) 2012.

[21] V. Salehi, A. Mohamed, A. Mazloomzadeh, & O. A. Mohammed, Laoratory-Based Smart Power System, Part II: Control, Monitoring, and Protection, *IEEE Trans. on Smart Grid*, 3 (3) 2012.

[22] Q. Hu, F. Li, & C. F. Chen, A Smart Home Test Bed for Undergraduate Education to Bridge the Curriculum Gap From Traditional Power Systems to Modernized Smart Grids, *IEEE Trans. on Edu.*, 58 (1) (2015) 32-38.

[23] J. H. Chow, Power System Coherency and Model Reduction, New York, NY, *USA: Springer*, 2013.

[24] R. A. Schlueter , G. L. Park, & E. Retford. (1978). A study of frequency prediction for power systems, *IEEE Trans. on Automatica Control*, 23 (6) 996-1000.

[25] B. Pal & B. Chaudhuri, Robust Control in Power Systems, Berlin, *Germany: Springer*, Jun. 2005.

[26] P. Kundur, Power System Stability and Control, *New York: McGraw-Hill*, 1994.

[27] Y. Wei, & G. K. Venayagamoorthy. Frequency prediction of synchronous generators in a multi-machine power system with a photovoltaic plant using a cellular computational network, *In IEEE Symposium Series on Computational Intelligence in Smart Grid (CIASG)*, Cape Town, South Africa, 2015.

[28] Y. Wei & G. K. Venayagamoorthy. Frequency situational intelligence in a Multi-machine power system, *Neural Network,* 93 (2017) 21-35.

[29] Y. Wei & G. K. Venayagamoorthy. A lite cellular generalized neuron network for frequency prediction of synchrnous generators in a multimachine power system, *in IEEE World Congress on Computational Intelligence (WCCI)*, Vancouver, Canada, 2016.

[30] M. A. Rahman, Y. Wei & G. K.. Venayagamoorthy, Cellular computational generalized neuron network with cooperative PSO for power systems, *in Proc. 2017 International Joint Conference on Neural Networks (IJCNN)*, anchorage, AK, USA, 2017.

[31] Y. Wei, K. Tang & G. K. Venayagamoorthy, Situational intelligence for online coherency analysis of synchronous generators in power system, *North American Symposium Coference* (*NAPS*), Denvor, Co, USA, 2016.

[32] Y. Wei & G. K. Venayagamoorthy, Situational Awareness of Coherency Behavior of Synchronous Generators in a Power System with Utility-Scale Photovoltaics, *Electric Power System Research,* under second review.

[33] Y. Wei, I. Jayawardene & G. K. Venayagamoorthy, Optimal Automatic Generation Controllers in A Multi-Area Interconnected Power System with Utility-Scale PV Plants, *IET Smart Grid.,* under review.

[34] Y. Wei & G. K. Venayagamoorthy, PMU Based Asynchronous Tuning of Automatic Generation Control in A Multi-Area Power System, *2019 IEEE Power & Energy Society General Meeting (PES GM)*, under review.

[35] I. Jayawardene, Y. Wei & G. K, Venayagamoorthy. Optimized automatic generation control in a multi-area power system with particle swarm optimization, *in 2017 IEEE Symposium series on Computational Intelligence (SSCI)*, Honolulu, HI, USA, 2017.

[36] A. Arzani, P. Arunagirinathan, & G. K. Venayagamoorthy, Development of Optimal PI Controllers for a Grid-Tied Photovoltaic Inverter, *in IEEE Symposium on Computational Intelligence Applications in Smart Grid (CIASG)*, Cape Town, South Africa, December 2015.

[37] A. Yazdani and P. Dash, A Control Methodology and Characterization of Dynamics for a Photovoltaic (PV) System Interfaced With a Distribution Network, *IEEE Trans. on Power Deli.*, 24 (3) (2009) 1538-1555.

[38] J. Liang, D. D. Molina, G. K. Venayagamoorthy, & R. Harley, Two-level dynamic stochastic optimal power flow control for power systems with intermittent renewable generation, *IEEE Trans. on Power Syst.*, 28 (3) (2013) 2670-2678.

[39] P. Arunagirinathan, H. Abdelsalam, & G. K, Venayagamoorthy, Remote Power System Stabilizer Tuning Using Synchrophasor Data, *in IEEE Symposium on Computational Intelligence Applications in Smart Grid (CIASG)*, Orlando, FL, USA, 2014.

[40] A. Pappachen, A. P. Fathima, Critical research areas on load frequency control issues in a deregulated power system: a state, *Renew. Sustainable Energy Rev.*, 72 (2017) 163-177.

[41] Ibraheem, P. Kumar, and D. P. Kothari, Recent philosophies of automatic generation control strategies in power systems, *IEEE Trans.Power Syst.*, 20 (1) (2009) 346-357.

[42] N. Jaleeli, L. S. VanSlyck, D. N. Ewart, L. H. Fink, and A. G. Holfmann, Understanding automatic generation control, *IEEE Trans. Power Syst.*, 7 (3) (1997) 1106-1122.

[43] NERC Subcommittee, Balancing and frequency control, NERC, Princeton, NJ, USA, 2011.

[44] NERC, Glossary of terms used in NERC reliability standards, Atlanta, GA, Junuary, 2014.

[45] H. Bevrani, Robust power system frequency control, 2nd ed, Springer, 2014.

[46] H. Bevrani & T. Hiyama, Intelligent Automatic Genration Control, 1st ed, CRC Press, 2011.

[47] I. Jayawardene & G. K. Venayagamoorthy, Reservoir Based Learning Network for Control of Multi-Area Power System with Variable Renewable Generation, *Neurocomputing*, 170 (2015) 428-438.

[48] A. Routray & A. K. Pradhan, A novel kalman filter for frequency estimation of distorted signals in power systems, *IEEE Trans. Instrum. Meas.*, 51(3) (2002), 469-79.

[49] M. S. Sachdev & M. M. Giray, A least square technique for determining power system frequency, *IEEE Trans. Power App. Syst*, PAS-104 (2) (1985), 437-44.

[50] M. S. Reza, M. Ciobotaru, & V. G. Agelidis, Power system frequency estimation by using a Newton-type technique for smart meters, *IEEE Trans. Instrum. Meas*, 64 (3) (2015) 615-24.

[51] Y. Xia, Y. He, K. Wang, W. Pei, Z. Blazic, & D. Mandic, A complex least squares enhanced smart DFT technique for power system frequency estimation, *IEEE Trans. Power Del.* 32 (3) (2017) 1270-1278.

[52] R. Jinfeng, & M. Kezunovic, A hybrid method for power system frequency estimation, *IEEE Trans. Power Del*, 27 (3) (2012) 1252-59.

[53] L. L. Lai , C. T. Tse , W. L. Chan, & A. T. P. So, Real-time frequency and harmonic evaluation using artificial neural networks, *IEEE Trans. Power Del*, 14 (1) (1999) 52-9.

[54] E. S. Karapidakis, Machine learning for frequency estimation of power systems, *Applied Soft Computing*, 7 (1) (2007), 105-14.

[55] R. F. Chang, C. N. Lu, & T. Y. Hsiao, Prediction of frequency response after generator outage using regression tree, *IEEE Trans. on Power Syst*, 20 (4) (2005), 2146-57.

[56] Md. Alizadeh, & Tj. Amraee, Adaptive scheme for local prediction of post-contingency power system frequency, *Electric Power Systems Research*, 107 (2014), 240-49.

[57] D. Jin, & M. Xiao, Frequency prediction of power systems in FNET based on state-space approach and uncertain basis functions, *IEEE Trans. Power Syst*, 29 (6) (2014) 2602-12.

[58] H. Ma, & H. Li, Analysis of frequency dynamics in power grid: a bayesian structure learning approach, *IEEE Trans. Smart Grid*, 4 (1) (2013) 457-66.

[59] C. Meng, S. S. Saif, & W. Jianzhong, Benefits of using virtual energy storage system for power system frequency response, *Applied Energy*, 194 (2016) 376-385.

[60] F. Saber, T. A. Seyed, & S. Mohammad, Grid frequency control with electric vehicles by using of an optimal fuzzy controller, *Applied Energy*, 178 (2016) 918-928.

[61] J. Zhong, L. He, C. Li, Y. Cao, J. Wang, B. Fang, L. Zeng, & G. Xiao, Coordinated control for large-scale EV charging facilities and energy storage devices participating in frequency regulation, *Applied Energy*, 123 (2014) 253-62.

[62] F. Beaufays, Y. Abdel-Magid, & B. Widow, Application of neural networks to load-frequency control in power systems, *Neural Networks*, 7 (1994) 183-194.

[63] L. R. Chang-Chien, Y. S. Wu & J. S. Cheng, Online estimation of system parameters for artificial intelligence applications to load frequency control, *IET Gen., Trans. and Dist.*, 5 (2011) 895-902.

[64] Yufei T., Jun Y., Jun Y., & Haibo H, Intelligent load frequency controller using GrADP for island smart grid with electric vehicles and renewable resources, *Neurocomputing*, 170 (2015) 406-416.

[65] Y. Engin, Interval type-2 fuzzy PID load frequency controller using Big Bang-Big Crunch optimiztion, *Applied Soft Computing,* 15 (2014) 100-112.

[66] K. Sabahi, S. Ghaemi, & S. Pezeshki, Application of type-2 fuzzy logic system for load frequency control using feedback error learning approaches, *Applied Soft Computing*, 21 (2014) 1-11.

[67] K. Sabahi, S. Ghaemi, & M. Badamchizadeh, Designing an adapative type-2 fuzzy logic system load frequency control for a nonlinear time-delay power system, *Applied Soft Computing*, 43 (2016) 97-106.

[68] S. Prakash, & S. K. Sinha. Simulation based neuro-fuzzy hybrid intelligent PI control approach in four-area load frequency control of interconnected power system, *Applied Soft Computing*, 23 (2014) 152-164.

[69] B. Luitel, & G. K. Venayagamoorthy, Cellular computational networks – a scalable architecture for learning the dynamics of large networked systems, *Neural Networks,* 50 (2014) 120-3.

[70] V. K. Raghavendra, & G. K. Venayagamoorthy, Generalized neural: Feedforward and recurrent architectures, *Neural Networks*, 22 (7) (2009) 1011-17.

[71] K. Cihan, K. Fuat, & C. A. Mehmet, FPGA implementation of neuro-fuzzy system with improved PSO learning, *Neural Networks*, 79 (2016) 128-40.

[72] J. H. Chow, *Power system coherency and model reduction*, New York, NY, USA: Springer, 2013.

[73] G. Xu & V. Vittal, Slow coherency based cutset determination algorithm for large power systems, *IEEE Trans. Power Syst.*, 25 (2010) 877-884.

[74] M. Jonsson, M. Begovic and J. Daalder, A new method suitable for real-time generator coherency determination, *IEEE Trans. Power Syst.*, 19 (3) (2004) 1473-1482.

[75] N. Senroy, Generator coherency using the Hilbert-Huang transform, *IEEE Trans. Power Syst.*, 23 (4) (2008) 1701-1708.

[76] Y. Susuki and I. Mezic, Nonlinear koopman modes and coherency identification of coupled swing dynamics, *IEEE Trans. Power Syst.*, 26 (2011) 1894-1904.

[77] Z. Lin, F. Wen, Y. Ding and Y. Xue, Data-driven Coherency Identification for Generators Based on Spectral Clustering, *IEEE Trans. Ind. Informat.*, 99 (2017) 1-12.

[78] K. K. Anaparthi, B. Chaudhuri, N. F. Thornhill, B. C. Pal, Coherency identification in power systems through principal component analysis, *IEEE Trans. Power Syst.*, 20 (3) (2005) 1658-1660.

[79] M. R. Aghamohammadi, S. M. Tabandeh, A new approach for online coherency identification in power systems based on correlation characteristics of generators rotor oscillations, *Int. J. Elect. Power Energy Syst*., 83 (2016) 470-484.

[80] T. Jiang, H. Jia, H. Yuan, N. Zhou, and F. Li, Projection Pursuit: a general methodology of wide-area coherency detection in bulk power grid, *IEEE Trans. Power Syst.*, 31 (2016) 2776-2786.

[81] M . A. M. Ariff and B. C. Pal, Coherency identification in interconnected power system—an independent component analysis approach, *IEEE Trans. Power Syst.*, 28 (2013) 1747-1755.

[82] O. Gomez, and M. A. Rios, Real time identification of coherent groups for controlled islanding based on graph theory, *IET Gen. Trans. & Dist.*, 9 (2015) 748-758.

[83] J. Wei, D. Kundur and K. L., Butler-Purry, A novel bio-inspired technique for rapid real-time generator coherency identification, *IEEE Trans. Smart Grid*, 6 (2015) 178-188.

[84] A. M. Khalil, R. Iravani, A dynamic coherency identification method based on frequency deviation signals, *IEEE Trans. Power Syst*., 31 (2016) 1779-1787.

[85] R. R. Yager and F. E. Petry, Hypermatching: Similarity Matching with Extreme Values, *IEEE Trans. Fuzzy Syst.*, 22 (2014) 949-957.

[86] Y. M. Park, and K. Y. Lee, Optimal decentralized load frequency control, *Electr. Pow. Syst. Res*. 7 (1984) 279-288.

[87] Y. Arya, AGC performance enrichment of multi-source hydrothermal gas power systems using new optimized FOFPID controller and redox flow batteries, *Energy*, 127 (127) 704-715.

[88] Y. Arya and N. Kumar, Optimal AGC with redox flow batteries in multi-area restructured power systems, *Eng. Sc. Tech., an Int. J.*, 19 (3) (2016) 1145-1159.

[89] H. Shayeghi, and H. A. Shayanfa, Design of decentralized robust LFC in a competitive electricity environment. *J. Electr. Eng.* 56 (2005) 225-236.

[90] B. Chaudhuri, B. C. Pal, and A. C. Zolotas, Mixed-sensitivity approach to H∞ control of power system oscillations employing multiple FACTS devices. *IEEE Trans Power Syst.* 18 (3) (2003) 1149-1156.

[91] C. Chen, K. Zhan, K. Yuan, and X. Teng, Tie-line bias control applicability to load frequency control for multi-area interconnected power systems of complex topology, *Energies,* 10 (78) (2017) 1-15.

[92] K. P. S. Parmar, S. Majhi, and D. P. Kothari, LFC of an interconnected power system with multi-source power generation in deregulated power environment, *Int. J. Electr. Power Energy Syst*. 57 (2014) 277-286.

[93] H. Shayeghi, H. A. Shayanfar, and O. P. Malik, Robust decentralized neural networks based LFC in a deregulated power system, *Electr. Power Syst. Res*. 77 (3-4) (2007) 241-251.

[94] Y. Arya, and N. Kumar, Fuzzy gain scheduling controllers for automatic generation control of two-area interconnected electrical power systems, *Electr. Power Compon. Syst.*, 44 (2016) 737-751.

[95] F. Saber, A. T. Seyed, and S. Mohammad, Grid frequency control with electric vehicles by using of an optimized fuzzy controller, *Appl. Energy*. 178 (1) (2016) 918-928.

[96] R. Khezri, S. Golshannavaz, S. Shokoohi, and H. Bevrani, Fuzzy logic based fine-tuning approach for robust load frequency control in a multi-area power system, *Electr. Pow. Compo. Sys.* 44 (18) (2016) 2073-2083.

[97] S. H. Hosseini, and A. H. Etemadi, Adaptive neuro-fuzzy inference system based automatic generation control, *Electr. Power Syst. Res*. 78 (7) (2008) 1230-1239.

[98] P. K. Hota, and B. Mohanty, Aotumatic generation control of multi-source power generation under deregulated environment, *Int. J. Electr. Power Energy Syst*. 75 (2016) 205-214.

[99] F. Daneshfar, and H. Bevrani, Load-frequency control: a GA-based multi-agent reinforcement learning, *IET Gener. Transm. & Distrib*. 4 (1) (2010) 13-26.

[100] Y. Bao, Y. Li, B. Wang, M. Hu, and P. Chen, Demand response for frequency control of multi-area power system, *J. Mod. Power Sys. Clean Energy*. 5 (1) (2017) 20-29.

[101] S. S. Dhillon, J. S. Lather, and S. Marwaha, Multi objective load frequency control using hybrid bacterial foraging and particle swarm optimized PI controller, *Int. J. Electr. Power Energy Syst*. 79 (2016) 196-209.

[102] N. E. Y. Kouba, M. Menaa, M. Hasni, and M. Boudour, LFC enhancement concerning large wind power integration using new optimized PID controller and RFBs, *IET Gener. Transm. & Distrib.* 10 (16) 4065-4077.

[103] K. Naidu, H. Mokhlis, A. H. Bakar, and V. Terzija, Performance investigation of ABC algorithm in multi-area power system with multiple interconnected generators, *Appl. Soft Comput.* 57 (2017) 436-451.

[104] Y. D. Valle, G. K. Venayagamoorthy, S. Mohagheghi, and R. G. Harley, Particle swarm optimization: basic concepts, variants and applications in power systems. *IEEE Trans. Evolut. Comput*. 12 (2) (2008) 171-195.

[105] J. Chuanwen, and E. A. Bompard, A self-adaptive chaotic particle swarm algorithm for short term hydroelectric system scheduling in deregulated environment. *Energy Convers. Manag*. 46 (17) (2003) 2689-2696.

[106] S. P. Bhatt, S. P. Ghoshal, and R. Roy, Coordinated control of TCPS and SMES for frequency regulation of interconnected restructured power systems with dynamic participation from DFIG based wind farm, *Renew. Energy*. 40 (2012) 40-50.

[107] Y. Arya, and N. Kumar, AGC of a multi-area multi-source hydrothermal power system interconnected via AC/DC parallel links under deregulated environment, *Int. J. Electr. Power Energy Syst.* 75 (2016) 127-138.

[108] H. Shayeghi, H. A. Shayanfar, and A. Jalili, LFC Design of a deregulated power system with TCPS using PSO, *Int. J. Electr. Comput. Energ. Electron Commun Eng.*, 3 (4) (2012) 691-699.

[109] G. Hou, L. Qin, X. Zheng, and J. Zhang, Application of PSO-based fuzzy PI controller in multi-area AGC system after deregulation. *Proc. IEEE*, 1 (2012) 1417-1422.

[110] M. T. Muhssin, et al., A novel adaptive deadbeat-based control for load frequency control of low inertia system in interconnected zones north and south of Scotland, *Int. J. Electr. Power Energy Syst.*, 89 (2017) 52-61.

[111] E. Hildebrandt, et al., California ISO 2017 Annual Report on Market Issues & Performance, Folsom, CA, Jun. 2018.

[112] C. Pilong, PJM Manual 12: Balancing Operations, Norristown, PA. 2018, [Online] Available: https://www.pjm.com /media/ documents/ manuals/ m12.ashx.

[113] A. M. Prostejovsky, M. Marinelli, M. Rezkalla, M. H. Syed, and E. G. Sansano, Tuningless Load Frequency Control Through Active Engagement of Distributed Resources, *IEEE Trans. Power Syst.*, 33 (2018) 2929-2939.

[114] M. Ma, C. Zhang, X. Liu, and H. Chen, Distributed Model Predictvie Load Frequency Control of the Multi-Area Power System After Deregulation, *IEEE Trans. Ind. Electron.*, 64 (2017) 5129-5139.

[115] V. Donde, M. A. Pai, and I. A. Hiskens, Simulation and optimization in an AGC system after deregulation, *IEEE Trans. Power Syst.*, 16 (2001) 481-489.

[116] L. Zhang, Y. Luo, Z. Shao, Y. Zheng, and Y. Cai, The Study of Optimal Cooperation of AGC in Different Areas Based on Regulation Marginal Cost, *in Proc. 2016 IEEE Power and Energy Society General Meeting (PESGM) Conf.*, (2016) 1-5.

[117] S. Dhundhara, and Y. P. Verma, Capacitive energy storage with optimized controller for frequency regulation in realistic multisource deregulation power system, *Energy*, 147 (2018) 1108-1128.

[118] T. Avila, and H. Chavez, Secondary reserves determination based on CPS1 and CPS2 compliant AGC operation, *in Proc. 2016 IEEE International on Automatica (ICA-ACCA) Conf.,* (2016) 1-5.

BIOGRAPHY

Yawei Wei, Clemson University

He received his MS degree from Michigan Technological University, Houghton, MI, at 2014. He received his BS degree from Shanghai University of Electric Power, Shanghai, China, at 2010. He is currently a PhD candidate at Clemson University. His research topic is power system frequency situational intelligence improvement for smart grid operation centers with high level of PV power integration. He is currently a research assistant with the Real-Time Power and Intelligent Systems Laboratory.